

COSMOGLOBE I. Improved Wilkinson Microwave Anisotropy Probe frequency maps through Bayesian end-to-end analysis

D. J. Watts^{1*}, A. Basyyrov¹, M. Galloway¹, H. T. Ihle¹, S. Paradiso², F. Rahman³, H. Thommesen¹, M. Bersanelli⁴, L. A. Bianchi⁴, M. Brilenkov¹, L. P. L. Colombo⁴, H. K. Eriksen¹, J. R. Eskilt^{1,5}, K. S. F. Fornazier⁶, C. Franceschet⁴, U. Fuskeland¹, E. Gjerløw¹, B. Hensley⁷, L. T. Hergt⁸, D. Herman¹, G. A. Hoerning⁶, K. Lee¹, J. G. S. Lunde¹, A. Marins^{6,9}, S. K. Nerval^{10,11}, S. K. Patel¹², M. Regnier¹³, M. San¹, S. Sanyal¹², N.-O. Stutzler¹, A. Verma¹², I. K. Wehus¹, and Y. Zhou¹⁴

¹ Institute of Theoretical Astrophysics, University of Oslo, Blindern, Oslo, Norway

² Waterloo Centre for Astrophysics, University of Waterloo, Waterloo, ON N2L 3G1, Canada

³ Indian Institute of Astrophysics, Koramangala II Block, Bangalore, 560034, India

⁴ Dipartimento di Fisica, Università degli Studi di Milano, Via Celoria, 16, Milano, Italy

⁵ Imperial Centre for Inference and Cosmology, Department of Physics, Imperial College London, Blackett Laboratory, Prince Consort Road, London SW7 2AZ, United Kingdom

⁶ Instituto de Física, Universidade de São Paulo - C.P. 66318, CEP: 05315-970, São Paulo, Brazil

⁷ Department of Astrophysical Sciences, Princeton University, 4 Ivy Lane, Princeton, NJ 08540

⁸ Department of Physics and Astronomy, University of British Columbia, 6224 Agricultural Road, Vancouver BC, V6T1Z1, Canada

⁹ Department of Astronomy, University of Science and Technology of China, Hefei, China

¹⁰ David A. Dunlap Department of Astronomy & Astrophysics, University of Toronto, 50 St. George Street, Toronto, ON M5S 3H4, Canada

¹¹ Dunlap Institute for Astronomy & Astrophysics, University of Toronto, 50 St. George Street, Toronto, ON M5S 3H4, Canada

¹² Department of Physics, Indian Institute of Technology (BHU), Varanasi - 221005, India

¹³ Laboratoire Astroparticule et Cosmologie (APC), Université Paris-Cité, Paris, France

¹⁴ Department of Physics, UC Berkeley

March 3, 2023

ABSTRACT

We present the first joint analysis of *WMAP* and *Planck* LFI time-ordered data, processed within the Bayesian end-to-end COSMOGLOBE framework. This framework builds directly on a similar analysis of the LFI measurements by the BEYONDPLANCK collaboration, and approaches the CMB analysis challenge through Gibbs sampling of a global posterior distribution. The computational cost of producing one complete *WMAP*+LFI Gibbs sample is 581 CPU-hr, including calibration, mapmaking, and component separation, of which 389 CPU-hr is spent on *WMAP* low-level processing; this demonstrates that end-to-end Bayesian analysis of the *WMAP* data is computationally feasible. We find that our *WMAP* posterior mean temperature sky maps are largely consistent with the official maps, and the resulting CMB power spectrum is in excellent agreement with previous results. The most notable difference is a slightly lower CMB quadrupole amplitude of $\sigma_2 = 120 \pm 65 \mu\text{K}^2$, as compared to $\sigma_2 = 229 \pm 97 \mu\text{K}^2$ in the BEYONDPLANCK analysis. In contrast, our *WMAP* polarization maps differ more notably from the official results, and in general they exhibit weaker transmission imbalance residuals; it is particularly noteworthy that our *W*-band sky maps appear statistically consistent with the *V*-band maps. At a higher level, *WMAP*-minus-LFI frequency map differences appear for the first time visually consistent with instrumental noise over most of the sky. Still, we identify three specific issues that require additional work, namely 1) noise mismodeling at high temporal frequencies, 2) a quadrupolar *V*-band temperature residual at the $2 \mu\text{K}$ level; and 3) a strong degeneracy between the absolute *K*-band calibration and the dipole of the anomalous microwave emission component. Nevertheless, we believe that the reprocessed *WMAP* maps presented here are significantly cleaner in terms of systematic uncertainties than the official *WMAP* maps, and they should be preferable for most scientific analyses that rely on *WMAP* measurements. Both sky maps and the associated code are made publicly available through the COSMOGLOBE web page.

Something to emphasize – we have good W4 maps

Key words. ISM: general – Cosmology: observations, polarization, cosmic microwave background, diffuse radiation – Galaxy: general

Contents

1	Introduction	2	2.4	Sky model	5
2	End-to-end Bayesian CMB analysis	3	2.5	Priors	5
2.1	LFI and BEYONDPLANCK	3	2.6	Posterior distribution and Gibbs sampling	5
2.2	Official <i>WMAP</i> pipeline	3	2.7	Sampling algorithms	5
2.3	Instrument model	4	2.7.1	Review of sampling algorithms	5
			2.7.2	Differential mapmaking	7
			2.7.3	Transmission imbalance estimation	7
			2.7.4	Baseline sampling	7

* Corresponding author: D. J. Watts; duncanwa@astro.uio.no

3 Data and data processing	7
3.1 Publicly available <i>WMAP</i> products	8
3.2 TOD pre-processing and data selection	8
3.3 Computational resources	8
4 Instrumental parameters	9
4.1 Trace plots and correlations	9
4.2 Gain and baselines	9
4.3 Transmission imbalance	10
4.4 Instrumental noise and goodness-of-fit	11
5 Frequency maps	13
5.1 Map summary statistics	14
5.2 Comparison with 9-year <i>WMAP</i> maps	15
5.3 Consistency within <i>WMAP</i> channels	21
5.4 Consistency between <i>WMAP</i> and LFI	21
6 Preliminary astrophysical results	26
6.1 CMB results	26
6.1.1 Solar dipole	26
6.1.2 Low- ℓ anomalies	26
6.1.3 Angular temperature power spectrum	27
6.1.4 Large-scale polarization	27
6.2 Galactic foregrounds	27
6.3 <i>WMAP</i> -versus-LFI signal-to-noise ratio comparison	27
7 Systematic error corrections and uncertainties	27
7.1 Sky map corrections	27
7.2 Power spectrum residuals	27
8 Outstanding issues	27
8.1 Noise modeling	27
8.2 <i>V</i> -band quadrupole residual	27
8.3 Degeneracy between <i>K</i> -band calibration and AME dipole	27
8.4 Other minor effects	27
8.4.1 Time-variable bandpass modeling	27
8.4.2 Polarized sidelobe modeling	27
9 Conclusions	27
A Survey of instrumental parameters	40
A.1 Gain, baselines, noise and χ^2	40
A.2 Transmission imbalance	40
B WMAP frequency map survey	40
C Comparison with BEYONDPLANCK LFI results	40

1. Introduction

The discovery of the cosmic microwave background (CMB) by Penzias & Wilson (1965) marked a paradigm shift in the field of cosmology, providing direct evidence that the Universe was once much hotter than it is today, effectively ruling out the steady-state theory of the universe (Dicke et al. 1965). This discovery spurred a series of ground-breaking cosmological experiments, including the Nobel Prize-winning measurements by *COBE*-FIRAS and *COBE*-DMR that confirmed the blackbody nature of the CMB Mather et al. (1994) and measured temperature variations from the primordial gravitational field (Smoot et al. 1992).

The NASA-funded *Wilkinson Microwave Anisotropy Probe* (*WMAP*; Bennett et al. 2003a) mission directly superseded

COBE-DMR, aiming to map the microwave sky with 45 times higher sensitivity and 33 times higher angular resolution, and thereby revolutionizing our understanding of early universe physics (Bennett et al. 2003a). As quantified by Bennett et al. (2013), the permissible parameter space volume for a standard Λ CDM model was decreased by a factor of 68,000 by *WMAP*, and the best pre-*WMAP* determination of the age of the universe was $t_0 < 14$ Gyr from Boomerang (Lange et al. 2001), with best-fit values of 9–11 Gyr; the latter values in apparent contradiction with direct measurements of the oldest globular clusters (Hu et al. 2001).

The ESA-led *Planck* satellite (Planck Collaboration I 2020) was developed concurrently with *WMAP*, and their operation lifetimes briefly overlapped, with *Planck* observing from 2009–2013 and *WMAP* from 2001–2011. *Planck*'s stated goal was to fully characterize the primary CMB temperature fluctuations from recombination, as well as to characterize the polarized microwave sky on large angular scales. Overall, *Planck*'s raw CMB sensitivity was an order of magnitude higher than *WMAP*'s, and its angular resolution three times higher. Today, *Planck* represents the state-of-the-art in terms of full-sky microwave sky measurements.

Planck comprised two independent experiments, namely the Low Frequency Instrument (LFI; Planck Collaboration II 2020) and High Frequency Instrument (HFI; Planck Collaboration III 2020), respectively. The LFI detectors were based on HEMT (high electron mobility transistor) amplifiers, spanning three frequency channels between 30 and 70 GHz, while the HFI detectors were based on TES (transition edge sensitive) bolometers, and spanned six frequency channels between 100 and 857 GHz. For comparison, *WMAP* was also HEMT-based, with comparable sensitivity to LFI alone, and spanned five frequencies between 23 and 94 GHz. At the same time, the two experiments implemented very different scanning strategies, and as a result they are highly complementary and synergistic; together they provide a clearer view of the low-frequency microwave sky than either can alone.

Towards the end of the *Planck* analysis phase it became clear that the interplay between instrument calibration and astrophysical component separation represents a main limiting factor in terms of systematic effects for high signal-to-noise measurements (Planck Collaboration II 2020). Specifically, in order to calibrate the instrument to sufficient precision, it is necessary to know the true sky to a comparably high precision – but to know the sky, it is also necessary to know the instrumental calibration. The data analysis is thus fundamentally circular and global in nature. The final official *Planck* LFI analysis performed four complete iterations between calibration and component separation (Planck Collaboration II 2020), aiming to probe this degeneracy. However, it was clearly recognized that this was not sufficient to reach full convergence, and this sub-optimality led to the BEYONDPLANCK project (BeyondPlanck 2022), which aimed to perform thousands of complete analysis cycles, as opposed to just a handful. This framework was implemented using the Commander3 (Galloway et al. 2022) code, a CMB Gibbs sampler that performs integrated high-level and low-level parameter estimation in a single integrated framework. This analysis demonstrated the feasibility of a full end-to-end Gibbs sampling analysis in the CMB framework, while providing the highest-quality LFI maps to date.

Rather than simply probing the degeneracy between instrument calibration and component separation, a better solution is to actually break it. And the optimal approach to do so is by jointly analyzing complementary datasets, each of which pro-

vide key information regarding the full system. This insight led to the COSMOGLOBE¹ initiative, which is an Open Source and community-wide effort that aims to derive a single joint model of the radio, microwave, and sub-millimeter sky by combining all state-of-the-art experiments. An obvious first extension of the LFI-oriented BEYONDPLANCK project is to analyze the *WMAP* measurements in the same framework. Indeed, already as part of the BEYONDPLANCK suite of papers, Watts et al. (2022) integrated *WMAP* *Q*-band time-ordered data (TOD) into the Commander3 framework, calibrated off of the BEYONDPLANCK sky model.

In this paper, we present the first end-to-end Bayesian analysis of the full *WMAP* TOD, processed within the COSMOGLOBE framework. As such, this paper also presents the first ever joint analysis of two major CMB experiments (LFI and *WMAP*) at the lowest possible level, and as such it constitutes a major milestone of the COSMOGLOBE project. In the future, many more datasets will be added, gradually providing stronger and stronger constraints on the true astrophysical sky. As such, each new experiment will then also in turn improve the instrumental calibration of all previous experiments.

The rest of this paper is organized as follows. In Sect. 2, we provide an brief review of the Bayesian end-to-end statistical framework used in this work, before describing the underlying data and computational expenses in Sect. 3. The main results, as defined by the global posterior distribution, are described in Sects. 4–6, summarizing instrumental parameters, frequency sky maps, and astrophysical results, respectively. In Sect. 7 we provide a discussion of systematic errors, while Sect. 8 discusses a few minor unresolved issues that should be addressed in future work. We conclude in Sect. 9, and lay a path forward for the COSMOGLOBE project.

2. End-to-end Bayesian CMB analysis

We begin by discussing the *WMAP* analysis from uncalibrated TOD to maps. Section 2.1 gives an overview of the BEYONDPLANCK project’s reanalysis of *Planck* LFI data, Sect. 2.2 provides a brief overview of the official *WMAP* pipeline, and Sect. 2.3 constructs the data model that is used in the end-to-end Gibbs sampling analysis.

2.1. LFI and BEYONDPLANCK

The BEYONDPLANCK project (BeyondPlanck 2022) was the first true application of end-to-end Gibbs sampling in the framework of CMB data analysis. The *Planck* Low Frequency Instrument data had been gradually improved through each *Planck* data release, specifically PR1 (Planck Collaboration II 2016), PR2 (Planck Collaboration II 2016), PR3 (Planck Collaboration II 2020), and PR4 (Planck Collaboration II 2016). Even after PR4, the LFI data still failed polarization null tests and contained visually striking poorly measured modes corresponding to relative gain uncertainties between different detectors. It was during the PR3 analysis when it became clear that there was a degeneracy between the assumption of the sky’s polarization and the gain differences, a problem that affected the final PR4 maps.

The BEYONDPLANCK analysis generated the first clean LFI maps by Gibbs sampling the sky components and underlying instrumental parameters jointly (BeyondPlanck 2022; Galloway et al. 2022; Basyrov et al. 2022). The Commander3 pipeline was used to perform the low-level data analysis conditioned on a sky model that was created through component separation, and the

reprocessed maps were used to perform component separation once again. This Gibbs chain allowed for data-driven estimates of the instrumental properties to be determined, created the best LFI maps to date, and in doing so fully explored the degeneracies between the low-level instrumental parameters themselves and our knowledge of the sky (Andersen et al. 2022; Svalheim et al. 2022).

2.2. Official WMAP pipeline

The *WMAP* satellite carried forty differential polarization-sensitive radiometers grouped as differencing assemblies (DAs), where one pair was sensitive to the difference in signal at one polarization orientation and the other pair sensitive to the orthogonal polarization. In total, the DAs were allocated as: 1 *K* (23 GHz), 1 *Ka* (30 GHz), 2 *Q* (40 GHz), 2 *V* (60 GHz), and 4 *W* (90 GHz).

The *WMAP* pointing solution was determined using the boresight vectors of individual feedhorns in spacecraft coordinates, in combination with on-board star trackers. Thermal flexure of the tracking structure introduced small pointing errors, as discussed by Jarosik et al. (2007). Using the temperature variation measured by housekeeping data, the quaternion pointing solution was corrected using a linear model that depends on arcsecond per kelvin. The residual pointing errors were computed using observations of Jupiter and Saturn, and the reported upper limit was given by 10'' (Bennett et al. 2013; Greason et al. 2012).

The *WMAP* bandpasses were measured directly pre-launch, sweeping a signal source through 201 frequencies and recording the output (Jarosik et al. 2003b). The bandpass responses have not been updated since the initial data release. However, as noted in Bennett et al. (2013), there has been an observed drift in the center frequency of *K*, *Ka*, *Q*, and *V*-band corresponding to a $\sim 0.1\%$ decrease over time. In practice, this did not affect the *WMAP* data processing because each year was mapped separately and co-added afterwards. An effective frequency calculator was delivered in the DR5 release as part of the IDL library to mitigate this effect during astrophysical analyses.²

The beams were characterized in the form of maps, with separate products for the near-field and far-field. The main beam and near sidelobes were characterized using a combination of physical optics codes and observations of Jupiter for each horn separately. The maps of Jupiter were then combined with the best-fit physical optics codes to create a map of the beam response (Hill et al. 2009; Weiland et al. 2011; Bennett et al. 2013). Far sidelobes were estimated using a combination of laboratory measurements and Moon data taken during the mission (Barnes et al. 2003), as well as a physical optics model described in Hinshaw et al. (2009). To remove the far sidelobe in the TOD, an estimate was calculated by convolving the intensity map and the orbital dipole signal with the measured sidelobe signal (Jarosik et al. 2007). Although the sidelobe pickup was modeled in Barnes et al. (2003), it was determined that the results were small enough to be neglected and have not been explicitly reported in any of the *WMAP* data releases.

The *WMAP* data were calibrated by jointly estimating the time-dependent gains and baselines, as described in Hinshaw et al. (2007), Hinshaw et al. (2009), and Jarosik et al. (2011). The TOD were intially modeled as having constant gain and baseline for a 1–24 hour period, and are fit to the orbital dipole assuming T_0 from Mather et al. (1999) and a map made from a previous it-

¹ <https://cosmoglobe.uio.no>

² https://lambda.gsfc.nasa.gov/product/wmap/dr5/m_sw.html

eration of the mapmaking procedure. Once the gain and baseline solution had converged, the data were fit to a parametric form of the radiometer performance as a function of housekeeping data, given in Appendix A of Greason et al. (2012).

Transmission imbalance, i.e., the effect of different sky signal transmission from the A-side and B-side optics, is parameterized using x_{im} , which is zero in the case of an ideal differential radiometer. In practice, an unpolarized sky map generates a timestamp

$$d_t^{\text{imbal}} \propto (1 + x_{\text{im}})T_{p_A} - (1 - x_{\text{im}})T_{p_B} \quad (1)$$

$$= (T_{p_A} - T_{p_B}) + x_{\text{im}}(T_{p_A} + T_{p_B}). \quad (2)$$

If the x_{im} value were inaccurate, this would yield a spurious polarization component, and create imbalance modes due to coupling with the Solar dipole (Jarosik et al. 2007). The transmission imbalance factors were fit by using the Solar dipole in TOD space and fitting the common-mode and differential signals in TOD space directly (Jarosik et al. 2003a, 2007).

Data were flagged and masked before the final mapmaking step. In particular, station-keeping maneuvers, solar flares, and unscheduled events caused certain data to be unusable – the full catalog of these events is listed in Table 1.8 of Greason et al. (2012). In addition, data were masked depending on the channel frequency and the planet itself, with the full list of exclusion radii enumerated in Table 4 of Bennett et al. (2013).

To create the sky maps \mathbf{m} , the calibrated data were put into the asymmetric mapmaking equation,

$$\mathbf{P}_{\text{am}}^T \mathbf{N}^{-1} \mathbf{P} \mathbf{m} = \mathbf{P}_{\text{am}}^T \mathbf{N}^{-1} \mathbf{d}, \quad (3)$$

where \mathbf{P} is implicitly defined for detectors \mathbf{d}_1 and \mathbf{d}_2 sensitive to different polarization orientations,

$$\begin{aligned} \mathbf{d}_1 &= \mathbf{P}_1 \mathbf{m} \\ &= (1 + x_{\text{im}})[T_A + Q_A \cos 2\gamma_A + U_A \sin 2\gamma_A + S_A] \\ &\quad + (1 - x_{\text{im}})[-T_B - Q_B \cos 2\gamma_B - U_B \sin 2\gamma_B - S_B], \end{aligned} \quad (4)$$

and

$$\begin{aligned} \mathbf{d}_2 &= \mathbf{P}_2 \mathbf{m} \\ &= (1 + x_{\text{im}})[T_A - Q_A \cos 2\gamma_A - U_A \sin 2\gamma_A - S_A] \\ &\quad + (1 - x_{\text{im}})[-T_B + Q_B \cos 2\gamma_B + U_B \sin 2\gamma_B + S_B]. \end{aligned} \quad (6)$$

In this formalism, S acts as an extra Stokes parameter that absorbs the effects of differing bandpass responses between radiometers \mathbf{d}_1 and \mathbf{d}_2 (Jarosik et al. 2007). The asymmetric mapmaking matrix, \mathbf{P}_{am} , was used because, as noted in Jarosik et al. (2011), large signals observed in one beam could leak into the solution for the pixel observed by the other beam, leading to incorrect signals in the final map. The asymmetric mapmaking solution essentially works by only updating the matrix multiplication for beam A when beam A is in a high emission region and beam B is not, and vice versa. Bennett et al. (2013) also identified that these effects are pronounced when there is a steep gradient in the emission across the $N_{\text{side}} = 512$ pixels within an $N_{\text{side}} = 16$ superpixel, leading to excesses 140° away from the Galactic center.

An accurate noise model was necessary to perform the maximum likelihood mapmaking, as it required the evaluation of the dense time-space inverse noise covariance matrix \mathbf{N}^{-1} . The time-space autocorrelation function was estimated for each year of data, which is then Fourier transformed, inverted, and Fourier

transformed again to create an effective inverse noise operator $N_{tt'}^{-1}$. Finally, to create the sky maps themselves, the data are treated one year at a time, and the iterative Bi-conjugate Gradient Stabilized Method (BiCG-STAB van der Vorst 1992; Barrett et al. 1994) is applied to the maps.

2.3. Instrument model

As opposed to the *WMAP* pipeline, the *COSMOGLOBE* uses a generative model for every aspect of the data, including the sky and instrumental effects at once. In the *COSMOGLOBE* paradigm, it is simplest to characterize the data's goodness-of-fit to a model,

$$\mathbf{d} = \mathbf{GP}[\mathbf{B}^{\text{symm}} \mathbf{Ma} + \mathbf{B}^{4\pi}(\mathbf{s}^{\text{orb}} + \mathbf{s}^{\text{fsl}})] + \mathbf{s}^{\text{inst}} + \mathbf{n}^{\text{corr}} + \mathbf{n}^{\text{w}}, \quad (7)$$

where \mathbf{G} is the time-dependent gain in the form of the matrix $\text{diag}(g_t)$, \mathbf{P} is the $n_p \times n_t$ pointing matrix, where n_p is the number of pixels and n_t the number of TOD datapoints, \mathbf{B}^{symm} and $\mathbf{B}^{4\pi}$ are the symmetrized and full symmetric beam, respectively, \mathbf{M} is the mixing matrix between a given component c with spectral energy distribution $f_c(v/v_{0,c})$ and a detector j with bandpass $\tau_j(v)$, given by

$$\mathbf{M}_{cj} = \int dv \tau_j(v) f_c(v/v_{c,0}). \quad (8)$$

The maps \mathbf{a} are the component amplitudes, \mathbf{s}^{orb} is the orbital dipole induced by the motion of the telescope with respect to the Sun, and \mathbf{s}^{fsl} is the time-dependent far sidelobe signal. In the Commander3 (Galloway et al. 2022) implementation, \mathbf{n}^{corr} is a realization of the correlated noise component whose power spectrum is parametrized by $P(f | \xi_n)$, where ξ_n generally includes f_{knee} , a slope α , and an amplitude fixed by the white noise σ_0 . Similarly, each experiment has particular signals that are specific to the instrument in question, e.g., the 1 Hz spike in *Planck* LFI or the large baseline in *WMAP*, which can be modeled by \mathbf{s}^{inst} .

The most unique feature of the *WMAP* data is that it includes differential pointing. *WMAP* has two primary mirrors approximately reflected along the vertical satellite axis, and are tilted approximately 19.5° downwards – in total, when horn A is pointed at pixel p_A , horn B is pointed at a pixel p_B that is approximately 141° away (Page et al. 2003). The incoming radiation is differenced in the electronics before being deposited on the detectors, essentially recording radiation proportional to $\mathbf{m}_A - \mathbf{m}_B$ and $\mathbf{m}_B - \mathbf{m}_A$ (Jarosik et al. 2003b). Each pair of radiometers has a partner pair of radiometers that observes the same pixels with sensitivity to the orthogonal polarization direction. Taking these effects all into account, the total data model for a single radiometer is given by

$$d_t = g_t \mathbf{P}_{t,p} s_p + s_t^{\text{inst}} + n_t \quad (9)$$

$$\begin{aligned} &= g_t [\alpha_A(T_{p_A(t)} + Q_{p_A(t)} \cos 2\gamma_A(t) + U_{p_A(t)} \sin 2\gamma_A(t)) \\ &\quad - \alpha_B(T_{p_B(t)} + Q_{p_B(t)} \cos 2\gamma_B(t) + U_{p_B(t)} \sin 2\gamma_B(t))] \\ &\quad + s_t^{\text{inst}} + n_t, \end{aligned} \quad (10)$$

where s_p is the total sky signal $\mathbf{B} \mathbf{M} \mathbf{a}$, $\gamma_{A/B}$ are the time-dependent polarization angles, and $p_{A/B}$ are the A and B pixel locations. In this notation, $\alpha_{A/B}$ is the total optical power transmission for horn A and B. Defining the transmission imbalance for a given radiometer pair $x_{\text{im}} \equiv (\alpha_A - \alpha_B)/(\alpha_A + \alpha_B)$ and absorbing $\alpha_A + \alpha_B$ into the definition of g_t allows the pointing operation to be written in terms of the deviation from ideality,

$$\begin{aligned} \mathbf{P}_{t,p} s_p &= (1 + x_{\text{im}})(T_{p_A} + Q_{p_A} \cos 2\gamma_A + U_{p_A} \sin 2\gamma_A) \\ &\quad - (1 - x_{\text{im}})(T_{p_B} + Q_{p_B} \cos 2\gamma_B + U_{p_B} \sin 2\gamma_B). \end{aligned} \quad (11)$$

2.4. Sky model

Following BeyondPlanck (2022), we assume that the sky (\mathbf{a} in Eq. 7) can be modeled as a linear combination of CMB fluctuations (\mathbf{a}_{CMB} and \mathbf{a}_{quad}), synchrotron (\mathbf{a}_s), free-free emission (\mathbf{a}_{ff}), anomalous microwave emission (\mathbf{a}_{ame}), thermal dust (\mathbf{a}_d), and radio point sources ($\mathbf{a}_{j,\text{src}}$). The parametric sky model we adopt is given in brightness temperature units as

$$s_{\text{RJ}} = (\mathbf{a}_{\text{CMB}} + \mathbf{a}_{\text{quad}}(\nu)) \frac{x^2 e^x}{(e^x - 1)^2} + \quad (12)$$

$$+ \mathbf{a}_s \left(\frac{\nu}{\nu_{0,s}} \right)^{\beta_s} + \quad (13)$$

$$+ \mathbf{a}_{\text{ff}} \left(\frac{\nu_{0,\text{ff}}}{\nu} \right)^2 \frac{g_{\text{ff}}(\nu; T_e)}{g_{\text{ff}}(\nu_{0,\text{ff}}; T_e)} + \quad (14)$$

$$+ \mathbf{a}_{\text{ame}} e^{\beta(\nu - \nu_{0,\text{ame}})} + \quad (15)$$

$$+ \mathbf{a}_d \left(\frac{\nu}{\nu_{0,d}} \right)^{\beta_d+1} \frac{e^{h\nu_{0,d}/k_B T_d} - 1}{e^{h\nu/k_B T_d} - 1} + \quad (16)$$

$$+ U_{\text{mJy}} \sum_{j=1}^{N_{\text{src}}} \mathbf{a}_{j,\text{src}} \left(\frac{\nu}{\nu_{0,\text{src}}} \right)^{\alpha_{j,\text{src}}-2}. \quad (17)$$

Note that the AME model we adopt is a pure exponential, rather than the spectral energy distribution (SED) template $s_0^{\text{sd}}(\nu)$ computed using SpDust2 (Ali-Haïmoud et al. 2009; Ali-Haïmoud 2010; Silsbee et al. 2011). The SpDust2 model was parameterized in BeyondPlanck (2022) by a peak frequency ν_p such that

$$s_{\text{RJ}}^{\text{sd}}(\nu) \propto \nu^{-2} s_0^{\text{sd}} \left(\nu \cdot \frac{30 \text{ GHz}}{\nu_p} \right). \quad (18)$$

In the WMAP and LFI frequency range, the exponential model and the SpDust2 are phenomenologically quite similar, despite their very different descriptions. The exponential model is a simple fit with β drawn from a prior value of -3.57 , and is a clear parametric form that is easy to interpret. An alternative model is the two-parameter log-normal AME SED,

$$s_{\text{RJ}}^{\text{ame,log-N}} = \mathbf{a}_{\text{ame}} \left(\frac{\nu}{\nu_{\text{ame}}} \right)^{-2} \exp \left(-\frac{1}{2} \left[\ln(\nu/\nu_{\text{ame}}) \right]^2 \right), \quad (19)$$

derived by Stevenson (2014) as an analytical approximation to the spinning dust emission. This has also been employed in the latest QUIJOTE analysis, e.g., Tramonte et al. (2023), as it allows for variation of the peak frequency ν_{ame} and width W_{ame} . Although this work is not dependent on the specific parametric form of the AME, we opt for the exponential form described above, as it provides an excellent fit to the diffuse AME with a single parameter.

2.5. Priors

2.6. Posterior distribution and Gibbs sampling

As shown in BeyondPlanck (2022), this parametric description of the instrumental effects and sky allows us to write down a total model for the data, $\mathbf{d} = \mathbf{s}^{\text{tot}}(\omega) + \mathbf{n}^w$, where \mathbf{s}^{tot} encompasses all of the terms in Eq. (7) except for the white noise term. Assuming that all instrumental effects have been modeled, the data should be Gaussian distributed with a mean of $\mathbf{s}^{\text{tot}}(\omega)$ and variance σ_0^2 . Given this model, we can evaluate the likelihood for arbitrary chunks of time-ordered data in the context of the entire model,

so that individual chunks of data with poor fits can be more easily identified. In general, the likelihood is written

$$P(\mathbf{d} | \omega) \propto \exp \left(-\frac{1}{2} \sum_t \frac{(d_t - s_t^{\text{tot}}(\omega))^2}{\sigma_0^2} \right). \quad (20)$$

If $\mathbf{d} \sim \mathcal{N}(\mathbf{s}^{\text{tot}}, \sigma_0^2)$ is the correct model for the data, the argument of the exponent is proportional to a χ^2 -distribution with n_{TOD} degrees of freedom. In the limit of large n , a χ^2 distribution is well-approximated by a Gaussian with mean n and variance $2n$. Therefore we define and use the reduced- χ^2 statistic,

$$\chi^2 \equiv \frac{\sum_t ((d_t - s_t^{\text{tot}})^2 / \sigma_0^2 - n_{\text{TOD}})}{\sqrt{2n_{\text{TOD}}}}, \quad (21)$$

which is approximately drawn from the standard normal distribution $\mathcal{N}(0, 1)$.

The COSMOGLOBE Gibbs chain is given by

$$\mathbf{g} \leftarrow P(\mathbf{g} \mid \mathbf{d}, \xi_n, s^{\text{inst}}, \boldsymbol{\beta}, \mathbf{a}, C_\ell, \theta) \quad (22)$$

$$\mathbf{n}_{\text{corr}} \leftarrow P(\mathbf{n}_{\text{corr}} \mid \mathbf{d}, \mathbf{g}, \xi_n, s^{\text{inst}}, \boldsymbol{\beta}, \mathbf{a}, C_\ell, \theta) \quad (23)$$

$$\xi_n \leftarrow P(\xi_n \mid \mathbf{d}, \mathbf{g}, \mathbf{n}_{\text{corr}}, s^{\text{inst}}, \boldsymbol{\beta}, \mathbf{a}, C_\ell, \theta) \quad (24)$$

$$s^{\text{inst}} \leftarrow P(s^{\text{inst}} \mid \mathbf{d}, \mathbf{g}, \mathbf{n}_{\text{corr}}, \xi_n, \boldsymbol{\beta}, \mathbf{a}, C_\ell, \theta) \quad (25)$$

$$\boldsymbol{\beta} \leftarrow P(\boldsymbol{\beta} \mid \mathbf{d}, \mathbf{g}, \mathbf{n}_{\text{corr}}, \xi_n, s^{\text{inst}}, C_\ell, \theta) \quad (26)$$

$$\mathbf{a} \leftarrow P(\mathbf{a} \mid \mathbf{d}, \mathbf{g}, \mathbf{n}_{\text{corr}}, \xi_n, s^{\text{inst}}, \boldsymbol{\beta}, C_\ell, \theta) \quad (27)$$

$$C_\ell \leftarrow P(C_\ell \mid \mathbf{d}, \mathbf{g}, \mathbf{n}_{\text{corr}}, \xi_n, s^{\text{inst}}, \boldsymbol{\beta}, \mathbf{a}, \theta) \quad (28)$$

$$\theta \leftarrow P(\theta \mid \mathbf{d}, \mathbf{g}, \mathbf{n}_{\text{corr}}, \xi_n, s^{\text{inst}}, \boldsymbol{\beta}, \mathbf{a}, C_\ell), \quad (29)$$

with each step requiring its own dedicated sampling algorithm. The Commander3 pipeline is designed so that results of each Gibbs sample can be easily passed to each other, and that the internal calculations of each step do not directly depend on the inner workings of each other. Therefore, in order to add another data set to the Gibbs chain, one can either add a map or TODs. To add a TOD, one must implement Eqs. (22)–(25) for each instrument, as was done in BeyondPlanck (2022) and Basyrav et al. (2022) for Planck LFI and in Watts et al. (2022) for WMAP. To add a map, one must simply pass processed maps with beam, mask, and noise information to Eqs. (26)–(29), as was done for the Haslam 408 MHz map (Haslam et al. 1982; Remazeilles et al. 2015) and the Planck 353 and 857 GHz maps.

Before we discuss the results of this Gibbs chain as applied to the Planck LFI and WMAP data, we summarize the TOD processing steps in Sect. 2.7.

2.7. Sampling algorithms

Each step of the Gibbs chain requires its own distribution to be sampled from. In Sect. 2.7.1 we review the sampling algorithms implemented in the BEYONDPLANCK suite of papers, while Sects. 2.7.2–2.7.4 provide an overview of the WMAP-specific processing steps.

2.7.1. Review of sampling algorithms

Several of the techniques required for WMAP data analysis have already been implemented and described in the BEYONDPLANCK framework and implemented in Commander3. This section includes a summary of the algorithms that were used previously for the analysis of LFI data. In each of these cases, every part of

the model not explicitly mentioned is held fixed unless specified otherwise.

Noise estimation and calibration, described in [Ihle et al. \(2022\)](#) and [Gjerløw et al. \(2022\)](#) respectively, are highly degenerate, given that the timestream

$$d_{t,i} = g_{q,i}s_i^{\text{tot}} + n_{t,i}^{\text{corr}} + n_{t,i}^{\text{wn}} \quad (30)$$

is equally well fit by two solutions if $g' = gs^{\text{tot}}/(s^{\text{tot}})'$ or $(n^{\text{corr}})' = n^{\text{corr}} + gs^{\text{tot}} + g'(s^{\text{tot}})'$. In practice, this is dealt with by marginalizing over the correlated noise realization \mathbf{n}^{corr} assuming a fixed PSD ξ_n , so that Eqs. (22) and (23) are evaluated as

$$\mathbf{g} \leftarrow P(\mathbf{g} \mid \mathbf{d}, \xi_n, \dots) \quad (31)$$

$$\mathbf{n}_{\text{corr}} \leftarrow P(\mathbf{n}_{\text{corr}} \mid \mathbf{d}, \mathbf{g}, \xi_n, \dots). \quad (32)$$

This is allowed by probability theory given that the joint distribution $P(\mathbf{g}, \mathbf{n}_{\text{corr}} \mid \omega) = P(\mathbf{n}_{\text{corr}} \mid \mathbf{g}, \omega)P(\mathbf{g} \mid \omega)$, so that Eqs. (31) and (32) evaluated in sequence is equivalent to drawing a joint sample from $P(\mathbf{g}, \mathbf{n}_{\text{corr}} \mid \omega)$. In practice, this means that when sampling for \mathbf{g} , the covariance matrix $\mathbf{N} = \mathbf{N}_{\text{wn}} + \mathbf{N}_{\text{corr}}$ must be used, rather than just \mathbf{N}_{wn} .

`Commander3` models the gain at each timestream t for a detector i as

$$g_{t,i} = g_0 + \Delta g_i + \delta g_{q,i} \quad (33)$$

where q labels the time interval for which we assume the gain is constant over, e.g., a single scan. In order to sample the gain, we write down a generative model for the TOD,

$$\mathbf{d}_i = \mathbf{g}_i s_i^{\text{tot}} + \mathbf{n}_i^{\text{tot}} \sim \mathcal{N}(\mathbf{g}_i s_i^{\text{tot}}, \mathbf{N}_i). \quad (34)$$

Since the \mathbf{d}_i is given as a linear combination of the fixed signal and the gains, a random sample of the gain can be drawn by solving³

$$[(s_i^{\text{tot}})^T \mathbf{N}_i^{-1} s_i^{\text{tot}}] \mathbf{g}_i = (s_i^{\text{tot}})^T \mathbf{N}_i^{-1} \mathbf{d}_i + (s_i^{\text{tot}})^T \mathbf{N}_i^{-1/2} \boldsymbol{\eta}. \quad (35)$$

Note that the \mathbf{N}_i depends implicitly on the noise PSD ξ_n , while the specific realization of \mathbf{n}_{corr} is accounted for in the covariance matrix. In practice, as shown in [Gjerløw et al. \(2022\)](#), `Commander3` samples g_0 , Δg_i , and $\delta g_{q,i}$ in separate sampling steps. Formally, the Gibbs chain is broken by fitting the absolute gain g_0 to the orbital dipole rather than the full sky signal. However, this makes the sampling much more robust to unmodeled systematic effects, so the trade-off in rigor is justified.

The correlated noise sampling, described in [Ihle et al. \(2022\)](#), follows a similar procedure to gain sampling, except now conditioned upon the gain estimate, sampled just before correlated noise in the code. Similar to the gain case, we can write a generative model for the data

$$\mathbf{d}_i = \mathbf{g}_i s_i^{\text{tot}} + \mathbf{n}_i^{\text{corr}} + \mathbf{n}_i^{\text{wn}} \sim \mathcal{N}(\mathbf{g}_i s_i^{\text{tot}}, \mathbf{N}_{\text{corr},i} + \mathbf{N}_{\text{wn},i}). \quad (36)$$

Given fixed $\mathbf{r}_i = \mathbf{d}_i - \mathbf{g}_i s_i^{\text{tot}}$, we can again write a sampling equation,

$$(\mathbf{N}_{\text{corr},i}^{-1} + \mathbf{N}_{\text{wn},i}^{-1}) \mathbf{n}_i^{\text{corr}} = \mathbf{N}_{\text{wn},i}^{-1} \mathbf{r}_i + \mathbf{N}_{\text{wn},i}^{-1/2} \boldsymbol{\eta}_1 + \mathbf{N}_{\text{corr},i}^{-1/2} \boldsymbol{\eta}_2. \quad (37)$$

This gives a sample of the true underlying correlated noise that occurred when the instrument was taking data. In practice, this is equivalent to the destriping mapmaking algorithm `Madam`, and returns equivalent results to the classical method ([Keihänen et al. 2022](#)).

³ See, e.g., Appendix A.2 of [BeyondPlanck \(2022\)](#) for a derivation of this result.

To solve for the correlated noise parameters, we assume that the correlated noise is drawn from a correlated Gaussian and form the posterior distribution

$$P(\xi_n \mid \mathbf{n}^{\text{corr}}) \propto \frac{\exp[-\frac{1}{2}(\mathbf{n}^{\text{corr}})^T \mathbf{N}_{\text{corr}}^{-1} \mathbf{n}^{\text{corr}}]}{\sqrt{|\mathbf{N}_{\text{corr}}|}} P(\xi_n). \quad (38)$$

The simplest parameterization for correlated noise is given by

$$\mathbf{N}_{\text{corr}}(f) = \sigma_0^2 \left(\frac{f}{f_{\text{knee}}} \right)^\alpha. \quad (39)$$

This can in principle be modified, and for *Planck* LFI a Gaussian log-normal bump was added at a late stage in the BEYOND-PLANCK analysis. Rather than sampling for σ_0 , we effectively fix the white noise level to the noise level at the highest frequency, e.g.,

$$\sigma_0^2 \equiv \frac{\text{Var}(r_{t+1} - r_t)}{2}, \quad (40)$$

where t and $t + 1$ are consecutive time samples, and $\mathbf{r} \equiv \mathbf{d} - \mathbf{g}s^{\text{tot}} - \mathbf{n}^{\text{corr}}$. In practice, this makes σ_0 a deterministic function of the sampled sky and gain parameters. The parameters α and f_{knee} are not linear in the data, so must be sampled using the general inversion sampler.⁴ In practice, this requires gridding out the posterior one parameter at a time.

The bandpass mismatch is explicitly modeled in `Commander3`. Using the calibrated sky model, the expected calibrated sky signal is given by

$$m_{p,j} = \mathbf{B}_{p,p'} \sum_c \mathbf{M}_{c,j} d_{p'}^c + n_{j,p}^w. \quad (41)$$

Since $\mathbf{M}_{c,j}$ encodes the bandpass response of every detector j to every sky component c , the maps \mathbf{m}_j will each be slightly different depending on their bandpass τ_j . More importantly, differences in signal between different detectors can be attributed to a spurious polarization signal, giving spurious polarized maps. Therefore, before averaging different detectors together, `Commander3` estimates the average over all detectors in a given frequency channel $\mathbf{m} \equiv \langle \mathbf{m}_j \rangle$, and subtracts it directly in the timestream;

$$\delta s_{t,j}^{\text{leak}} = \mathbf{P}_{t,p}^j \mathbf{B}_{p,p'}^j (\mathbf{m}_{j,p'} - \mathbf{m}_{p'}). \quad (42)$$

This leakage term uses the expected bandpass response to remove the expected component that deviates from the mean in the timestream, directly reducing polarization contamination.

Once the instrumental parameters have been sampled, `Commander3` computes the calibrated TOD for each band,

$$r_{t,j} = \frac{d_{t,j} - n_{t,j}^{\text{corr}}}{g_{t,j}} - (s_{t,j}^{\text{orb}} + s_{t,j}^{\text{fsl}} + \delta s_{t,j}^{\text{leak}} + s_{t,j}^{\text{inst}}) \quad (43)$$

where s^{orb} is the orbital dipole, s^{fsl} is the far sidelobe timestream, δs^{leak} is the bandpass leakage, and s^{inst} is the set of instrumental parameters, e.g., the 1 Hz spike in LFI. With a correlated noise realization removed, one can perform simple binned mapmaking, weighting each pixel by the white noise amplitude.

⁴ See, e.g., Appendix A.3 of [BeyondPlanck \(2022\)](#) and Chapter 7.3.2 of [Press et al. \(2007\)](#) for further details.

2.7.2. Differential mapmaking

The first additional algorithm that needed to be added to Commander3 when adding WMAP TOD data was differential mapmaking, since the *Planck* LFI data came from a standard single-horn instrument.

After calibration and correction for instrumental effects, the TOD can be modeled as

$$\mathbf{d} = \mathbf{P}\mathbf{m} + \mathbf{n}^w, \quad (44)$$

where

$$\mathbf{m} = \mathbf{B}^{\text{symm}}\mathbf{M}\mathbf{a} \quad (45)$$

is the expected map for each detector after removing the orbital dipole, far sidelobe, baseline, and a realization of correlated noise. The differential pointing strategy can be represented in matrix form as

$$\mathbf{P}_{tp} = (1 + x_{\text{im}})(\delta_{p' p'_A} + \delta_{p' p'_A}^o \cos 2\psi_A + \delta_{p' p'_A}^u \sin 2\psi_A) \quad (46)$$

$$- (1 - x_{\text{im}})(\delta_{p' p'_B} - \delta_{p' p'_B}^o \cos 2\psi_B - \delta_{p' p'_B}^u \sin 2\psi_B) \quad (47)$$

where p_A and p_B are the time-dependent pointings for each DA. The maximum likelihood map can in principle be solved using the usual mapmaking equation,

$$\mathbf{P}^T \mathbf{N}^{-1} \mathbf{P}\mathbf{m} = \mathbf{P}^T \mathbf{N}^{-1} \mathbf{d}. \quad (48)$$

For a single-horn experiment, i.e., *Planck* LFI, this reduces to a 3×3 matrix that can be inverted for each pixel independently. For the pointing matrix in Eq. (46), this is no longer possible, as there is inherently coupling between horns A and B in the timestreams. The $3N_{\text{pix}} \times 3N_{\text{pix}}$ matrix can be solved using an iterative algorithm, e.g., preconditioned conjugate gradients.

Jarosik et al. (2011) identified an issue where a large difference in the sky temperature values at pixel value at pixel A versus pixel B induced artifacts in the mapmaking procedure. We adopt the procedure first described in Hinshaw et al. (2003) where only the pixel in a bright region, defined by a small processing mask (Bennett et al. 2013) is accumulated, thus modifying the mapmaking equation to

$$\mathbf{P}_{\text{am}}^T \mathbf{N}^{-1} \mathbf{P}\mathbf{m} = \mathbf{P}_{\text{am}}^T \mathbf{N}^{-1} \mathbf{d}. \quad (49)$$

This equation can be solved using the BiCG-STAB algorithm for a non-symmetric matrix \mathbf{A} where $\mathbf{A}\mathbf{x} = \mathbf{b}$. We apply a preconditioner \mathbf{M} by numerically inverting the same problem with $N_{\text{side}} = 16$ maps and applying a diagonal noise matrix. Numerically, we define convergence as when the residual $\mathbf{r} \equiv \mathbf{b} - \mathbf{A}\mathbf{x}$ satisfies $\mathbf{r}^T \mathbf{M}^{-1} \mathbf{r} / \mathbf{b}^T \mathbf{M}^{-1} \mathbf{b} < 10^{-10}$, which typically takes about 20 iterations for producing frequency maps.

2.7.3. Transmission imbalance estimation

Transmission imbalance, i.e., the differential power transmission of the optics and waveguide components, can be parameterized as

$$d_{t,j} = g_{t,j}[(1 + x_{\text{im},j})s_{t,j}^{\text{tot,A}} - (1 - x_{\text{im},j})s_{t,j}^{\text{tot,B}}] + n_t. \quad (50)$$

This can be decomposed into a differential (d) and common-mode (c) signal such that

$$d_{t,j} = g_{t,j}[s_{t,j}^d + x_{\text{im},j}s_{t,j}^c] + n_t. \quad (51)$$

In this form, the imbalance parameters can be estimated by drawing Gaussian samples from the standard mean and standard deviation over the entire mission. To draw samples for $x_{\text{im},j}$, we construct the sampling routine analogous to Eqs. (35) and (37) with $\mathbf{r} = \mathbf{d} - \mathbf{gs}^d$,

$$[(\mathbf{gs}^c)^T \mathbf{N}^{-1} \mathbf{gs}^c]x_{\text{im}} = (\mathbf{gs}^c)^T \mathbf{N}^{-1} \mathbf{r} + (\mathbf{gs}^c)^T \mathbf{N}^{-1/2} \boldsymbol{\eta}, \quad (52)$$

essentially cross-correlating the common-mode signal with \mathbf{r} with appropriate weights and adding a Gaussian random variable with the correct weighting. Note that we are marginalizing over the correlated noise here by using $\mathbf{N} = \mathbf{N}_{\text{wn}} + \mathbf{N}_{\text{corr}}$. This mitigates any baseline drifts being erroneously attributed to the common-mode signal and biasing the estimate of x_{im} .

The WMAP procedure, described in Jarosik et al. (2003a), fit for common-mode and differential coefficients along with a cubic baseline over 10 precession periods at a time, corresponding to 10 hours of observation. The mean and uncertainty were then calculated by averaging and taking the standard deviation of these values. This approach has the benefit of allowing for the tracking of possible transmission imbalance variation throughout the mission. However, none of the WMAP suite of papers have indicated this, and it has not arisen in our analysis, so we model this as an effect whose value is constant throughout the mission.

2.7.4. Baseline sampling

The data model adopted in Hinshaw et al. (2003) can be written in raw digital units (du) as

$$\mathbf{d} = \mathbf{GPBM}\mathbf{a} + \mathbf{n} + \mathbf{b}, \quad (53)$$

where \mathbf{b} is the instrumental baseline and \mathbf{n} is the total instrumental noise. As detailed in Ihle et al. (2022), Commander3 divides the noise into $\mathbf{n} = \mathbf{n}^w + \mathbf{n}^{\text{corr}}$, a white noise term and a correlated noise term. By definition, the white noise does not have any correlations between adjacent pixels, so that any pixel-pixel covariance should be fully described by realizations of the \mathbf{n}^{corr} timestream.

Commander estimates the baseline using the full estimate of the current sky model, $\mathbf{r} = \mathbf{d} - \mathbf{gs}^{\text{tot}} = \mathbf{b} + \mathbf{n}$. Modeling $\mathbf{b} = b_0 + b_1 \Delta t$, we solve for b_0 and b_1 using linear regression in each timestream while masking out samples that lie within the processing mask. Strictly speaking, this is breaking the Gibbs chain, as we are not formally sampling b_0 and b_1 for each TOD chunk. In practice, baseline estimation uncertainty propagates to correlated noise realizations and PSD parameters, as discussed below.

The approach detailed in Hinshaw et al. (2003) and the Commander implementation differ mainly in the assumed stable timescale – the initial WMAP baseline is estimated over one hour timescales, whereas Commander assumes constant values throughout the entire timestream, 3–7 days depending on the band in question. As noted in Hinshaw et al. (2003), residual baseline variations manifest as correlated noise stripes in the final maps. WMAP9 solves this using a time-domain filter, downweighting the data based off of the noise characterization. This approach is equivalent to the Commander3 procedure of removing a constrained realization of correlated noise from the timestream directly, based on the best-fit to the noise PSD.

3. Data and data processing

We describe the delivered WMAP data in Sect. 3.1, then describe the treatment we apply it to make them compatible with

Table 1. Flagging statistics

Band	Flagged (%)	Discarded (%)	Used (%)
<i>K</i>	1.72	0.87	97.4
<i>Ka</i>	1.64	0.88	97.5
<i>Q1</i>	1.84	0.84	96.5
<i>Q2</i>	1.62	0.81	97.6
<i>V1</i>	1.62	1.10	97.3
<i>V2</i>	1.61	1.01	97.4
<i>W1</i>	1.76	1.03	97.2
<i>W2</i>	1.60	0.81	97.6
<i>W3</i>	1.61	0.87	97.5
<i>W4</i>	1.60	0.81	97.6

Commander3 in Sect. 3.2, then describe the computational requirements in Sect. 3.3.

3.1. Publicly available WMAP products

The full *WMAP* dataset is hosted at the Legacy Archive for Microwave Background Data Analysis (LAMBDA).⁵ In addition to the primary scientific products, e.g., cosmological parameters, CMB power spectra and anisotropy maps, and frequency maps, the time-ordered data (TOD) can be downloaded, both in uncalibrated and calibrated form.⁶ In principle, thanks to these data and the explanatory supplements (Greason et al. 2012), the entire data analysis pipeline can be reproduced from TOD in digital units (du) to frequency maps.

For this analysis, we keep certain instrumental parameters fixed to the reported values. For example, we have made no attempts to rederive the pointing solutions, re-estimate the main beam response and far sidelobe pickup, or recover data that was flagged in the *WMAP* event log. These and other analyses, such as estimating the bandpass shift over the course of the mission, are certainly possible within the larger Gibbs sampling framework. However, in this work we limit ourselves to recalibrating the TOD, estimating the noise properties, and applying bandpass corrections to the data before mapmaking.

3.2. TOD pre-processing and data selection

The full nine-year *WMAP* archive spans from August 10, 2001 to August 10, 2010, with the raw uncalibrated data spanning 626 GB. A little over 1 % of the data were lost or rejected due to incomplete satellite telemetry, thermal disturbances, spacecraft anomalies, and station-keeping maneuvers, with an extra 0.1 % rejected due to planet flagging (Bennett et al. 2003b; Hinshaw et al. 2007, 2009; Bennett et al. 2013). The final results reported in Bennett et al. (2013) included roughly 98.4 % of the total data volume. A full accounting of all data cuts can be found in Table 1.8 of Greason et al. (2012). In total, we flag the same data indicated in the fiducial *WMAP* analysis, and use the same planet flags.

As shown in Galloway et al. (2022), a large fraction of *Commander3*'s computational time is spent performing FFTs on individual scans. Rather than truncating datastreams to have lengths equal to “magic numbers” for which FFTW (Frigo & Johnson 2005) is fastest, as in Galloway et al. (2022), we re-

distribute the data into scans of length 2^N , where $N = 22$ for *K*–*Q*, $N = 23$ for *V*–*W*. This yields scans with lengths of 6.21 days for *K*- and *Ka*-band, 4.97 days for *Q*-band, 7.46 days for *V*-band, and 4.97 days for *W*-band. These datastream lengths are short enough to be processed quickly and distributed efficiently across multiple processors, while being long enough to properly characterize the noise properties of the timestreams, whose f_{knee} values are on the order 1 mHz. Most importantly, FFTW performs fastest when the datastream is of length 2^N .

When redistributing the data, timestreams of length 2^N were interrupted by events logged in Table 1.8 of Greason et al. (2012). When we encountered these events, TOD segments that were interrupted by the event were appended to the previous TOD, in most cases creating TODs with lengths $> 2^N$. We found that events of length $< 2^N$ were too short to accurately estimate the noise PSD parameters. This criterion led us to discard these otherwise useful data. In addition, when $> 10\%$ of the TOD was flagged, the large number of gaps in the data made the constrained realizations unreliable, as well as biasing the noise PSD parameters. Together, these two effects led to $\simeq 1\%$ of the data to be discarded despite being of acceptable quality. We present the full flagging statistics for our maps in Table 1. In total, the COSMOGLOBE maps use slightly less data than the *WMAP9* official products, which had a total efficiency of $\simeq 98.4\%$ (Bennett et al. 2013). The total difference in data volume can be entirely accounted for by the cuts described in this paragraph.

3.3. Computational resources

A key motivation of the COSMOGLOBE project is to evaluate whether it is feasible to perform a joint analysis of two datasets simultaneously, each with its own particular processing requirements and algorithmic treatment. One of the results from Watts et al. (2022) was that most of the data processing procedures for *WMAP* and *Planck* LFI overlapped, with the notable exception of mapmaking. While the algorithmic requirements have been discussed in Sect. 2, we have not yet quantified the requirements in terms of RAM and CPU hours. In Table 2, we enumerate the RAM requirements and CPU time for each sampling step using the local cluster at the Institute of Theoretical Astrophysics at the University of Oslo. The node that these numbers come from used 128 cores of an AMD EPYC 7H12, 2.6 GHz machine with 2 TB of memory. As *Commander3* is parallelized and used 128 cores, wall hours in Table 2 can be obtained by dividing by 128.

Despite the relatively small data volume spanned by *WMAP*, the CPU time is comparable to each of the LFI channels. By far the largest reason for this is the mapmaking step, which requires looping over the entire dataset for each matrix multiplication, a process which must be repeated ~ 20 times. This is vastly sped up by the use of a low resolution preconditioner, reducing the number of iterations by an order of magnitude.

Additionally, operations that require creating timestreams for each detector, i.e., TOD projection, sidelobe evaluation, and orbital dipole projection, take much longer than expected from a pure data volume scaling. Part of this is due to each *WMAP* radiometer needing to evaluate the sky in two pixels simultaneously, doubling the expected workload. The operations of gain sampling and correlated noise sampling include multiple FFTs. Typical LFI TODs are of length $\sim 200\,000$, an order of magnitude smaller than the *WMAP* TODs of length $2^{22}-23$.

⁵ https://lambda.gsfc.nasa.gov/product/wmap/dr5/m_products.html

⁶ https://lambda.gsfc.nasa.gov/product/wmap/dr5/tod_info.html



Fig. 1. Time-ordered data segment for the K113 radiometer. From top to bottom, the panels show 1) raw uncalibrated TOD \mathbf{d} ; 2) sky signal s_{sky} ; 3) calibrated correlated noise n_{corr} ; 4) orbital CMB dipole signal s_{orb} ; 5) sidelobe correction s_{sl} ; 6) leakage mismatch correction s_{leak} ; and 7) residual TOD, $d_{\text{res}} = (\mathbf{d} - \mathbf{n}_{\text{corr}} - \mathbf{b})/g - s_{\text{sky}} - s_{\text{orb}} - s_{\text{leak}} - s_{\text{sl}}$, in units of $\sigma_0[\text{du}]$ for this TOD segment. Note that the vertical range varies significantly from panel to panel.

4. Instrumental parameters

4.1. Trace plots and correlations

To illustrate the dependence of the goodness-of-fit on the noise model, we inspect the 50th TOD segment, corresponding to MJDs 52285.2–52290.6, as a function of Gibbs iteration, in Fig. 3. This is one of the worst-fitting TOD segments of the entire mission, with a reduced relative χ^2 of -7.5 , equivalent to $\chi^2/n = 0.993$. The line plots demonstrate a strong correlation between the noise parameters and the χ^2 , while the gain itself is almost completely uncorrelated with the variations in the χ^2 . As σ_0 is not formally sampled in the Gibbs chain, it is weakly dependent on f_{knee} and α , making it more likely that it is the driver of the correlations in this figure.

4.2. Gain and baselines

To compare the calibrated TODs from *WMAP* versus *COSMOGLOBE*, it is important to look at the *WMAP* gain model,

$$g = \alpha \frac{\bar{V} - V_{\circ} - \beta(T_{\text{RXB}} - 290 \text{ K})}{T_{\text{FPA}} - T_{\circ}} + (m\Delta t + c), \quad (54)$$

where α , V_{\circ} , β , T_{\circ} , m , and c are fit to a constant value across the mission for each radiometer. \bar{V} represents the radio frequency bias powers per detector, and T_{RXB} and T_{FPA} are the receiver box and focal plane assembly temperatures, which are recorded every 23.04 s. Evaluating the model as a function of T_{RXB} and T_{FPA} requires finding the housekeeping data for the thermistor that was physically closest to the relevant radiometer's focal plane on the satellite. As this requires detailed technical information about the specifications of the satellite's schematics layout that can easily be misunderstood, we do not attempt to reproduce

Table 2. Computational resources required for end-to-end COSMOGLOBE processing. All times correspond to CPU hours, and all data volumes are reported in GB. Reported times are averaged over more than 100 samples, and vary by $\lesssim 5\%$ from sample to sample.

ITEM	30	44	70	K	Ka	Q1	Q2	V1	V2	W1	W2	W3	W4	SUM
<i>Data volume</i>														
Compressed TOD volume	86	178	597	13	12	15	15	19	18	26	26	26	26	1 053
<i>Processing time (cost per run)</i>														
TOD initialization/IO time	1.8	2.5	9.3	0.3	0.3	0.4	0.4	0.4	0.4	0.5	0.5	0.5	0.5	17.8
Other initialization														13.4
Total initialization														31.2
<i>Gibbs sampling steps (cost per sample)</i>														
Huffman decompression	1.1	2.1	10.5	0.9	0.8	1.0	1.0	1.3	1.3	1.8	1.8	1.8	1.8	27.2
TOD projection (P operation)	0.4	0.9	4.2	2.6	2.6	3.3	3.4	4.3	4.3	6.4	6.3	6.3	6.4	54.0
Sidelobe evaluation	1.0	2.1	7.6	2.9	2.9	3.5	3.5	4.7	4.8	7.0	6.9	6.9	6.9	60.7
Orbital dipole	0.9	1.9	7.1	1.3	1.3	1.7	1.7	2.2	2.3	3.4	3.3	3.3	3.3	33.7
Gain sampling	0.5	0.8	1.9	0.8	0.8	0.5	0.5	0.9	0.9	0.7	0.7	0.7	0.7	10.4
1 Hz spike sampling	0.3	0.4	1.6											2.4
Correlated noise sampling	2.0	4.0	21.7	2.8	2.9	3.3	3.6	5.1	5.4	8.0	7.7	7.2	8.5	81.3
Correlated noise PSD sampling	4.8	5.9	1.5	0.2	0.2	0.3	0.3	0.5	0.4	0.7	0.6	0.6	0.7	16.7
TOD binning (P' operation)	0.1	0.1	4.0	0.5	0.5	0.7	0.8	0.8	0.8	1.2	1.2	1.2	1.2	13.1
Mapmaking						6.4	7.0	8.9	8.1	11.1	9.5	14.4	14.3	119.5
Sum of other TOD processing	4.4	8.6	44.4	14.7	4.6	5.1	5.0	9.4	7.7	8.1	6.8	8.6	8.7	136.1
TOD processing cost per sample	15.5	26.8	104.5	23.0	24.1	27.6	27.9	40.3	37.4	51.7	50.6	51.9	54.6	535.9
Amplitude sampling														14.0
Spectral index sampling														25.5
Total cost per sample														581.2

the gain model given in Eq. (54) in this work. Although we are unable to reproduce the exact gain model parametrized in Greason et al. (2012), the 23.04 s time dependence of the gain model on housekeeping data is a plausible explanation for the time-dependent noise variation in the different calibrated data solutions.

As reported in Hinshaw et al. (2007), the calibrated data archive has been calibrated using the procedure listed above, with a baseline subtracted each hour and the sidelobe subtracted. Figure 5 shows the COSMOGLOBE timestream $d/g - s_{\text{sl}} - b$ with the WMAP delivered calibrated signal subtracted. The most prominent feature is a $\sim 25 \mu\text{K}$ offset, which is unsurprising, given the different treatment of baselines in our two pipelines. The second obvious difference is a series of spikes associated with Galactic plane crossings. The differences of order $50 \mu\text{K}$ correspond to sky brightness of order 10 mK , equivalent to $\sim 0.5\%$ deviations in the gain solution. This is twice as large as the 0.2% uncertainty estimated in Bennett et al. (2013) based on end-to-end simulations.

The slight downward drift in Fig. 5 can be understood as part of a long-term effect. On longer timescales, as displayed in Figure 6, the most prominent feature is a varying signal of amplitude 0.2 mK . This likely due to the hourly baseline subtraction mentioned above, which contrasts with the COSMOGLOBE approach of assigning a linear baseline solution for the entire scan. The variations are commensurate with correlated noise, which for $K113$ has $f_{\text{knee}} \sim 0.5 \text{ mHz}$, corresponding to a little over half an hour. Therefore, the hourlong baseline subtraction essentially acts as a destriper, removing an estimate of the correlated noise. To test this hypothesis, we plot a realization of correlated noise generated by Commander, and find that the signals are very similar, both in amplitude and morphology.

We also compare the gain and baseline solutions throughout the course of the mission in Fig. 2. To recover the WMAP9 gain solution, we directly compare the uncalibrated WMAP data with

the calibrated WMAP data with a far sidelobe contribution convolved with the delivered WMAP9 DA maps. We find that the calibrated and uncalibrated data can be related by

$$d_t^{\text{raw}} = g(d_t^{\text{cal}} + s_t^{\text{sl}}) + \sum_{i=0}^3 c_i(t - t_0)^i, \quad (55)$$

where the second term is a cubic polynomial with coefficients c_i referenced to the time at the beginning of the scan t_0 . To calculate s_t^{sl} , we convolve the WMAP far sidelobes with WMAP9 frequency maps with the Solar dipole from Hinshaw et al. (2009) added back in. We find that d^{raw} is consistent with the expression on the right at the level of $< 0.1 \text{ du}$ for all radiometers, suggesting that this estimate of g and the baseline c_0 is a good approximation of the WMAP9 calibration solution. An initial estimate using a linear baseline gave an unacceptable poor fit. Given that Eq. (2) of Jarosik et al. (2003a) employed a cubic baseline fit while fitting for transmission imbalance parameters, it is reasonable to assume that the official calibrated archive was created using a similar procedure.

The morphological characteristics of the WMAP9 and COSMOGLOBE gain solutions are similar, with a general trend to increase with time. Both solutions also follow a sinusoidal pattern, corresponding to temperature change due to L2's motion around the Sun (Greasen et al. 2012). However, we do find the COSMOGLOBE K -band gain has slightly more oscillatory features than the WMAP9 solution. In general, the gains are consistent between COSMOGLOBE and WMAP9 within 1% . For completeness, the full gain comparisons can be found in Fig. A.5.

4.3. Transmission imbalance

The transmission imbalance parameters x_{im} are crucial to measure correctly because their misestimation can induce a large polarized signal that is coupled to the Solar dipole (Jarosik et al.



Fig. 2. Overview of K113. The red solid lines in first and second panel are the delivered gain and baselines from WMAP9, while the black lines in all panels are samples from the COSMOGLOBE Gibbs chain. The red dashed and yellow dashed lines are reported σ_0 and f_{knee} values from the first-year WMAP data analysis and GSFC measurements, respectively.

2007; Watts et al. 2022). The uncertainty in x_{im} was quoted as the source of large-scale polarized features in the WMAP9 maps, and a template of this effect was explicitly projected out in the pixel-space polarized covariance matrix.

We find x_{im} values that are largely consistent with the values reported in Bennett et al. (2013), albeit with some outliers. We find in general that the 68 % confidence intervals from COSMOGLOBE are smaller than the fiducial values, although we caution against a direct comparison of these values since such different procedures were used for estimating the uncertainties.

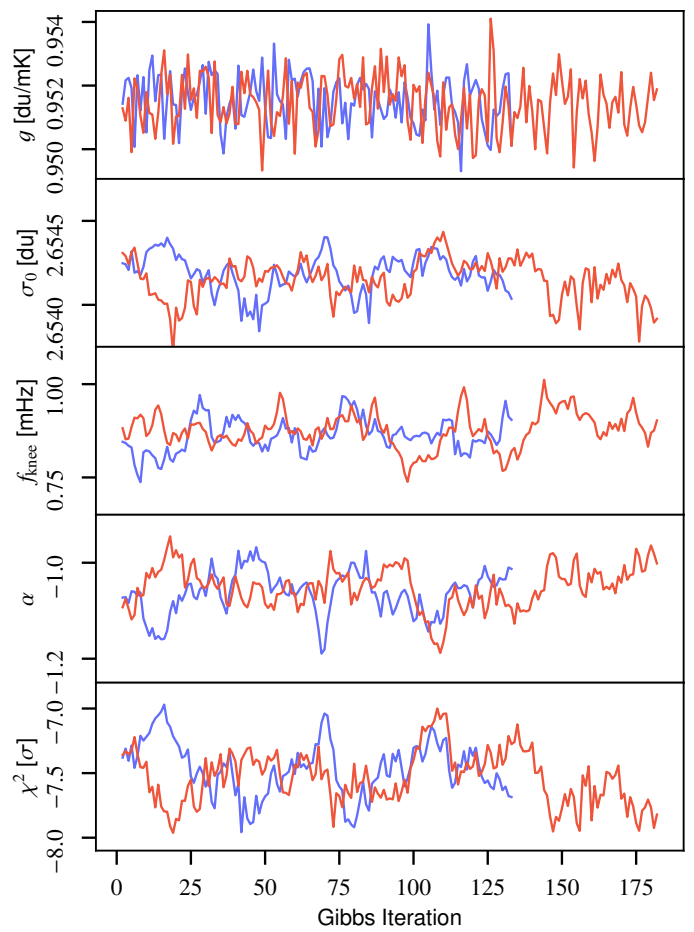


Fig. 3. Subset of K113 Gibbs samples for both chains, arbitrarily colored red and blue. The parameters correspond to MJDs 52285.2–52290.6.

4.4. Instrumental noise and goodness-of-fit

The noise fitting, as outlined in Sect. 2.7, inherently depends on the data being fit well by both the sky model and the instrument model. In practice, correlated noise fitting can model any unmodeled signals, so the power spectrum and TODs must be carefully scrutinized before any conclusions can be made about the corresponding maps.

The white noise level in raw du is not strictly sampled, but is estimated conditioned on the instrumental parameters and the sky parameters. However, the calibrated white noise level $\sigma_0[\text{K}] = \sigma_0[\text{du}]/g$ does depend on the gain quite directly, which allows us to test the effects of the calibration on the instrument sensitivity itself. The calibrated white noise level follows a biaurnal trend indicative of a system temperature variation, which is to be expected given the radiometer equation

$$\sigma_0[\text{V}] \propto gT_{\text{sys}}. \quad (56)$$

Aside from an overall amplitude shift due to the absolute calibration variation, the shape of the white noise level is stable throughout the Gibbs chain.

The knee frequencies for each channel lie between the reported values in Jarosik et al. (2003a) for both the Goddard Space Flight Center (GSFC) laboratory measurements and those from the first year of data collection. Nearly all radiometers have constant f_{knee} throughout the mission, with a few notable exceptions. First, all W-band channels display some amount of tem-



Fig. 4. Noise parameter correlation matrix. We average over all Gibbs samples of the noise parameters $\xi^n = \{\alpha, f_{\text{knee}}, \sigma_0\}$ for each PID. We then find the correlation in time between these averages for the different bands and detector. The results here are for the calibrated white noise level, $\sigma_0 [\text{mK}]$. The values for each detector are ordered 13, 14, 23, and 24

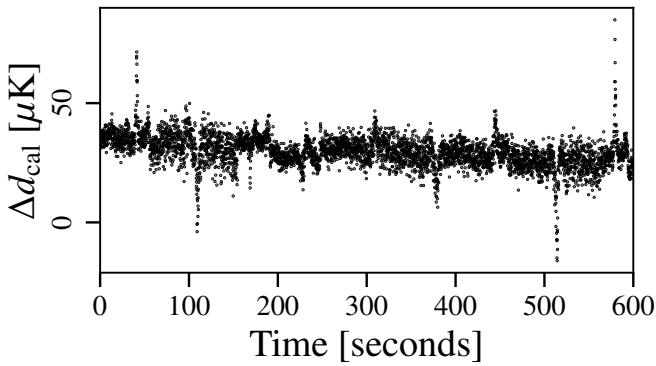


Fig. 5. Difference between the CosMOGLOBE $d_{\text{cal}} = d/g - b - s_{\text{sl}}$ and the delivered calibrated TOD from WMAP. **Zoom in, maybe 0–100 seconds or less**

poral variation that does not seem to be associated with any sinusoidal features. Second, all $Q2$ channels, $V223$, and $V224$ all display a similar asymptotic drift in time. We have not found any instrumental effects that share this feature. The PSD slope α is around -1 for each radiometer, albeit with high scatter for the lower frequencies. As expected, the uncertainty in α decreases as f_{knee} increases, since there are more datapoints to fit below f_{knee} where the constraining power on α is the strongest.

The most striking feature of the reduced normalized χ^2 is its amplitude and its semiannual periodicity. Given the noise model and data residual, we can evaluate the goodness-of-fit in the form of the relative χ^2 . Here, we find that approximately half of the radiometers have a χ^2 value at least 6σ above or below the expected value. Given perfect Gaussian residuals, we would expect the reduced sum of squares to be $n_{\text{tod}} = 2^N$ and be within $\sqrt{2n_{\text{tod}}} = 2^{(N+1)/2}$ 68 % of the time. For a typical W -band scan of length $n_{\text{TOD}} = 2^{22}$, a 10σ model failure corresponds to

Table 3. Summary of noise properties.

Radiometer ..	Diode	Sensitivity, σ_0 (mK \sqrt{s})			Knee frequency, f_{knee} (mHz)			Slope, α
		GSFC	WMAP	CG/ $\sqrt{2}$	GSFC	WMAP	CG/ $\sqrt{2}$	
K11	1	0.72	0.66	0.704 ± 0.002	6.13	0.4	0.82 ± 0.20	-1.01 ± 0.10
	2			0.708 ± 0.003			0.63 ± 0.14	-0.95 ± 0.10
K12	1	0.87	0.75	0.796 ± 0.004	5.37	0.51	0.42 ± 0.19	-0.93 ± 0.12
	2			0.780 ± 0.005			0.71 ± 0.15	-1.02 ± 0.10
Ka11	1	0.75	0.71	0.788 ± 0.001	1.66	0.71	1.20 ± 0.22	-1.02 ± 0.09
	2			0.777 ± 0.001			1.19 ± 0.22	-1.02 ± 0.09
Ka12	1	0.77	0.72	0.788 ± 0.003	1.29	0.32	0.62 ± 0.16	-0.99 ± 0.11
	2			0.784 ± 0.001			0.63 ± 0.13	-1.01 ± 0.11
Q11	1	0.99	0.92	0.998 ± 0.002	3.21	1.09	1.06 ± 0.16	-1.09 ± 0.09
	2			0.992 ± 0.002			1.06 ± 0.16	-1.10 ± 0.09
Q12	1	0.95	1.02	1.159 ± 0.007	3.13	0.35	0.45 ± 0.47	-0.98 ± 0.11
	2			1.146 ± 0.007			0.83 ± 0.14	-1.00 ± 0.09
Q21	1	0.89	0.85	0.908 ± 0.002	1.92	5.76	2.88 ± 0.37	-1.10 ± 0.07
	2			0.906 ± 0.002			3.22 ± 0.56	-1.10 ± 0.06
Q22	1	1.04	0.99	1.074 ± 0.004	4.61	8.62	3.95 ± 0.54	-1.11 ± 0.06
	2			1.064 ± 0.003			4.05 ± 0.64	-1.11 ± 0.06
V11	1	1.25	1.22	1.551 ± 0.003	2.56	0.09	1.27 ± 0.15	-0.90 ± 0.06
	2			1.539 ± 0.003			1.19 ± 0.14	-0.89 ± 0.06
V12	1	1.07	1.11	1.398 ± 0.002	4.49	1.41	2.11 ± 0.20	-0.97 ± 0.05
	2			1.432 ± 0.002			1.88 ± 0.17	-0.96 ± 0.05
V21	1	1.01	0.97	1.241 ± 0.298	2.43	0.88	1.50 ± 0.24	-0.95 ± 0.07
	2			1.217 ± 0.294			1.60 ± 0.26	-0.97 ± 0.06
V22	1	1.13	1.1	1.443 ± 0.300	3.06	8.35	4.01 ± 0.85	-1.00 ± 0.08
	2			1.415 ± 0.316			3.08 ± 0.65	-1.01 ± 0.08
W11	1	1.18	1.35	1.938 ± 0.005	16.2	7.88	5.59 ± 0.53	-0.94 ± 0.05
	2			1.895 ± 0.005			8.99 ± 0.85	-0.95 ± 0.04
W12	1	1.41	1.61	2.301 ± 0.005	15.1	0.66	3.91 ± 0.42	-0.89 ± 0.05
	2			2.345 ± 0.006			4.81 ± 0.53	-0.89 ± 0.05
W21	1	1.38	1.61	2.225 ± 0.007	1.76	9.02	13.57 ± 1.47	-0.89 ± 0.03
	2			2.292 ± 0.006			5.06 ± 0.95	-0.93 ± 0.05
W22	1	1.44	1.72	2.291 ± 0.006	0.77	7.47	3.02 ± 0.53	-0.98 ± 0.05
	2			2.232 ± 0.007			7.26 ± 1.05	-0.95 ± 0.04
W31	1	1.47	1.65	2.328 ± 0.005	1.84	0.93	1.30 ± 0.46	-0.99 ± 0.07
	2			2.322 ± 0.006			1.97 ± 0.28	-0.98 ± 0.06
W32	1	1.69	1.86	2.707 ± 0.015	2.39	0.28	1.59 ± 0.29	-0.98 ± 0.07
	2			2.579 ± 0.015			1.40 ± 0.39	-1.00 ± 0.07
W41	1	1.6	1.71	2.519 ± 0.010	8.46	46.5	26.81 ± 1.83	-0.92 ± 0.04
	2			2.479 ± 0.009			24.75 ± 1.63	-0.92 ± 0.04
W42	1	1.43	1.65	2.221 ± 0.017	5.31	26.0	16.10 ± 1.09	-0.94 ± 0.04
	2			2.202 ± 0.015			17.11 ± 1.19	-0.94 ± 0.04

$\chi^2/n_{\text{TOD}} = 1.003$. Therefore, it is exceedingly difficult to look at any given WMAP scan in the time domain and identify a model failure. In power spectrum space, i.e., in Fig. 7, the data are still characterized well at all scales, despite this scan having a χ^2 that is 7σ above the expectation value.

Only with aggressive smoothing, as in Fig. 8, does the model failure become apparent at frequencies 1–10 Hz. Here, it is clear that despite fitting the data well at the highest and lowest frequencies, it is in the intermediate range of 1–5 Hz where the $1/f$ model is a less accurate fit to the residual power spectrum. Part of the cause of this failure is that the white noise level is essentially fixed by the value of the power spectrum at the Nyquist frequency, as it was computed by differencing adjacent samples. The power spectrum has a downward trend beyond above 1 Hz, indicating that the data would be better fit by one or more terms proportional to f^α . This is phenomenologically similar to the WMAP collaboration's approach of describing the time-space autocorrelation as a cubic polynomial in $\log \Delta t$ (Jarosik et al. 2007).

In practice, the $1/f$ model has a small effect on the final data products, and was not visible in noise models when we modeled the data in one day scans rather than the longer 3–7 day scans due to the lower n_{TOD} giving a higher uncertainty on the relative χ^2 . Therefore, although this strictly constitutes a deficiency in the model, it is in practice too small to affect the results of the rest of the chain. The downturn of the noise PSD at high frequencies is also present in, e.g., the Planck HFI data (Planck Collaboration Int. XLVI 2016, Fig. 1), so improved modeling of this form will be a necessity in future COSMOGLOBE endeavors, and will be used to improve the WMAP data processing.

5. Frequency maps

In this section, we present the reprocessed WMAP frequency maps and their properties. In Sect 5.1 we present the reprocessed WMAP maps themselves, commenting on notable features. Section 5.2 compares the properties of the individual DAs with the published WMAP9 results, while Sect. 5.3 focuses on the internal

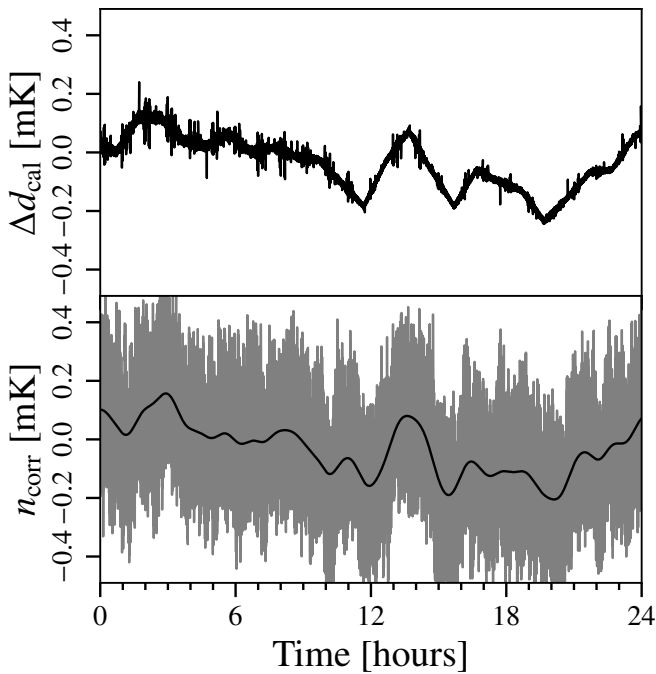


Fig. 6. (top): Difference between the COSMOGLOBE $d_{\text{cal}} = d/g - \mathbf{b} - \mathbf{s}_{\text{sl}}$ and the delivered calibrated TOD from *WMAP*. (Bottom): Raw correlated noise (gray) and smoothed data with Gaussian kernel (black). This shows more clearly the hourly baseline subtraction from the *WMAP* treatment.

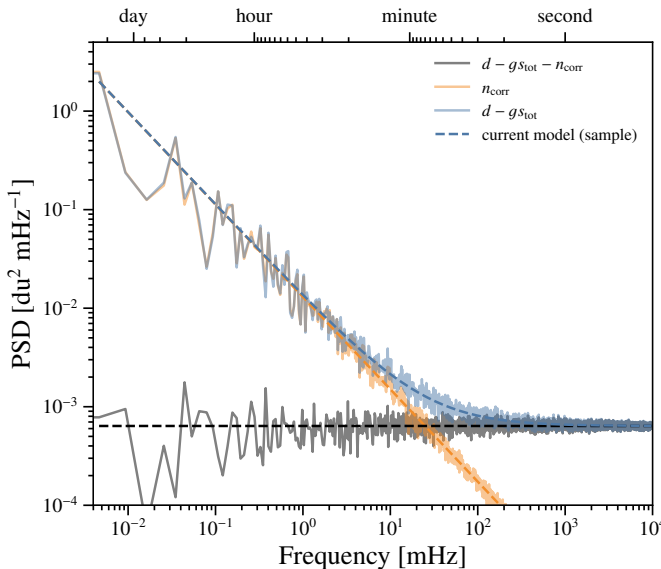


Fig. 7. PSD for radiometer W413 that spans MJDs 52252.3–52254.8. The power spectrum of the blue line corresponds to the residual, while the gray line is the residual with a correlated noise realization removed.

consistency between the *WMAP* channels themselves. Finally, we assess the consistency between the LFI channels and *WMAP* in Sect. 5.4 and compare with legacy results.

5.1. Map summary statistics

For each DA, we present the mean maps, the white noise contribution in the form of RMS maps, and the standard deviation of the maps accounting for the sampling of instrumental parame-

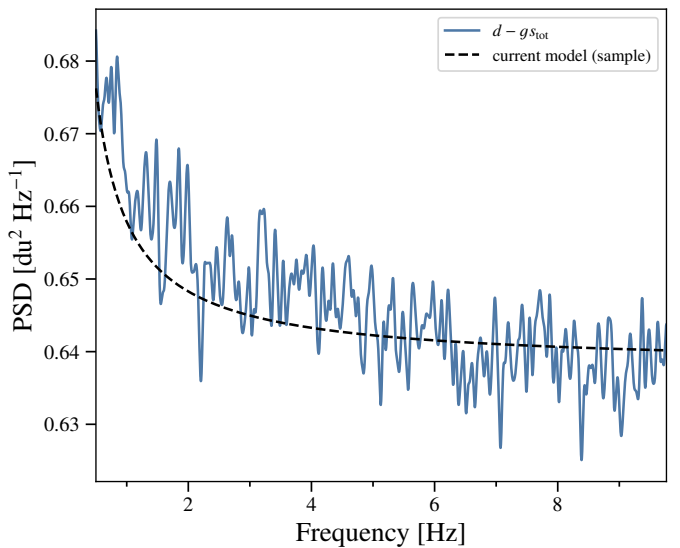


Fig. 8. PSD for radiometer W413 that spans MJDs 52252.3–52254.8. The black dashed line is a sample of the theoretical PSD, while the blue line is the smoothed residual power spectrum.

ters. Each mean map retains the Solar dipole, which we will estimate separately in Sect. 6.1.1. Additionally, we present inverse-weighted mean maps of Q , V , and W rather than displaying each individual DA.

The K -band, Ka -band, Q -band, V -band, and W -band mean maps are presented in Figs. 9, 10, 11, 12, and 13, respectively, given in μK_{CMB} units. The temperature maps are presented at full resolution, while the polarization maps have been smoothed with a 2° Gaussian beam. The maps in temperature behave as expected, with consistent Solar dipole and Galactic foreground emission decreasing as the frequency increases. Similarly, the polarized maps decrease from K – V -band following the expected synchrotron behavior, with a slight increase at W -band due to the contribution of thermal dust. Most striking, especially when compared with the delivered *WMAP9* maps, is the lack of transmission imbalance modes or poorly measured modes in the polarized maps.

The RMS maps are computed during the mapmaking routine, adding $\sigma_{0,i}^{-2}$ for every timestep that horn is in a given pixel, appropriately scaled by polarization angle and imbalance parameters. The top row of Fig. 14 shows the white noise for the Stokes parameters and the correlation coefficient between Stokes Q and U . The white noise pattern for T follows the usual pattern with highest sensitivity at the North and South ecliptic poles, as well as circles around the poles corresponding to times when the partner horn is observing the opposite ecliptic pole. There are also regions of higher noise level corresponding to planets crossing the ecliptic, and regions of higher emission $\simeq 140^\circ$ away from the Galactic center, which correspond to the times when the partner horn lies within the processing mask.

The polarized RMS maps share all of these characteristics, but with an overall amplitude shift due to polarization measurements having half the effective number of observations per pixel. In addition, the poles have a characteristic “X”-like structure that is rotated 45° degrees between Q and U , corresponding to different polarization orientations. There are also characteristic large scale structures visible in Galactic coordinates, corresponding to polarization modes poorly constrained by the *WMAP* scan strategy.

While the maps in the top row of Fig. 14 are directly comparable to the *WMAP9* products, the bottom row shows a unique product, the standard deviation and *QU* correlation of the output chain maps. These maps can be considered the “systematic” error contributions, as their variation depends on the sampled instrumental parameters, i.e., gain, imbalance parameters, correlated noise, and sidelobe correction. The temperature map contains a clear quadrupole signature. This is due to the variation in the absolute calibration g_0 , which changes the Solar dipole in the final map. In addition to the quadrupole, the Galactic plane also varies due to the gain solution being varied. As expected, the white noise patterns associated with the scan strategy also appear in the polarization maps, and become more clear in the temperature maps for the higher frequency DAs (Fig. B.3). As these maps only include 490 total samples out of full 500-sample Gibbs chain, they will be superseded by a larger future chain. While the quantitative solution will change, it is unlikely that the final maps will differ qualitatively from those presented here.

An additional useful term to consider is the difference between two arbitrary samples, which we show in Fig. 15. In temperature, the most clear term is a dipole corresponding to the absolute gain difference and the Galactic plane. There are also additional small lines associated with the scanning strategy, which correspond to different correlated noise realizations. In polarization, correlated noise is the dominant difference between two samples, with a small imprint of the Galactic plane due to relative gain variation. The polarization differences are aligned with *WMAP*’s scans, modulated by the polarization angle.

We also consider the spatial structure of the TOD corrections in pixel space, as shown in Fig. 16. This corresponds to the TOD objects in Fig. 1 binned into Stokes *I*, *Q*, and *U* maps. Note that the dynamic range of each of these figures varies by two orders of magnitude, indicating that some components must be subtracted more carefully than others. However, the amplitude of the signal is not proportional to the level of scrutiny necessary, as some, such as orbital dipole, are much more precisely known than the others.

The variation of these TOD corrections is more important than the absolute amplitude. As shown in Fig. 17, white noise is the dominant effect for $\ell \gtrsim 100$ for all frequencies. For temperature, the low-multipole variation in the orbital dipole signal and far sidelobe corrections are the largest source of fluctuations and low multipoles, but remain orders of magnitude below the average signal. These fluctuations are directly related to absolute calibration uncertainty, and provide a practical limit to the magnitude gain effects the temperature signal. For the C_ℓ^{EE} and C_ℓ^{BB} spectra, the relative amplitude of the fluctuations are band-dependent. For example, bandpass leakage and orbital dipole corrections are the dominant effect, while for *Q*-band, the correlated noise realizations contribute the most variation. In general, we find that for large angular scale polarization, modelling uncertainties in the form of gain and sidelobe estimation have a comparable effect to white noise and correlated noise estimates.

As a final inspection of the COSMOGLOBE map products, we take the angular power spectra of the maps themselves and compare with the *WMAP9* results in Figs. 18–21. To compute the power spectrum, we mask the data using the extended temperature analysis mask which allows a sky fraction of 68.8 % and obtain the pseudo- C_ℓ power spectra using the NaMaster (Alonso et al. 2019)⁷ `compute_full_master` routine, returning a set of decoupled bandpowers.

As the temperature power spectra are signal-dominated up to $\ell \sim 200$ for all DAs, it is more useful to look at the ratio of spectra in Fig. 19. Here we see that the spectra are consistent with each other at all but the very largest and smallest scales. The largest scale differences are due to mode-coupling effects – the *WMAP9* maps were produced by removing the Solar dipole in the timestream before mapmaking, while the COSMOGLOBE maps needed a dipole estimate to be removed as a post-processing step. The small scale differences above $\ell \sim 200$ can be attributed to the white noise treatment. In particular, the *WMAP9* processing gain solution varies every 23 s compared to the COSMOGLOBE solution which uses constant gain per scan. Conversely, the COSMOGLOBE radiometer noise estimate varies per scan, whereas there is no mention of raw instrumental noise variation with time in the *WMAP* suite of papers.

The *E*-mode power spectra, displayed in Fig. 20, is mainly dominated by noise and polarized synchrotron emission. As expected, the large scale foreground-dominated multipoles decrease in amplitude according to the relative amplitude of the synchrotron spectrum. Aside from the $\ell = 8$ *W2* multipole, the COSMOGLOBE power spectra are well-behaved across all bands. The large fluctuations in the *WMAP* power spectrum, in particular *W2* and *W4*, are almost completely gone in the COSMOGLOBE analysis.

The *B*-mode power spectra, displayed in Fig. 21, should follow the same pattern as in the *E*-modes, but with foregrounds reduced by a factor of $\simeq 2$ (Bennett et al. 2013). Indeed, with the notable exception of the *Ka* and *Q1* $\ell = 3$ multipoles and the *W3* $\ell = 7$ multipole, this pattern is largely borne out, with nearly white noise across all angular scales. The $C_{\ell=3}^{\text{BB}}$ mode has been identified as being poorly measured by, e.g., Jarosik et al. (2011), due to its symmetry aligning with $\gtrsim 10$ min signals in the TOD induced by the *WMAP* scan strategy.

In general, we find that the reprocessed *WMAP* maps produced in the COSMOGLOBE framework have map and power spectrum properties that have few artifacts of the observation strategy. To fully assess the quality of these frequency maps compared to the official *WMAP9* products, we compare the maps explicitly in Sect. 5.2.

5.2. Comparison with 9-year WMAP maps

We present difference maps between the official 9-year *WMAP* maps and the maps produced in this work in Fig. 23. This figure shows a total of fifteen difference maps, one for each of the main *WMAP* bands (*K*, *Ka*, *Q*, *V*, and *W*), in the three Stokes’ parameters.

The differences are overall quite small, as the *WMAP* processing is nearly identical, with subtle differences as described in Sec. 3. Starting with total intensity, we see good agreement with the full *WMAP9* results, with deviations at the few μK level. The largest difference between the two analyses is shown in the *K*-band difference map, which demonstrates the difference between the band calibration as described in Secs. 4.2 and 8.3. For the other bands, we see some other differences which Duncan can elaborate on here.

In polarization, we note large scale differences in both Stokes *Q* and *U*. These large scale differences do not match known Galactic component morphologies. Across the *WMAP* bands, many of these differences are reminiscent of the poorly measured mode templates provided by the original *WMAP* team (Fig. A.10), though the map-space morphologies are not identical. These large mode differences have been tracked down to be a result of the interplay between the horn imbalance parameters

⁷ <https://github.com/LSSTDESC/NaMaster>



Fig. 9. K -band

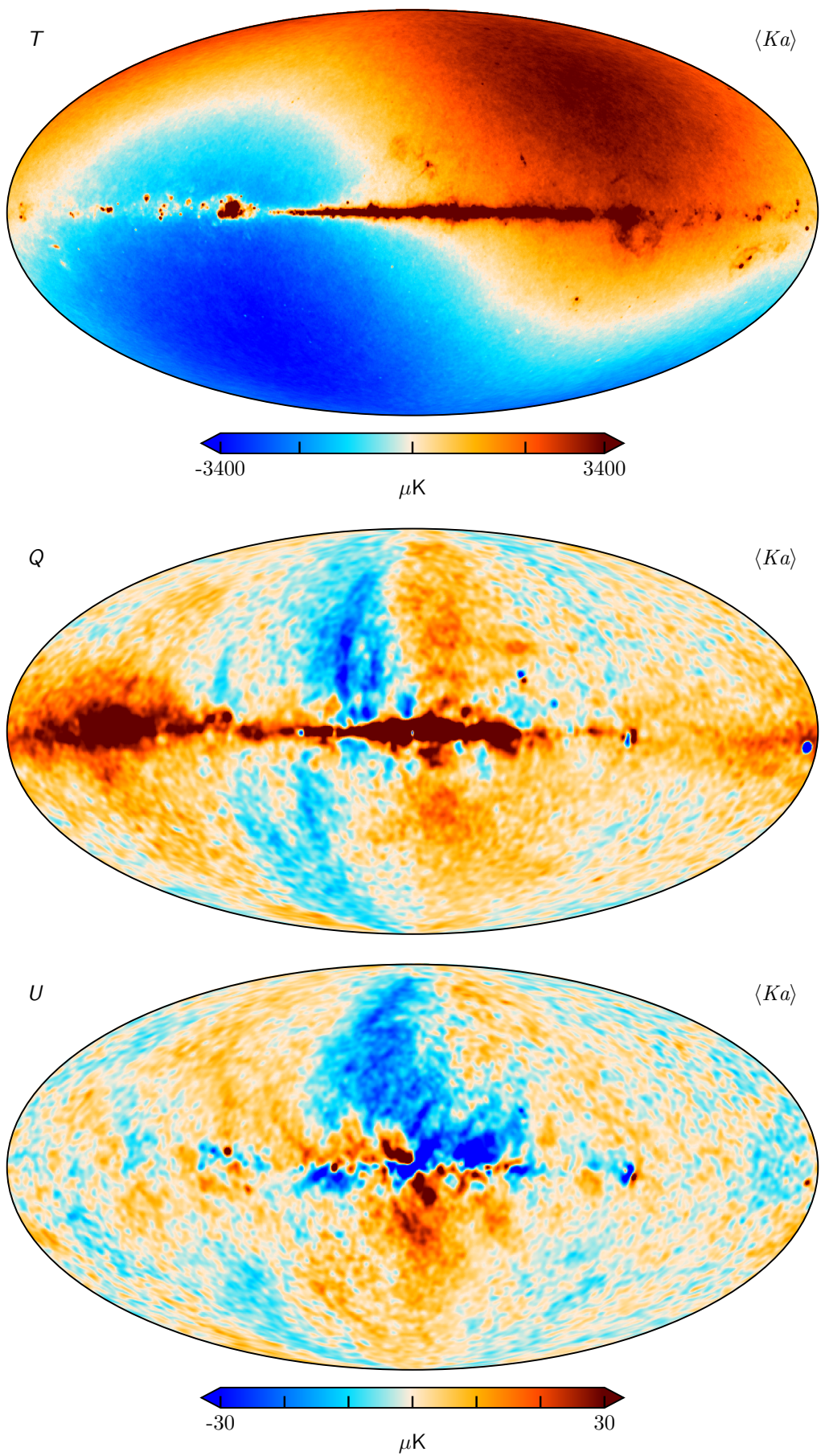


Fig. 10. Ka -band

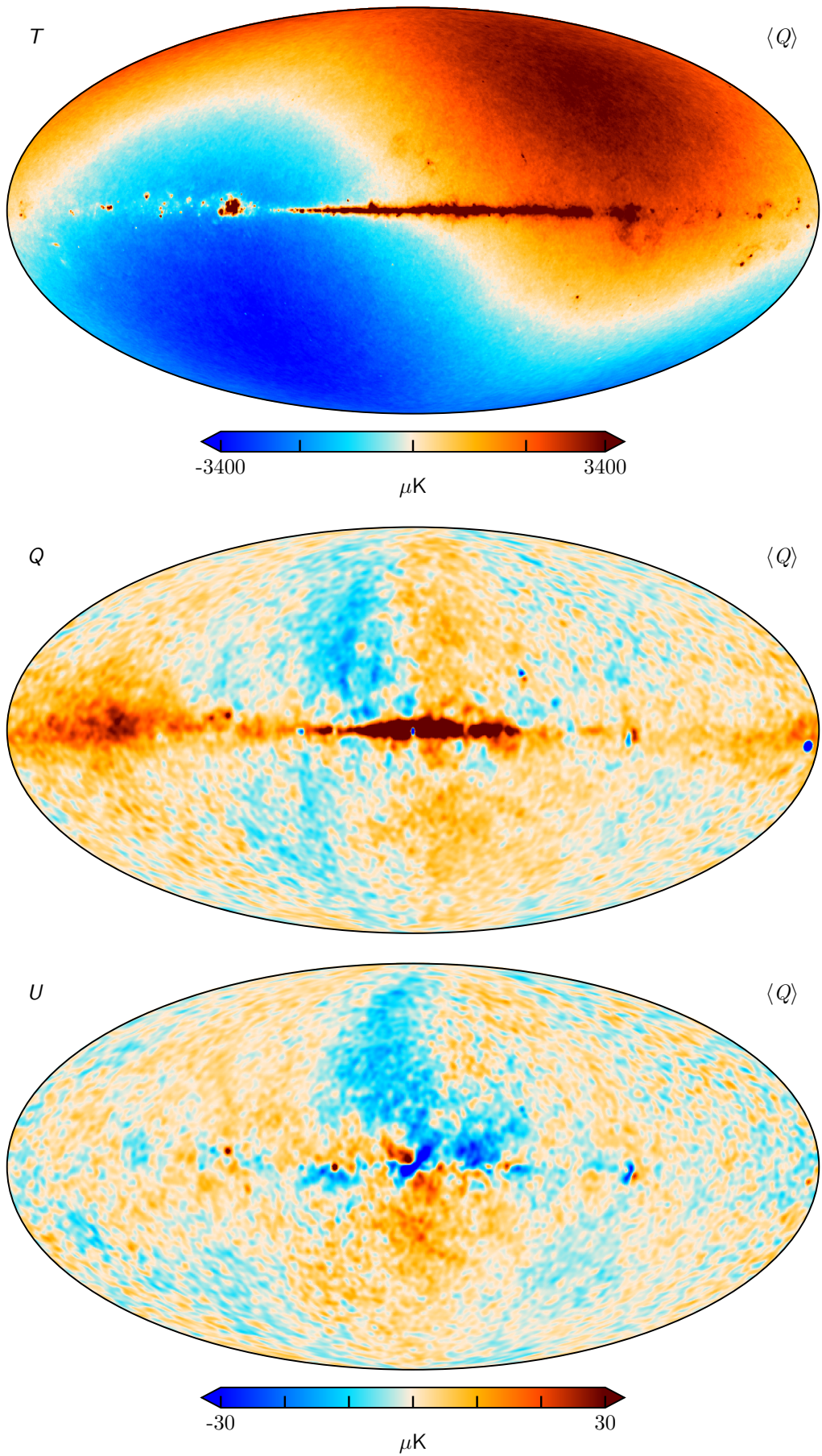


Fig. 11. Q -band

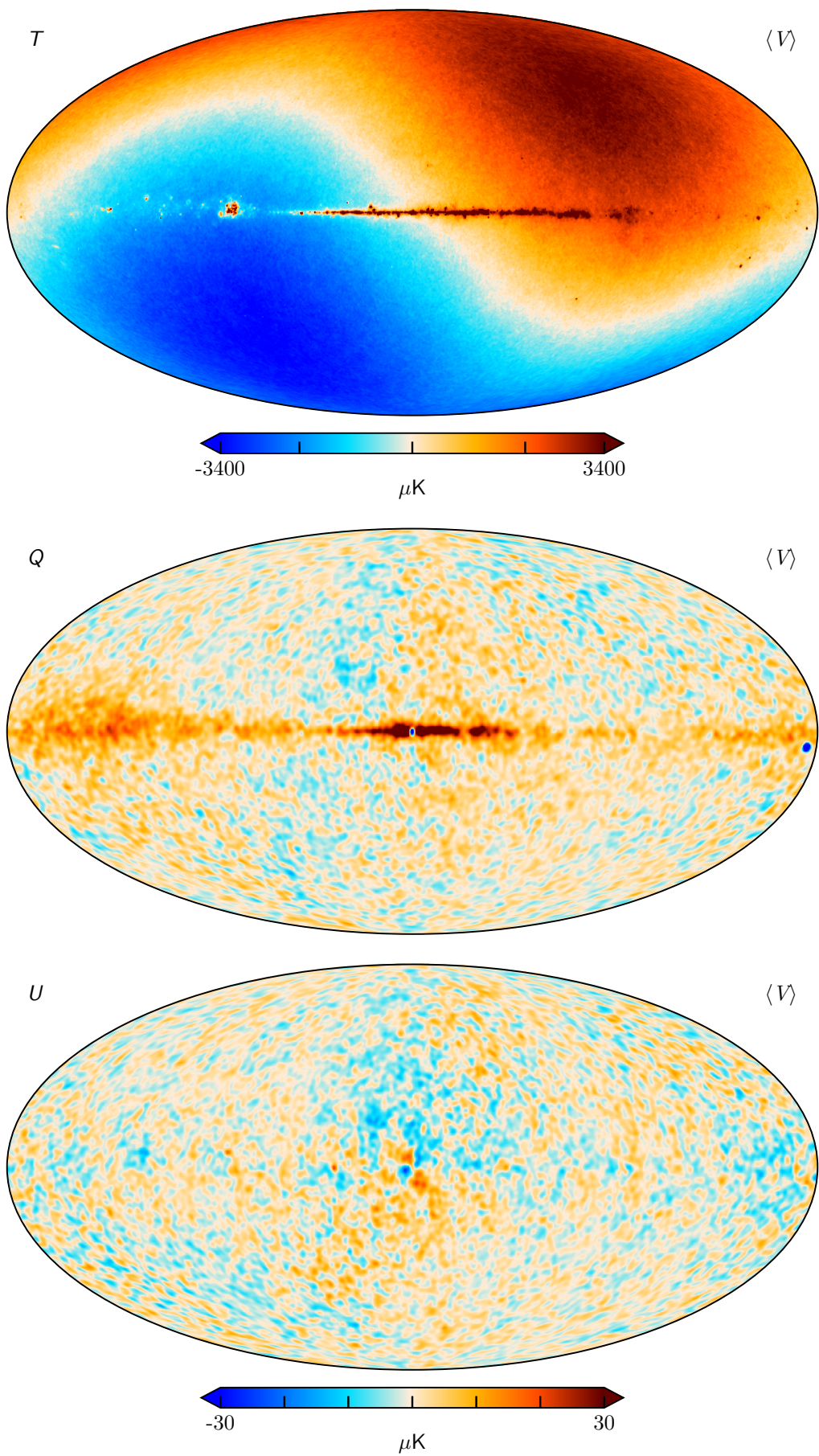


Fig. 12. *V*-band

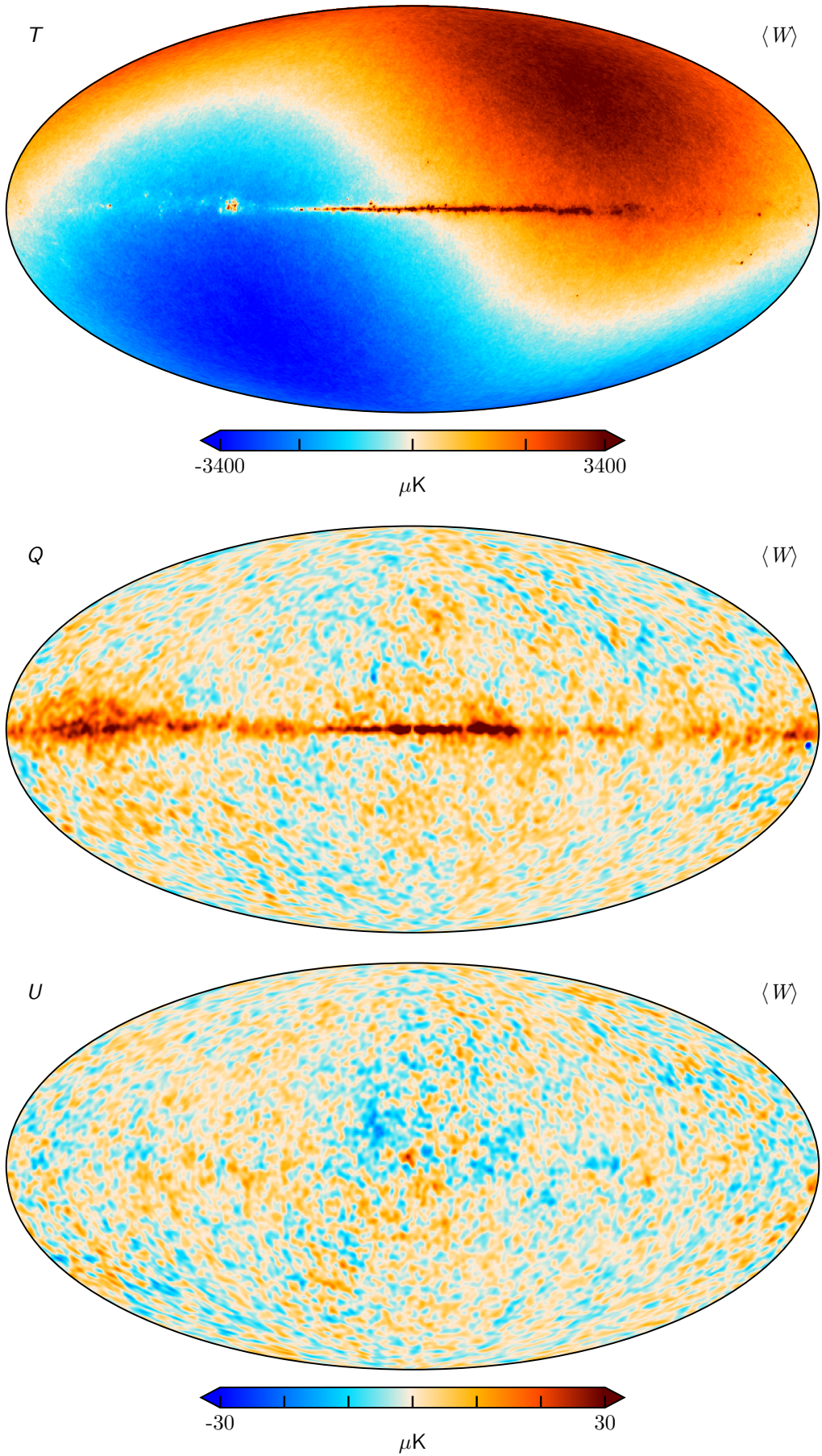


Fig. 13. W-band

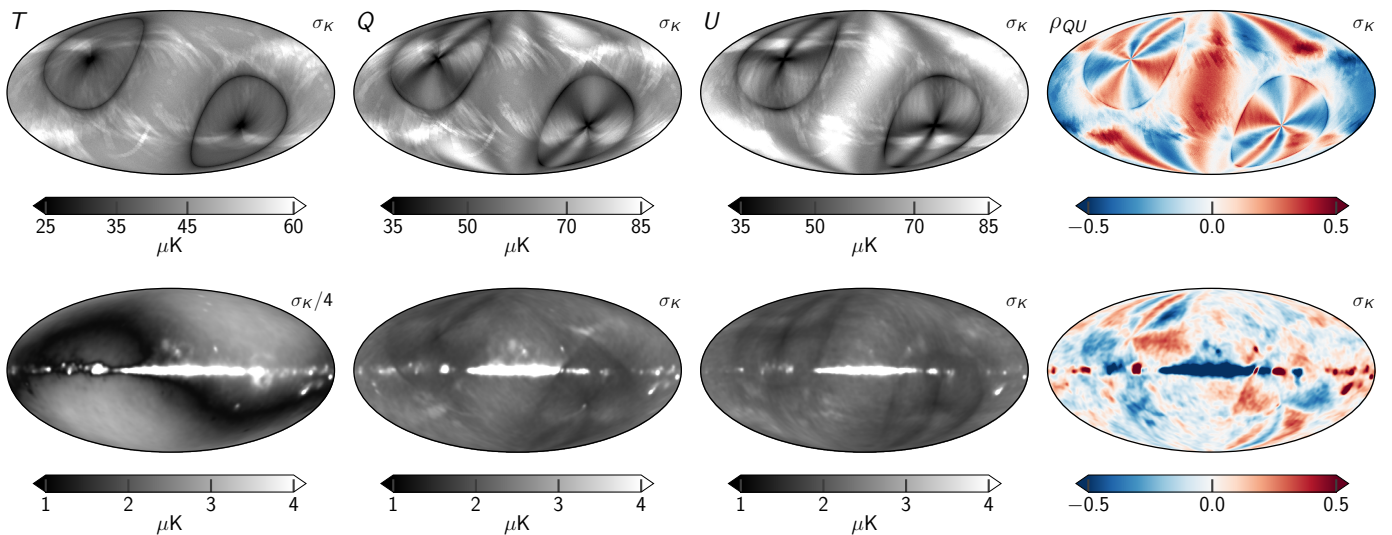


Fig. 14. Posterior variation maps for K -band. Columns show the Stokes parameters and the correlation coefficient between Q and U , while the rows show (top) the white noise rms per pixel and (bottom) the posterior standard deviation. The rms maps are unsmoothed, while the standard deviations have been smoothed to 7° .

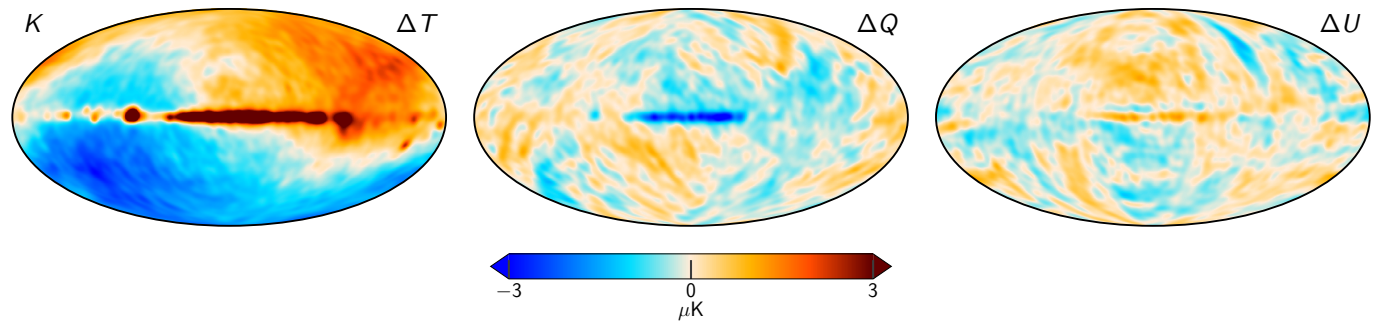


Fig. 15. Difference between two K -band Gibbs samples, smoothed to 7° .

x_{im} , the far sidelobe, and the Solar dipole, as briefly described in Sec. 2.2. The scale of this effect is most pronounced in the W -band polarization results, where we see the largest differences between the two processing pipelines.

This truly demonstrates the benefit of jointly processing these two experiments simultaneously in the same framework. The differences shown in Fig. 23, particularly in polarization, are due to unmodeled systematics in the 9-year *WMAP* maps. If these large scale modes, which are not Galactic in origin, were in the maps produced in this work, these modes would either be clearly present in Galactic component maps, or in the component separation residuals (Sec. 6, Fig. B.6) and they are present in neither.

Comment on the differences – the kinematic quadrupole is not removed in the *WMAP9* maps (Larson et al. 2015), and the amplitude goes as $\nu/(2T_0) \coth(\nu/(2T_0))$ (Notari & Quartin 2015).

5.3. Consistency within WMAP channels

An important test for how well the instrumental systematics are being modeled is by checking the agreement within each of the *WMAP* channels. As described in Sec. 2.2, the Q -, V -bands each had two DAs, and the W -band had four. Checking for discrepancies between each of the individual DA maps within the same frequency channel can highlight mismodeled systematics.

Table 4. Difference map χ^2 statistics.

DIFFERENCE	χ^2_{uncorr}	χ^2_{corr}	$\Delta\chi^2$
$0.32 \times K1 - K1 \dots$	4291	4287	4
$Q1 - Q2 \dots \dots$	4500	4380	120
$V1 - V2 \dots \dots$	4490	4429	61
$W1 - W2 \dots \dots$	4328	4270	68
$W3 - W4 \dots \dots$	4257	4145	112

The difference maps between the Q -, V -, and W -band inter-channel maps for Stokes T , Q , and U are shown in Fig.(TBD). The most notable difference has to do with the Galactic plane, which should not be surprising as each DA within each frequency channel as a slightly different bandpass. Beyond this, we see a bunch of things that we can comment on when the figures are actually present.

Looks like, according to this tex document, that there will also be a paragraph or two about the half-difference maps and their spectra.

5.4. Consistency between WMAP and LFI

Seeing as *WMAP* and *LFI* cover nearly identical frequency channels, it is vital to assess how well these two experiments agree

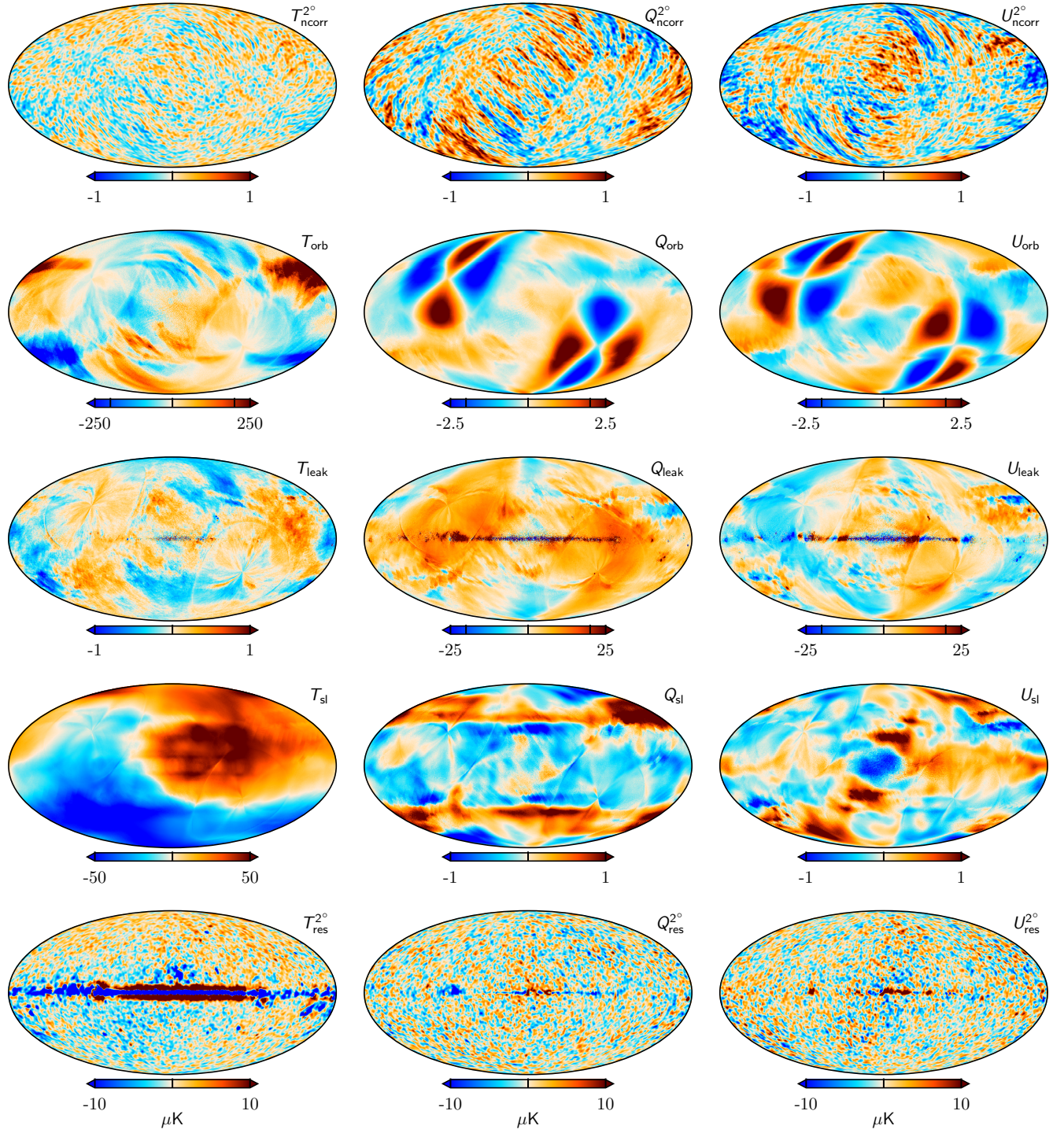


Fig. 16. TOD corrections for K -band for a single Gibbs sample, projected into maps. Columns show Stokes T , Q , and U parameters. Rows show, from top to bottom, 1) correlated noise; 2) the orbital dipole; 3) bandpass mismatch leakage; and 4) sidelobe corrections. The bottom row shows the residual obtained when binning the sky and systematics-subtracted TOD into a sky map. Note that the correlated noise and residual have been smoothed by a 2° Gaussian beam.

with each other, as the sky they observe is the same. Inspecting comparisons of the two experiments' sky maps can help elucidate systematic differences between them. Figure 26 shows comparisons between the *WMAP* K - and Ka -bands and the LFI 30 GHz channel, between the *WMAP* Q -band and LFI 44 GHz, and finally between *WMAP* V -band and LFI 70 GHz. For demonstration, the sky maps produced in this work are compared against the official *WMAP9* and *BeyondPlanck* maps.

Starting with the *Cosmoglobe* maps, we see in the first and third columns of Fig. 26 that the magnitude of the differences are small in both Stokes Q and U . Overall, across all four frequency map comparisons we see small levels of variation, with structure contained to the Galactic plane. Notably, however, is a larger sky signal within the Ka -band – 30 GHz Stokes Q comparison. **This will be commented on here by Duncan or HK as I don't know exactly what I should say.** Deviations at high Galactic latitudes are

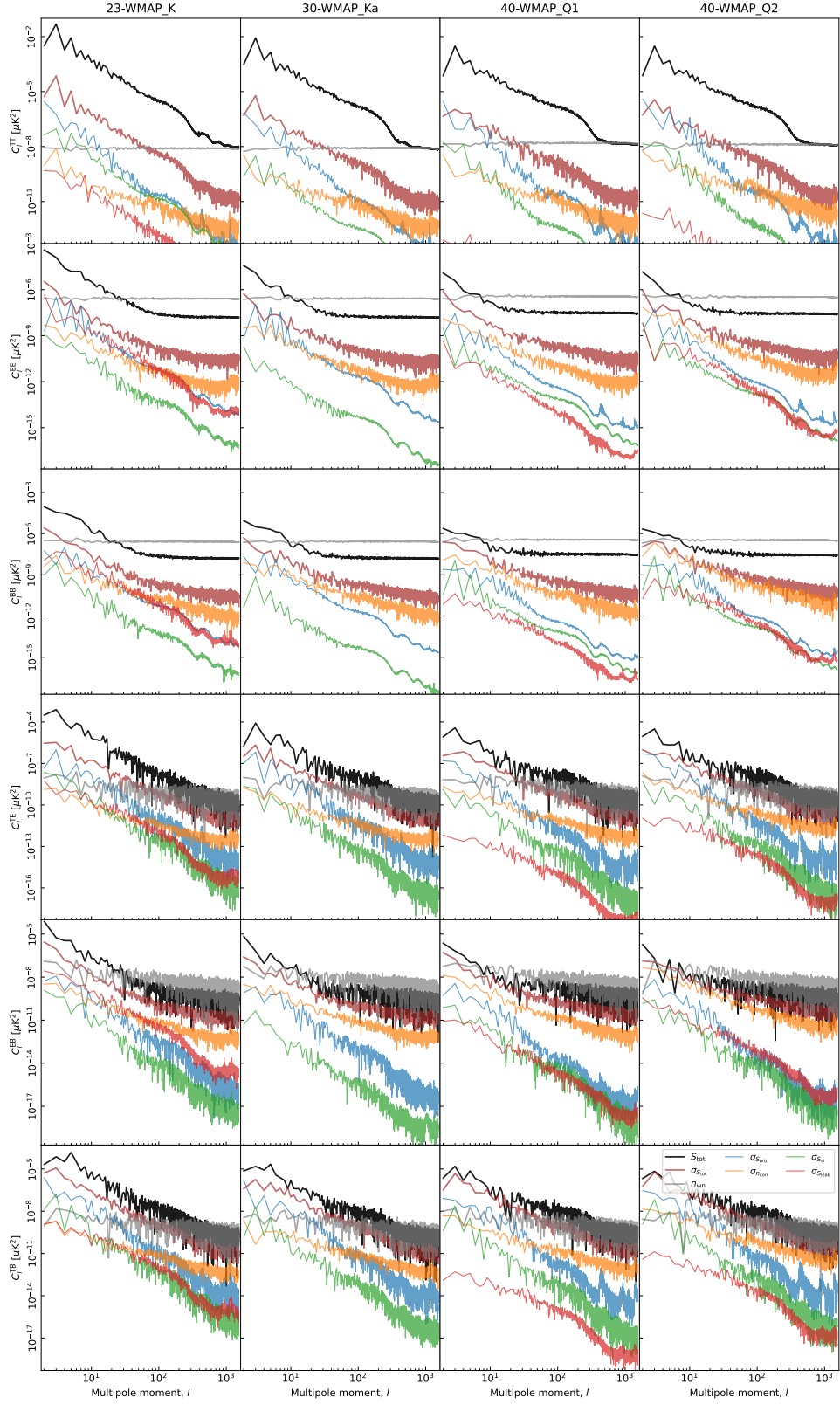
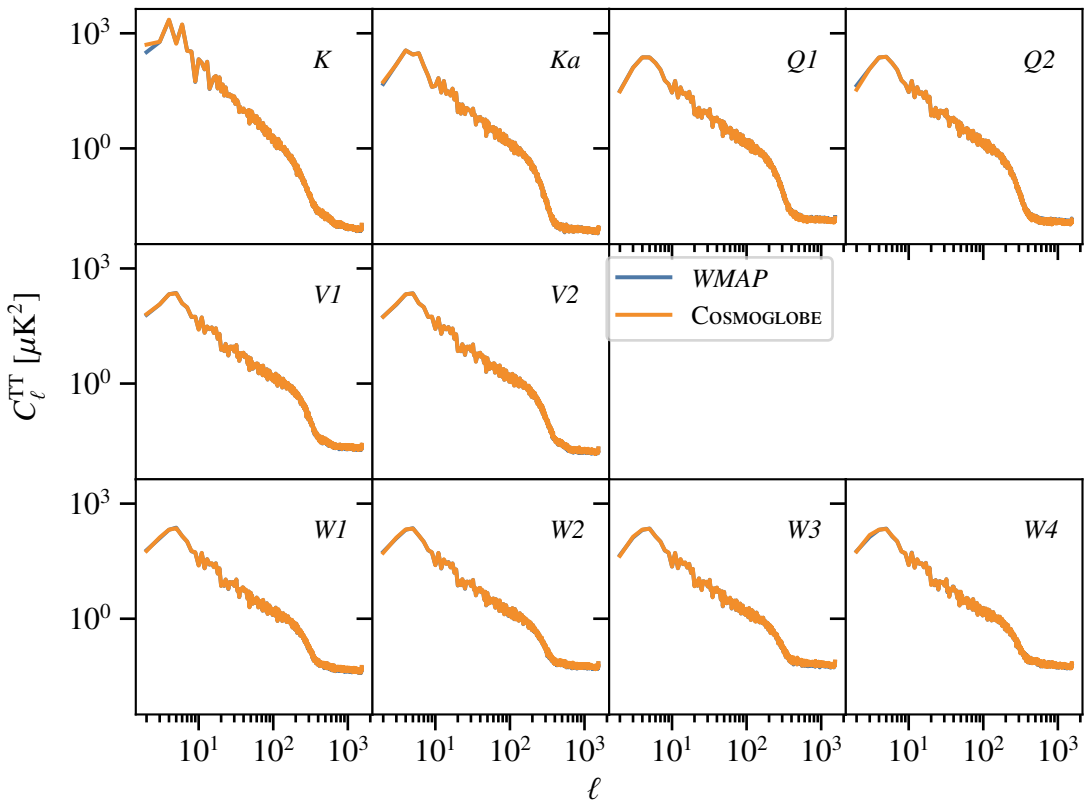
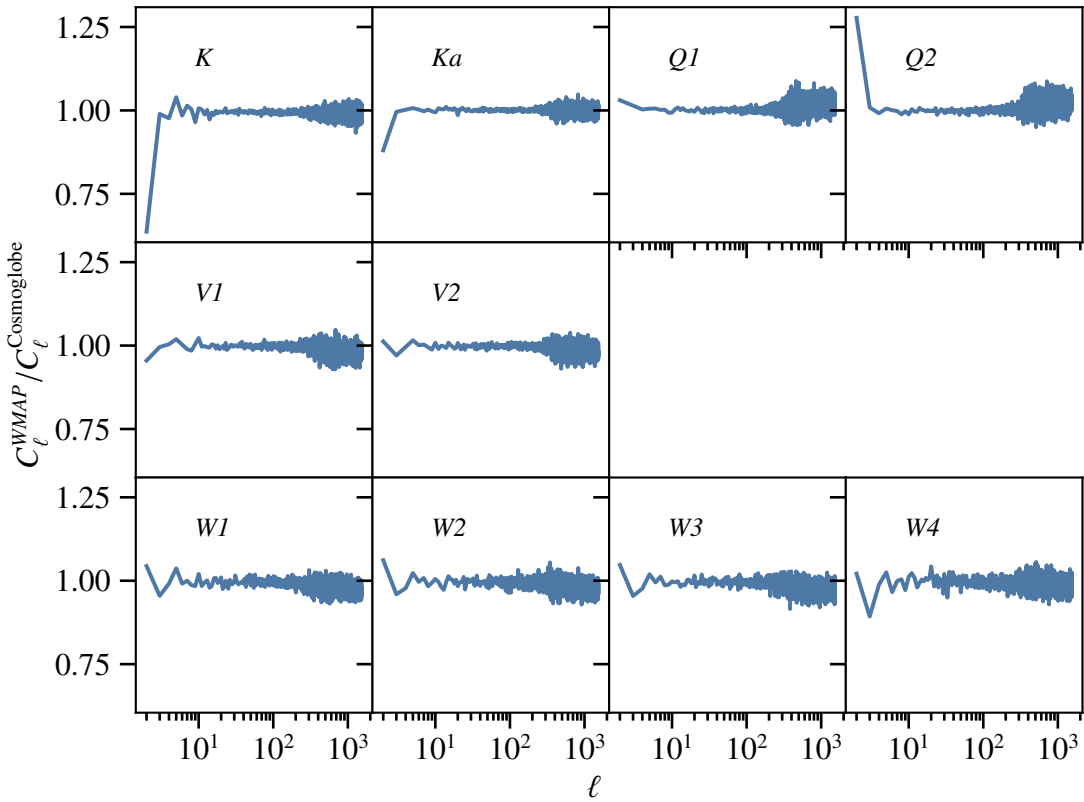


Fig. 17. Pseudo-spectrum standard deviation for each instrumental systematic correction shown in Fig. 16 (thin colored lines). For comparison, thick black lines show spectra for the full coadded frequency map; thick red lines show the standard deviation of the same (i.e., the full systematic uncertainty); gray lines show white noise realizations; and black lines show the power spectra of the mas themselves. Columns show results for K , Ka , $Q1$, and $Q2$, respectively, while rows show results for each of the six polarization states (TT , EE , BB , TE , TB , and EB). All spectra have been derived outside the CMB confidence mask presented by Andersen et al. (2022) using the HEALPix anafast utility, correcting only for sky fraction and not for mask mode coupling.

**Fig. 18.** TT power spectra**Fig. 19.** TT ratios

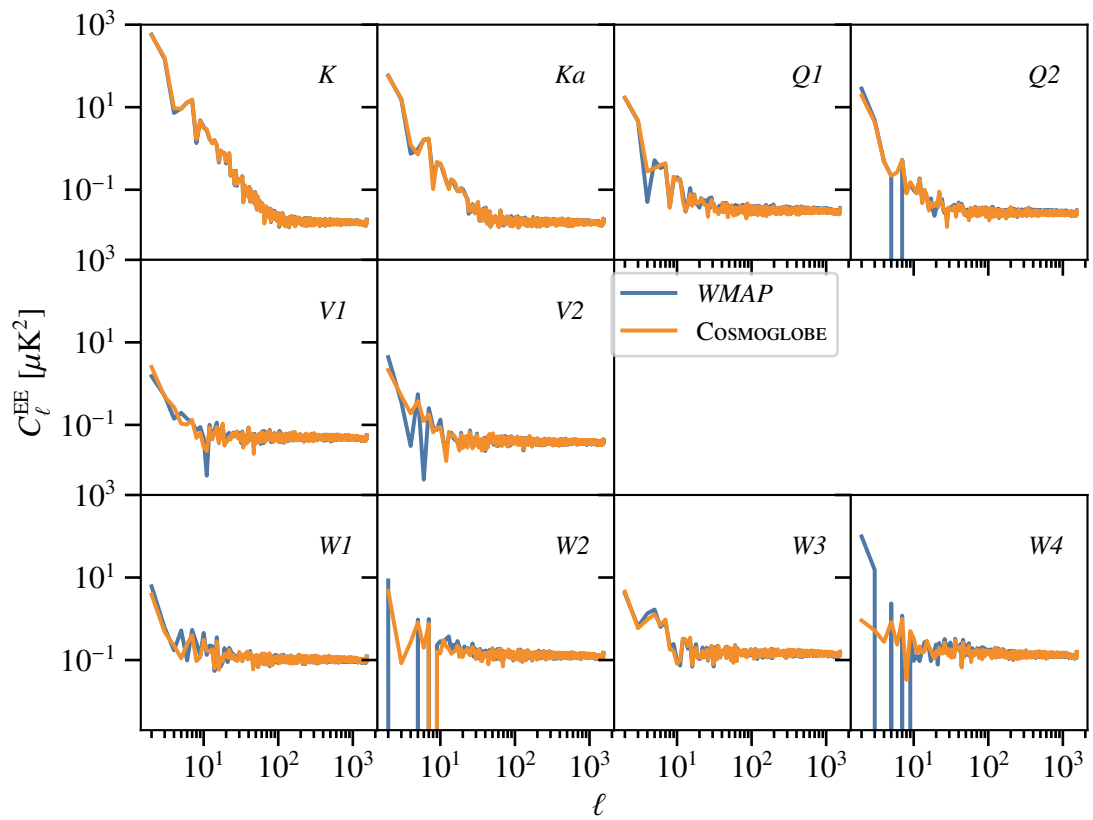
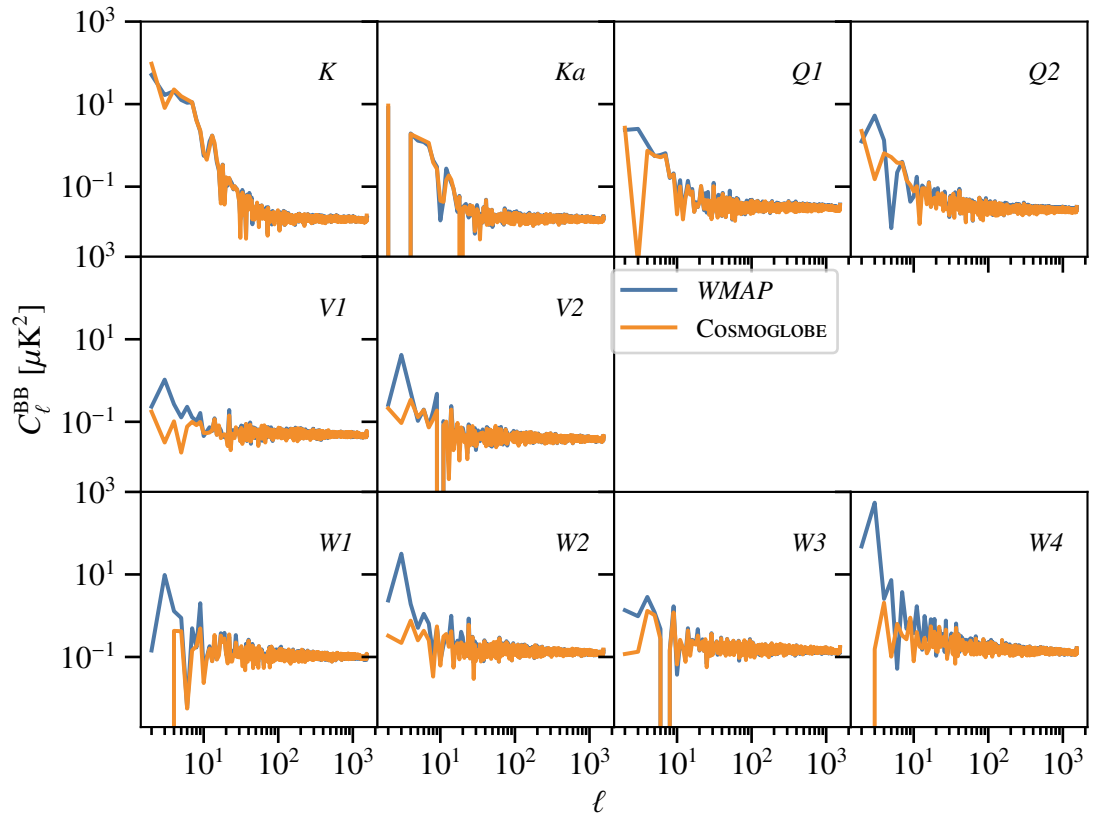
**Fig. 20.** EE power spectra**Fig. 21.** BB power spectra

Table 5. Transmission imbalance template amplitudes for each *WMAP* radiometer as estimated by fitting the official templates to low-resolution difference maps between COSMOGLOBE and *WMAP*. The templates are provided in mK, and the template amplitudes are therefore dimensionless. The fourth column lists the relative decrease in standard deviation, $\sqrt{\sigma_{\text{raw}}^2 - \sigma_{\text{corr}}^2}/\sigma_{\text{raw}}$, after subtracting the best-fit templates in percent.

DA	a_1	a_2	$\Delta\sigma[\%]$
K1	-27.5	-50.6	30
Ka1	-1.4	-1.9	25
Q1	-30.0	-71.6	11
Q2	-7.1	-1.5	20
V1	-32.8	-53.4	6
V2	8.8	-4.1	16
W1	-2.8	4.6	8
W2	-6.9	-3.5	11
W3	29.1	53.4	12
W4	15.5	-6.8	52

low, demonstrating a robust ability to remove poorly measured modes from both experiments thanks to the joint processing.

Columns two and four of Fig. 26 show the differences between the official *WMAP9* and BEYONDPLANCK LFI frequency maps. Similar to the COSMOGLOBE sky map comparisons, we see differences in the Galactic center, and to a lesser degree along the Galactic plane due to the slight differences in the frequency coverage. When comparing the official *WMAP* maps, particularly for *K*-band, we see structures sweeping across large angular scales across the sky, likely due to some effect Duncan totally knows how to describe here in detail. These structures were noted within the BEYONDPLANCK project, particularly in the polarized component separation and large-scale polarized AME studies (Svalheim et al. 2022; Herman et al. 2022). We see that the magnitude of both the Galactic and non-Galactic differences decrease with frequency as the central frequencies approach the foreground minimum where calibration uncertainties are the lowest. All frequency channels in this comparison do show large-scale modes which are difficult to constrain without joint processing.

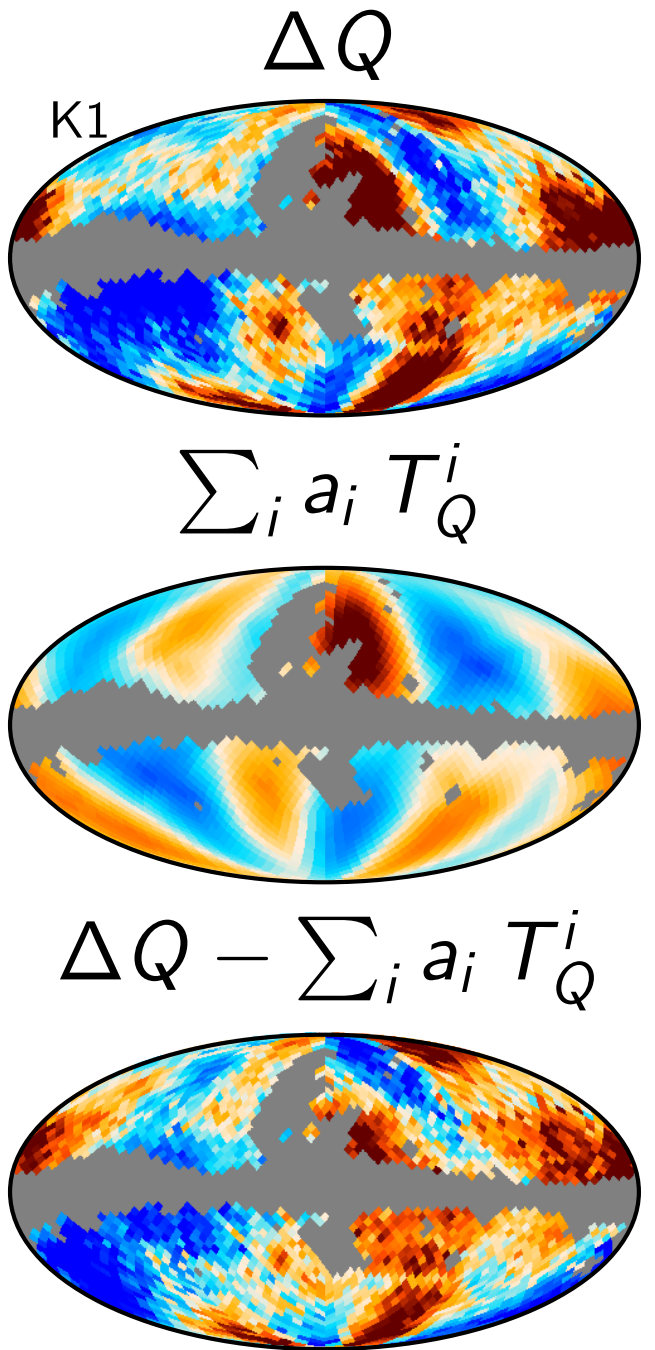


Fig. 22. K-band transmission imbalance templates

6. Preliminary astrophysical results

6.1. CMB results

6.1.1. Solar dipole

6.1.2. Low- ℓ anomalies

Even though the CMB is well described by Λ CDM, there are several anomalies, especially at low multipoles, that seem to be in tension with Λ CDM.

It has been noted since COBE-DMR that the quadrupole amplitude of our CMB is lower than expected from Λ CDM (Bennett et al. 1992). This has later been confirmed in *WMAP* (Hinshaw et al. 2003) and *Planck* (Planck Collaboration Int. XV 2014), but with large discrepancies in mean value and error bars.

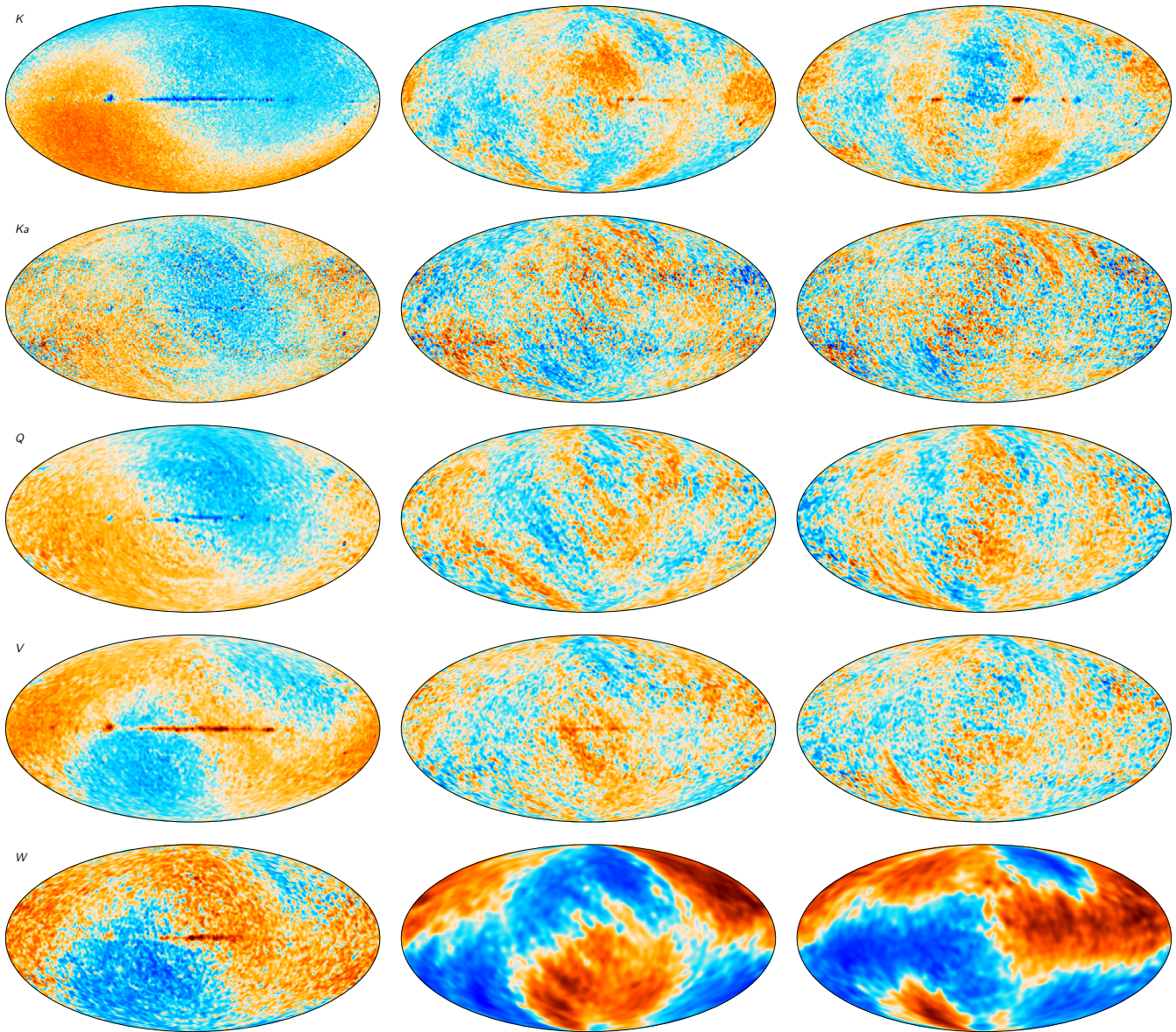


Fig. 23. Difference maps between the COSMOGLOBE and 9-year WMAP frequency maps. Columns show Stokes T , Q , and U parameter maps, while rows show K -, Ka -, Q -, V -, and W -band maps. The temperature maps are smoothed to an angular resolution of 1° FWHM, while the polarization maps are smoothed to 5° FWHM.

6.1.3. Angular temperature power spectrum

6.1.4. Large-scale polarization

6.2. Galactic foregrounds

6.3. WMAP-versus-LFI signal-to-noise ratio comparison

7. Systematic error corrections and uncertainties

7.1. Sky map corrections

7.2. Power spectrum residuals

8. Outstanding issues

8.1. Noise modeling

8.2. V -band quadrupole residual

8.3. Degeneracy between K -band calibration and AME dipole

8.4. Other minor effects

8.4.1. Time-variable bandpass modeling

8.4.2. Polarized sidelobe modeling

9. Conclusions

Ali-Haïmoud, Y., Hirata, C. M., & Dickinson, C. 2009, MNRAS, 395, 1055
Alonso, D., Sanchez, J., Slosar, A., & LSST Dark Energy Science Collaboration.

2019, MNRAS, 484, 4127

Andersen et al. 2022, A&A, in press [[arXiv:2201.08188](https://arxiv.org/abs/2201.08188)]

Barnes, C., Hill, R. S., Hinshaw, G., et al. 2003, ApJS, 148, 51

Barrett, R., Berry, M. W., Chan, T. F., et al. 1994, Templates for the Solution of Linear Systems (Society for Industrial and Applied Mathematics)

Basyrov et al. 2022, A&A, submitted [[arXiv:2208.14293](https://arxiv.org/abs/2208.14293)]

Bennett, C. L., Bay, M., Halpern, M., et al. 2003a, ApJ, 583, 1

Bennett, C. L., Halpern, M., Hinshaw, G., et al. 2003b, ApJS, 148, 1

Bennett, C. L., Larson, D., Weiland, J. L., et al. 2013, ApJS, 208, 20

Bennett, C. L., Smoot, G. F., Hinshaw, G., et al. 1992, ApJ, 396, L7

BeyondPlanck. 2022, A&A, submitted [[arXiv:2011.05609](https://arxiv.org/abs/2011.05609)]

Dicke, R. H., Peebles, P. J. E., Roll, P. G., & Wilkinson, D. T. 1965, ApJ, 142, 414

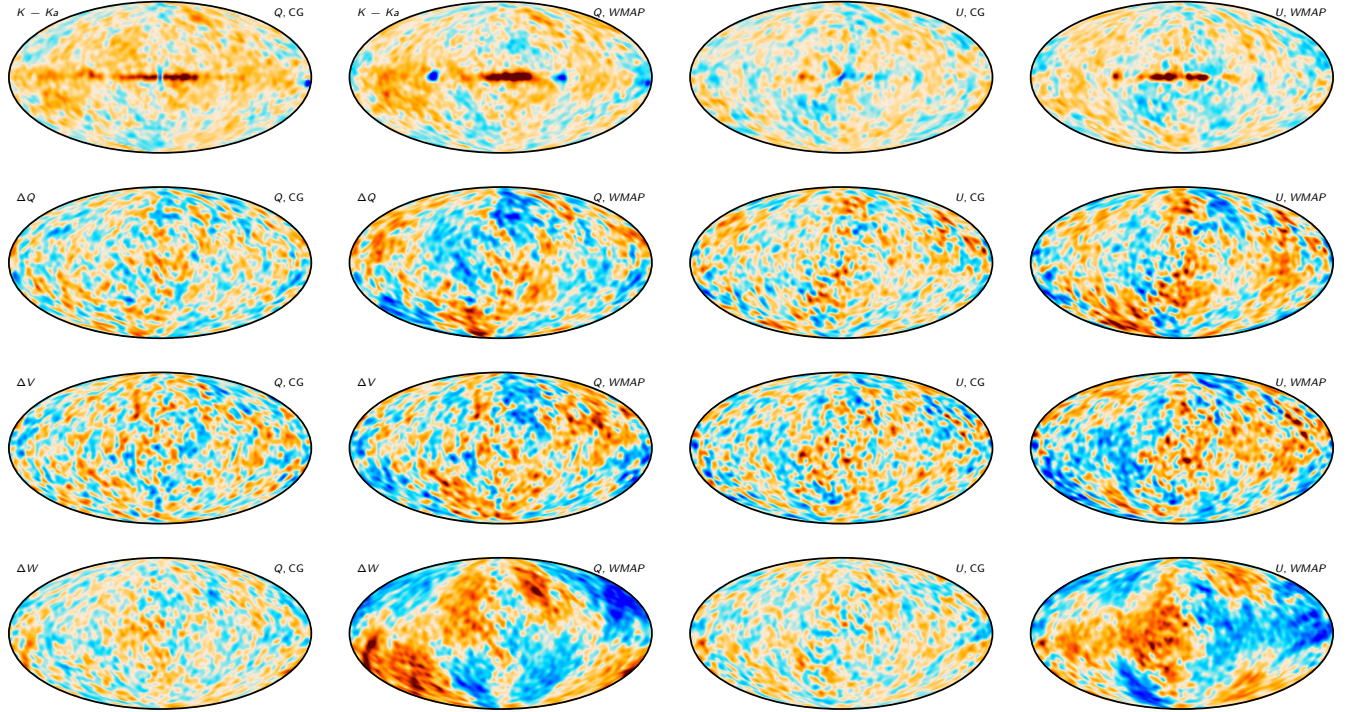
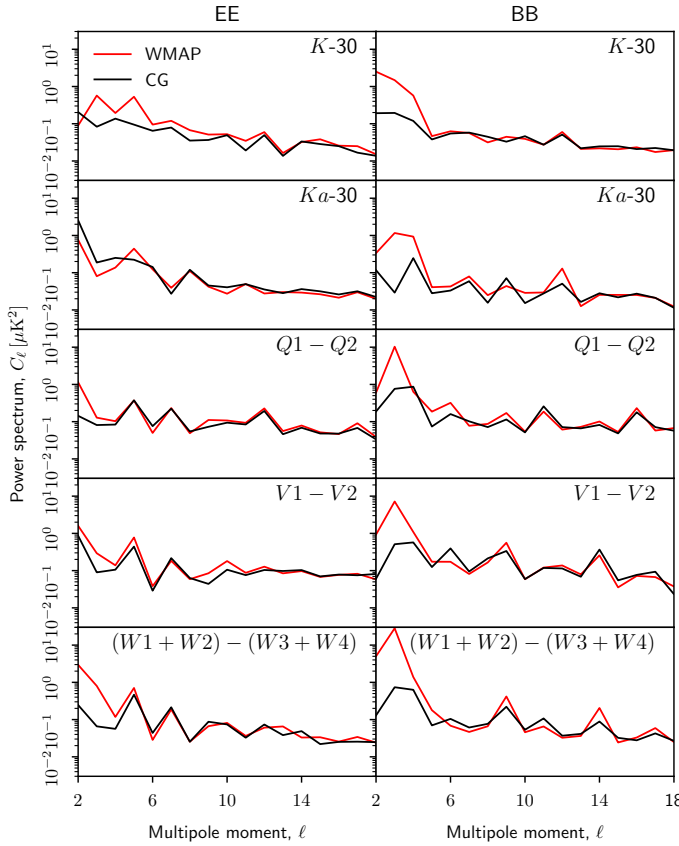
Frigo, M. & Johnson, S. G. 2005, Proceedings of the IEEE, 93, 216, special issue on “Program Generation, Optimization, and Platform Adaptation”

Galloway et al. 2022, A&A, in press [[arXiv:2201.03509](https://arxiv.org/abs/2201.03509)]

Gjerløw et al. 2022, A&A, submitted [[arXiv:2011.08082](https://arxiv.org/abs/2011.08082)]

Greason, M. R., Limon, M., Wollack, E., et al. 2012, Nine-Year Explanatory Supplement, 5th edn., Greenbelt, MD: NASA/GSFC

Haslam, C. G. T., Salter, C. J., Stoffel, H., & Wilson, W. E. 1982, A&AS, 47, 1

**Fig. 24.** Half-difference maps, smoothed by 10° .**Fig. 25.** Half-difference spectra.

- Hinshaw, G., Weiland, J. L., Hill, R. S., et al. 2009, ApJS, 180, 225
 Hu, W., Fukugita, M., Zaldarriaga, M., & Tegmark, M. 2001, ApJ, 549, 669
 Ihle et al. 2022, A&A, in press [[arXiv:2011.06650](#)]
 Jarosik, N., Barnes, C., Bennett, C. L., et al. 2003a, ApJS, 148, 29
 Jarosik, N., Barnes, C., Greason, M. R., et al. 2007, ApJS, 170, 263
 Jarosik, N., Bennett, C. L., Dunkley, J., et al. 2011, ApJS, 192, 14
 Jarosik, N., Bennett, C. L., Halpern, M., et al. 2003b, ApJS, 145, 413
 Keihänen et al. 2022, A&A, in press [[arXiv:2011.06024](#)]
 Lange, A. E., Ade, P. A., Bock, J. J., et al. 2001, Phys. Rev. D, 63, 042001
 Larson, D., Weiland, J. L., Hinshaw, G., & Bennett, C. L. 2015, ApJ, 801, 9
 Mather, J. C., Cheng, E. S., Cottingham, D. A., et al. 1994, ApJ, 420, 439
 Mather, J. C., Fixsen, D. J., Shafer, R. A., Mosier, C., & Wilkinson, D. T. 1999, ApJ, 512, 511
 Notari, A. & Quartin, M. 2015, Journal of Cosmology and Astroparticle Physics, 2015, 047–047
 Page, L., Jackson, C., Barnes, C., et al. 2003, ApJ, 585, 566
 Penzias, A. A. & Wilson, R. W. 1965, ApJ, 142, 419
 Planck Collaboration II. 2016, A&A, 594, A2
 Planck Collaboration I. 2020, A&A, 641, A1
 Planck Collaboration II. 2020, A&A, 641, A2
 Planck Collaboration III. 2020, A&A, 641, A3
 Planck Collaboration Int. XV. 2014, A&A, 565, A103
 Planck Collaboration Int. XLVI. 2016, A&A, 596, A107
 Press, W. H., Teukolsky, S. A., Vetterling, W. T., & Flannery, B. P. 2007, Numerical Recipes 3rd Edition: The Art of Scientific Computing, 3rd edn. (USA: Cambridge University Press)
 Remazeilles, M., Dickinson, C., Banday, A. J., Bigot-Sazy, M.-A., & Ghosh, T. 2015, MNRAS, 451, 4311
 Silsbee, K., Ali-Haïmoud, Y., & Hirata, C. M. 2011, MNRAS, 411, 2750
 Smoot, G. F., Bennett, C. L., Kogut, A., et al. 1992, ApJ, 396, L1
 Stevenson, M. A. 2014, The Astrophysical Journal, 781, 113
 Svalheim et al. 2022, A&A, in press [[arXiv:2011.08503](#)]
 Tramonte, D., Génova-Santos, R. T., Rubiño-Martín, J. A., et al. 2023, MNRAS, 519, 3432
 van der Vorst, H. A. 1992, SIAM Journal on Scientific and Statistical Computing, 13, 631
 Watts et al. 2022, A&A, in press [[arXiv:2202.11979](#)]
 Weiland, J. L., Odegard, N., Hill, R. S., et al. 2011, ApJS, 192, 19

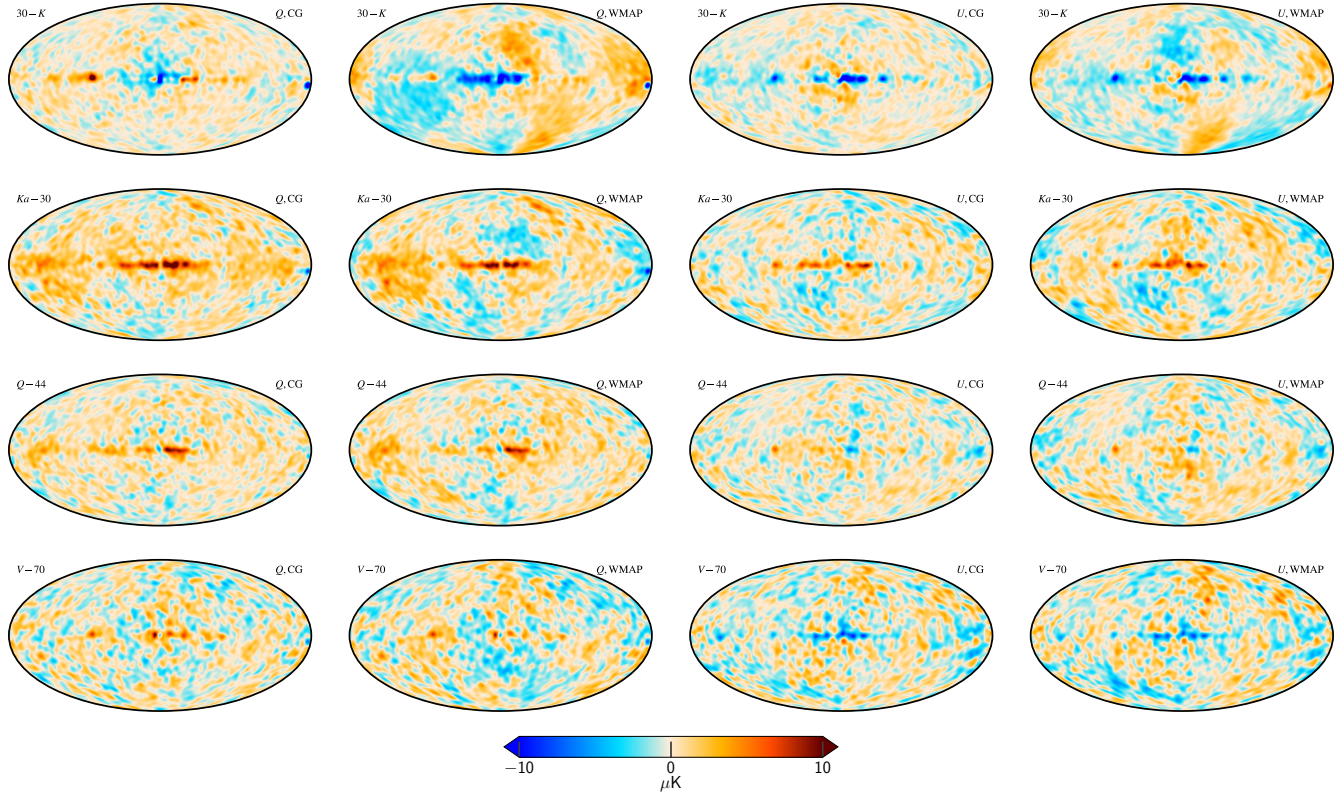


Fig. 26. Difference maps between similar WMAP and LFI frequency maps. The comparison plots go, by column: Stokes Q for the COSMOGLOBE sky maps, Stokes Q for official WMAP and BEYONDPLANCK data products, Stokes U for the COSMOGLOBEsky maps, and Stokes U for the official data products. (Top row) WMAP LFI 30 GHz minus K -band, scaled by the synchrotron power-law. (Top middle row) WMAP Ka -band minus LFI 30 GHz, also scaled by the synchrotron power-law. (Bottom middle row) WMAP Q -band compared to the LFI 44 GHz sky maps, scaled by the synchrotron power-law. (Bottom row) WMAP V -band minus LFI 70 GHz, with unit scalings for each band.

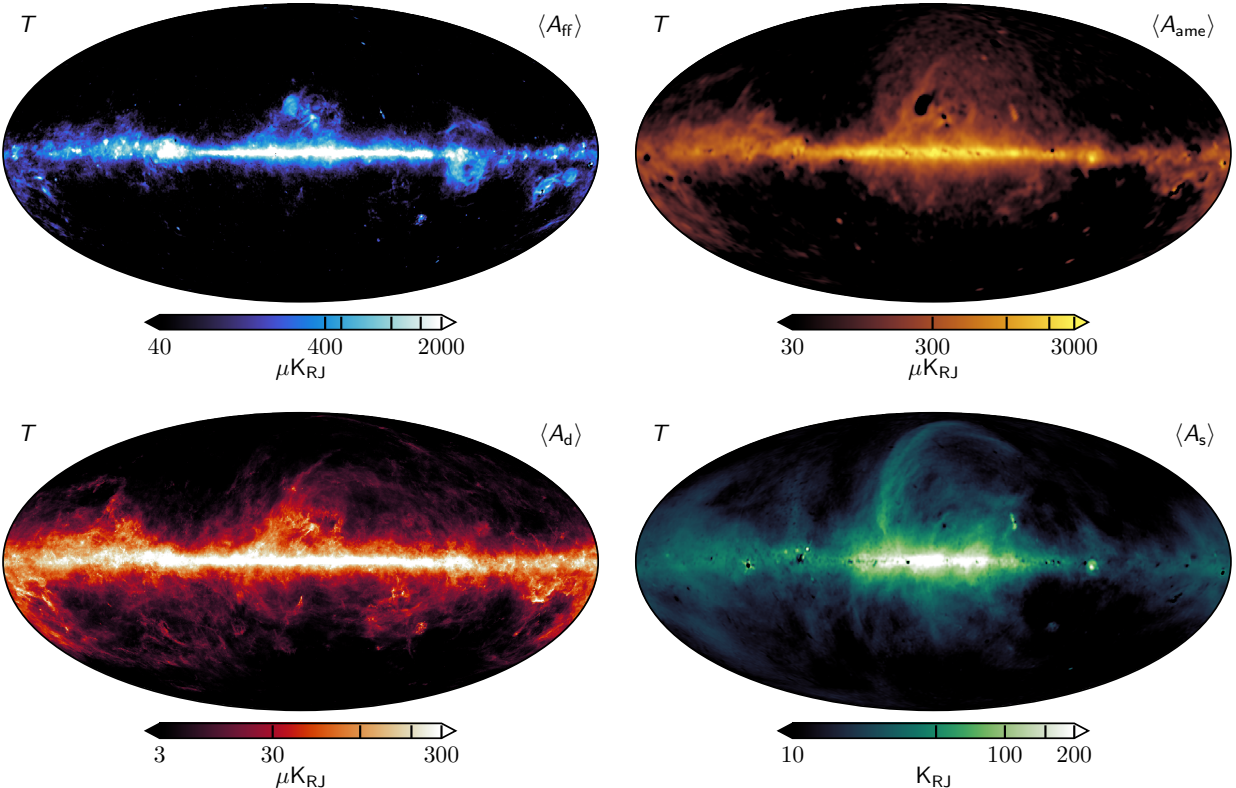


Fig. 27. Foreground intensity maps

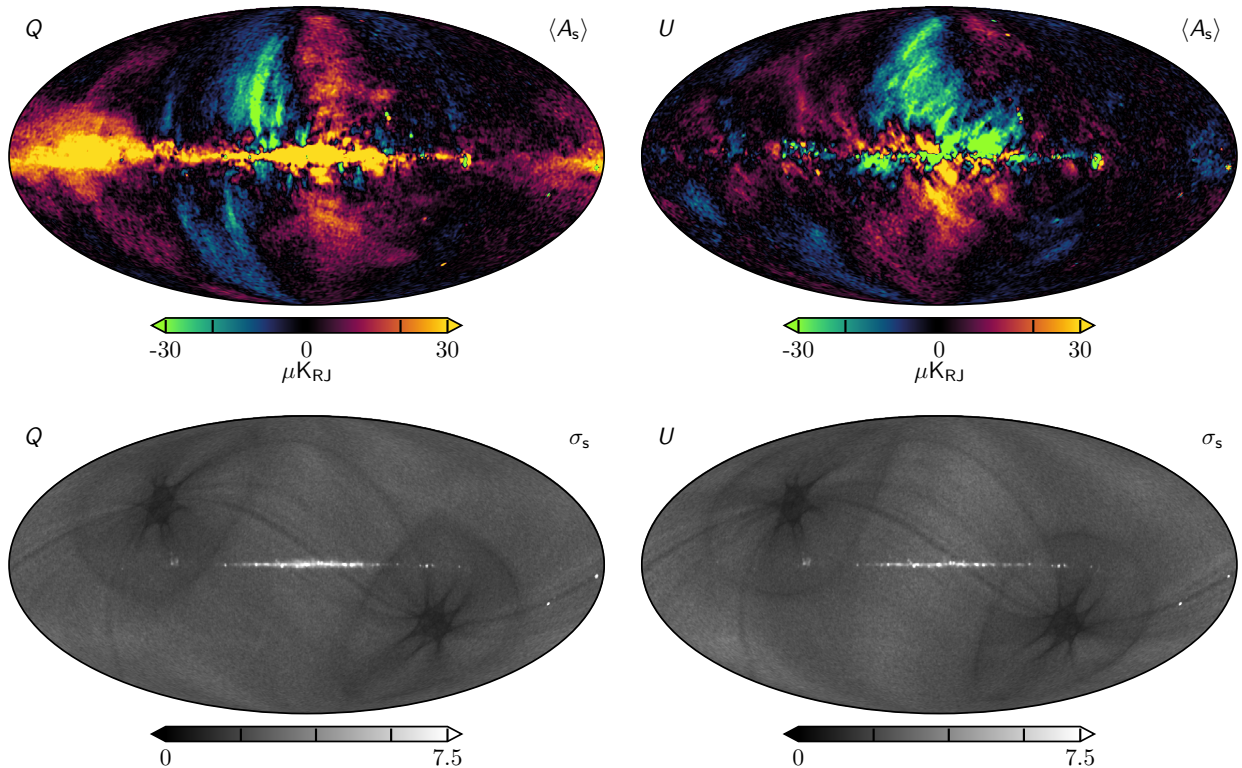


Fig. 28. Polarized synchrotron maps and their standard deviations

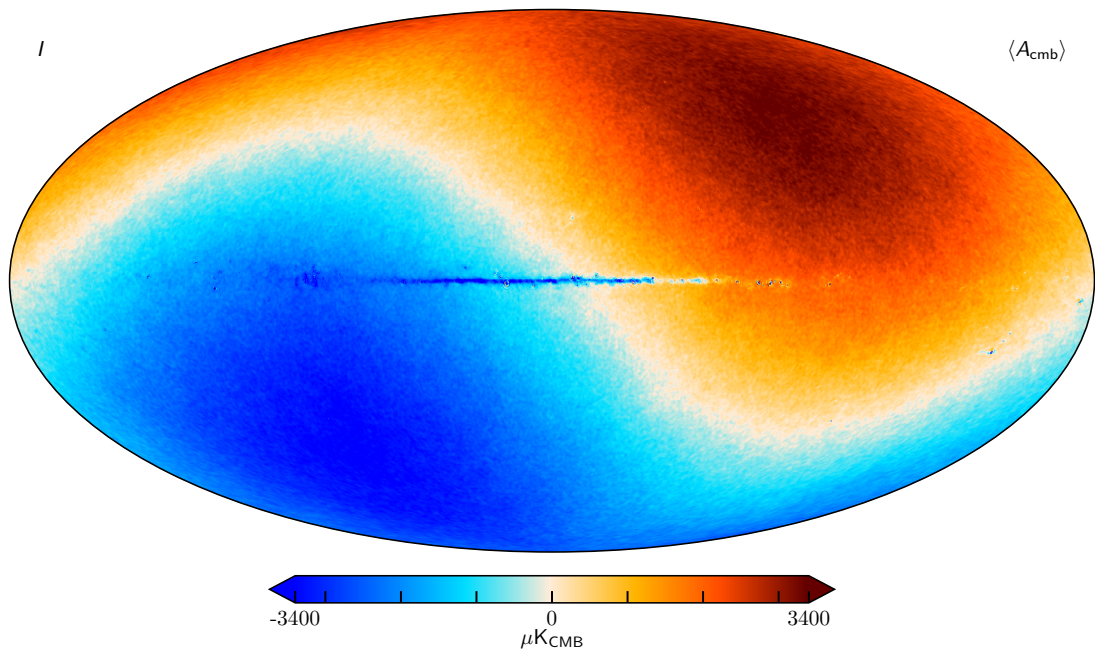


Fig. 29. Posterior mean CMB Cosmoglobe temperature map, smoothed to an angular resolution of 14' FWHM.

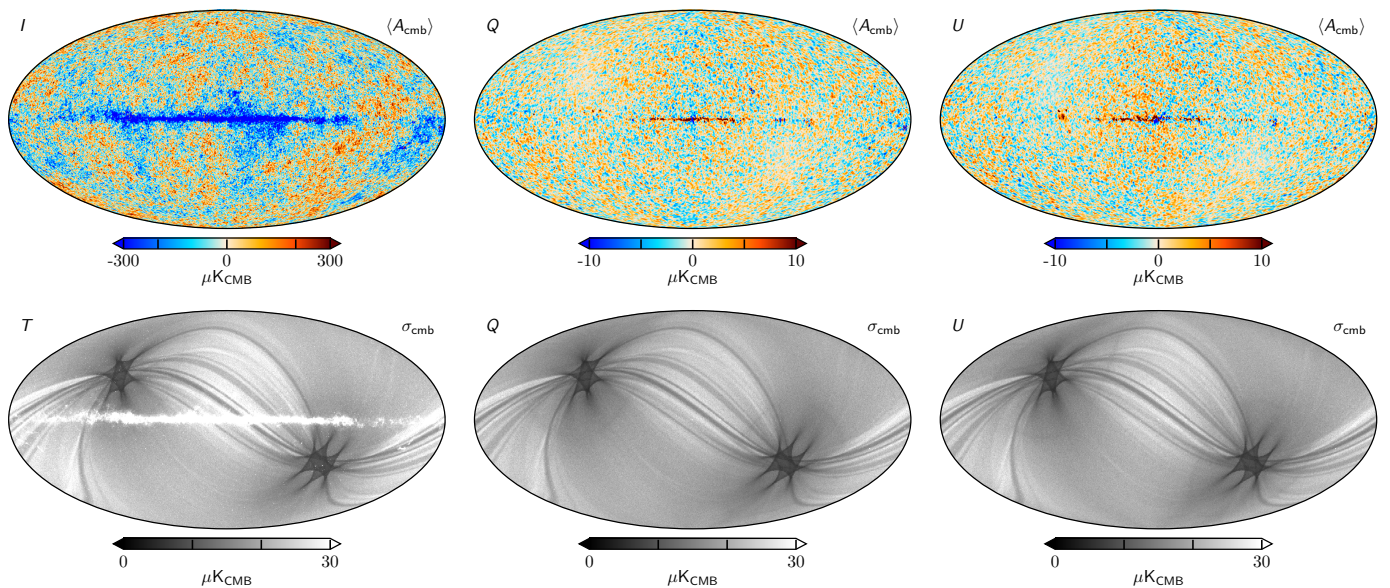


Fig. 30. Posterior mean CMB Cosmoglobe maps and their standard deviation.

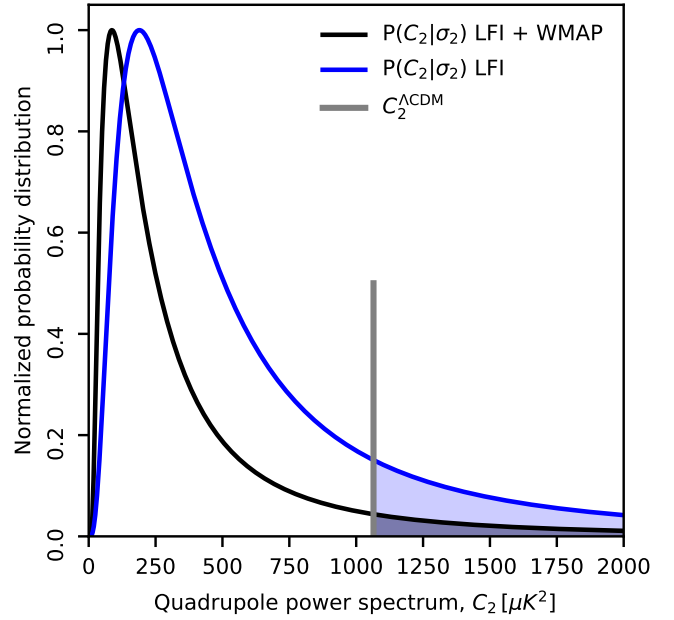
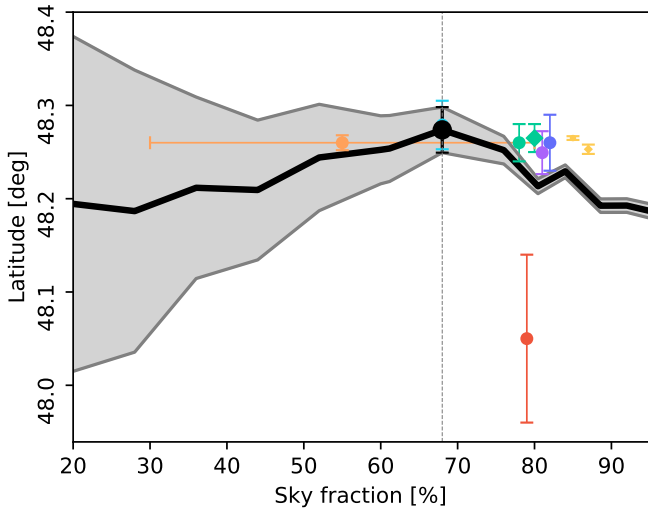
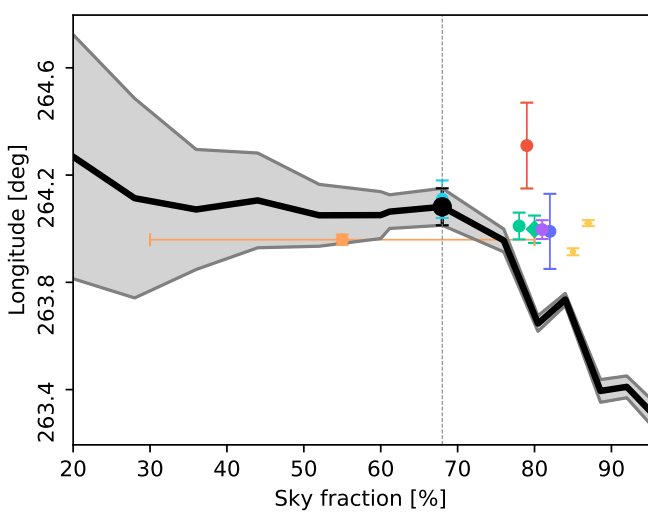
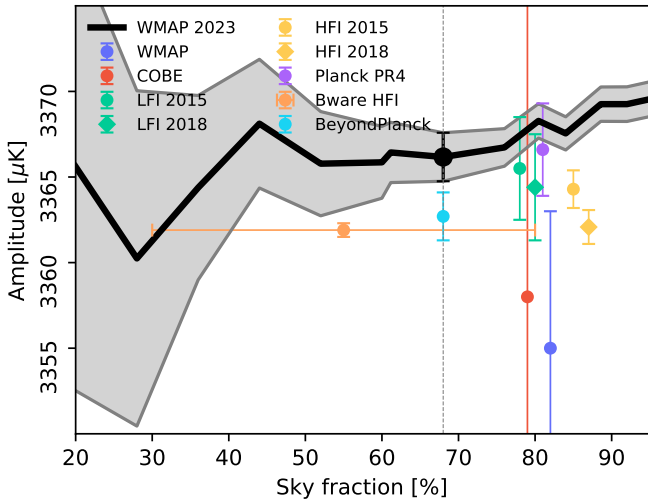


Fig. 31. Marginal probability distribution of the ensemble-averaged C_2 given the data, $P(C_2|d)$, as measured by COSMOGLOBE (black) and BEYONDPLANCK (blue).

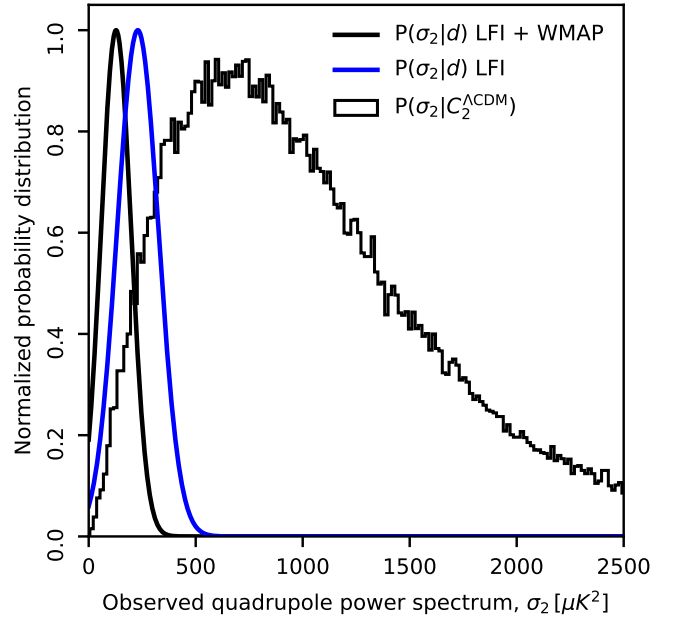


Fig. 32. Histogram of 100 000 realizations of C_2 given $C_2^{\Lambda\text{CDM}} = 1064.7$ compared with the measured power spectrum σ_2 of our universe for COSMOGLOBE (black) and BEYONDPLANCK (blue).

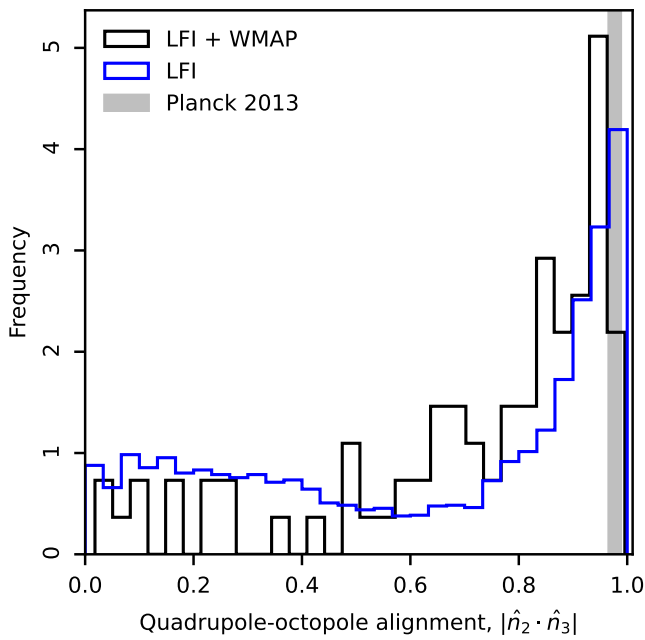


Fig. 33. The quadrupole-octopole alignment of COSMOGLOBE compared with BEYONDPLANCK.

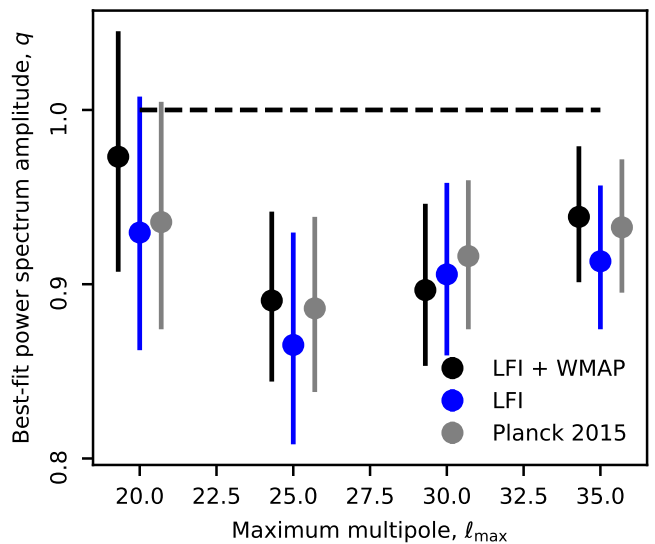


Fig. 35. Best-fit amplitude, q , of the low multipole power spectrum $C_\ell = qC_\ell^{\Lambda\text{CDM}}$, $2 \leq \ell \leq \ell_{\max}$ compared to *Planck*2015 (grey) and BeyondPlanck (blue).

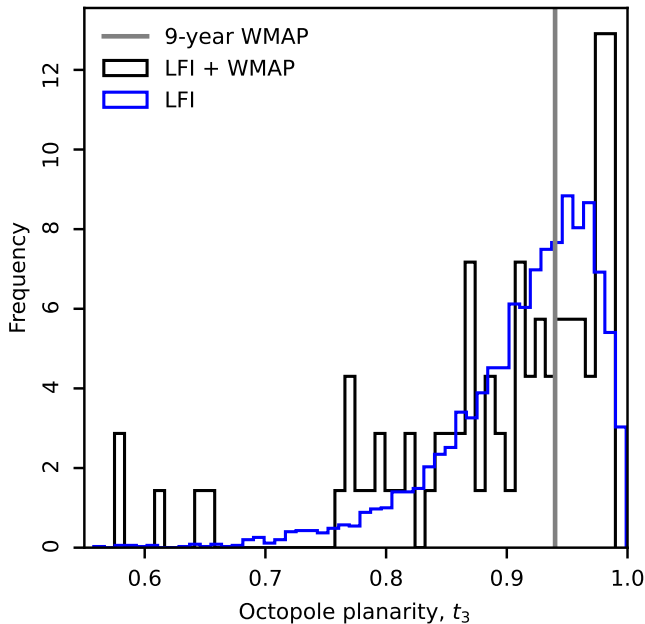


Fig. 34. The octopole planarity statistics t_3 compared with the BEYONDPLANCK analysis (blue).

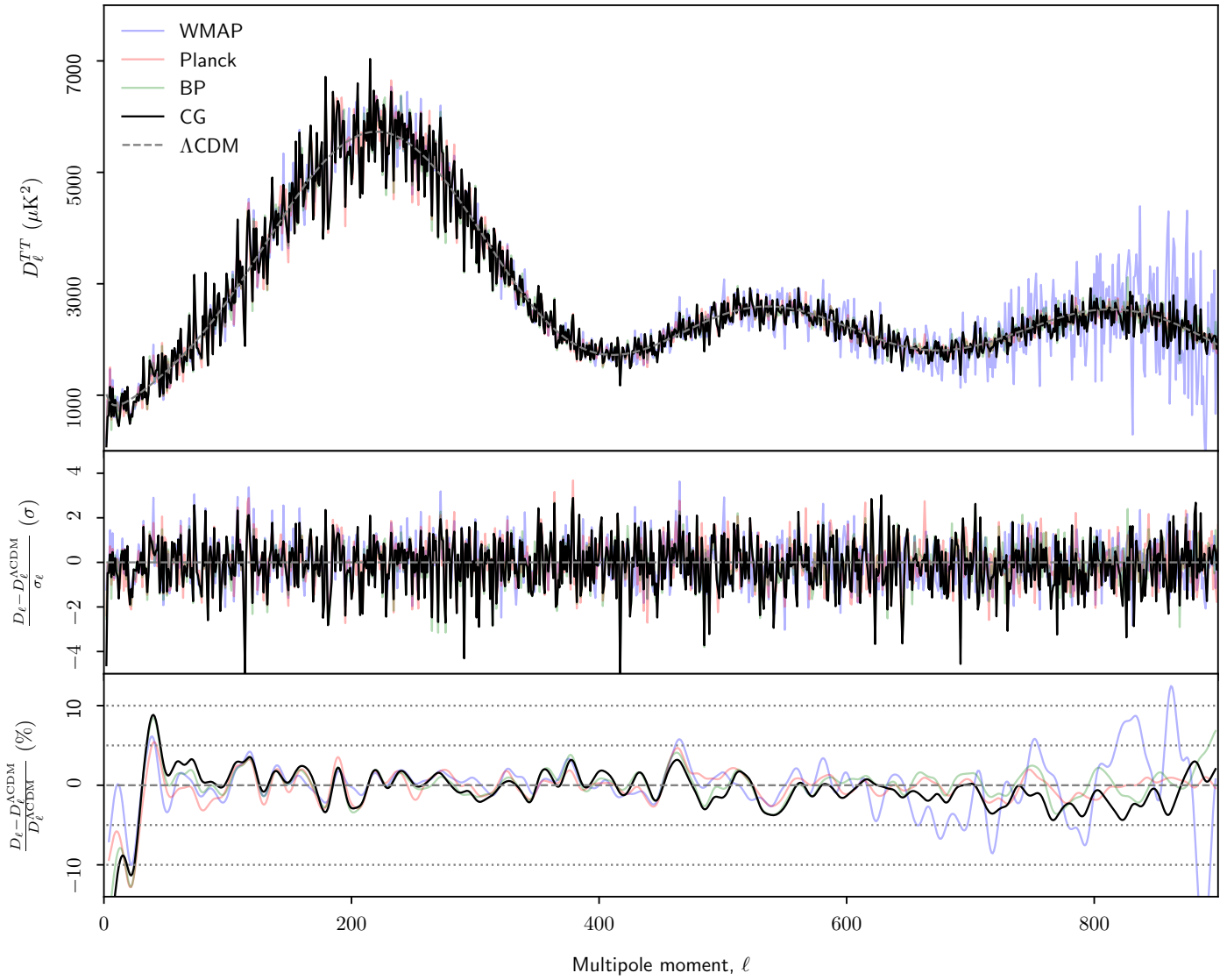
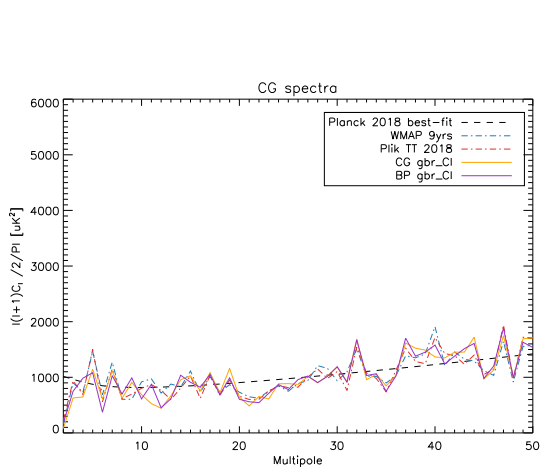
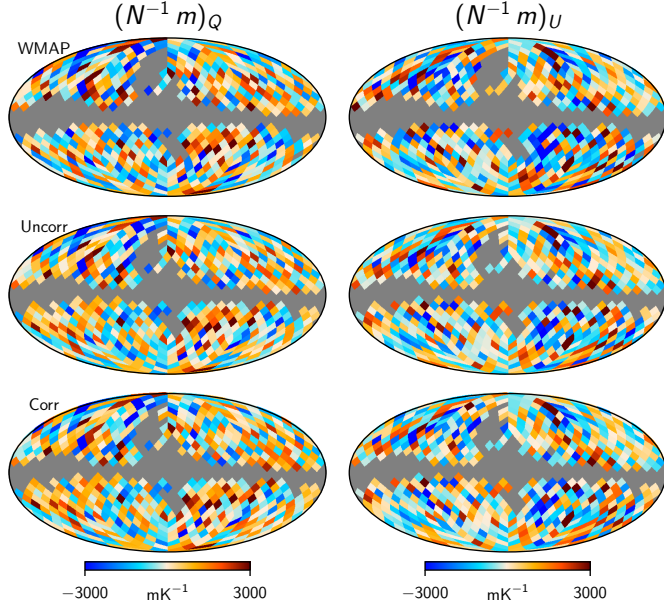
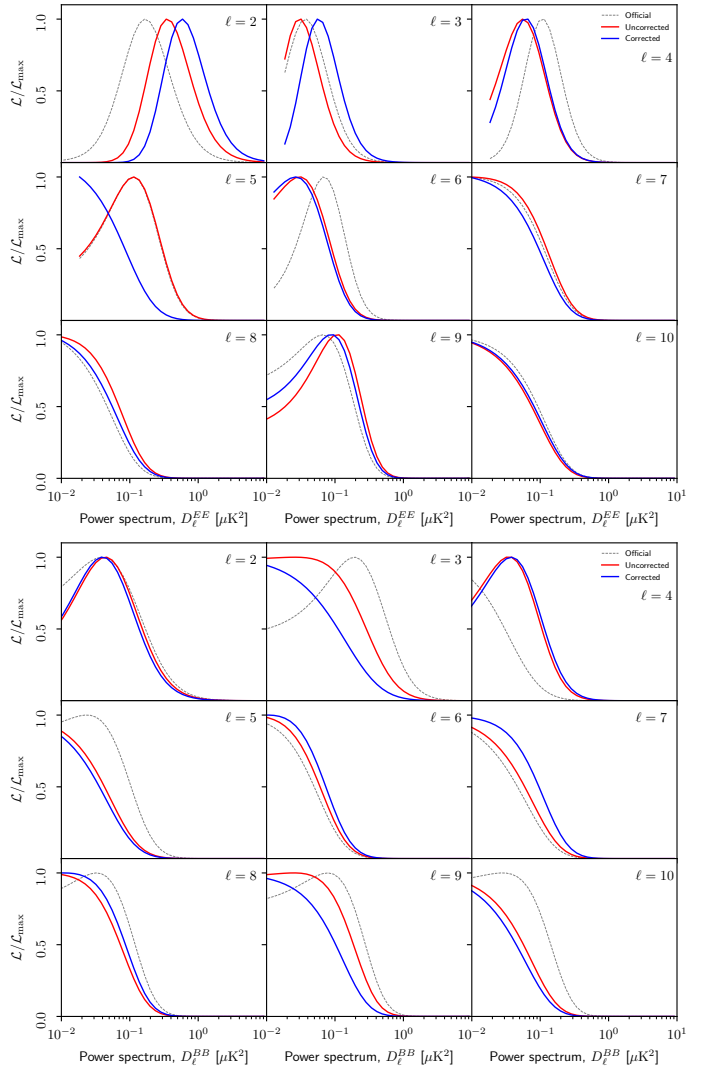


Fig. 36. Temperature power spectra from COSMOGLOBE, BEYONDPLANCK, WMAP9, and *Planck* DR4, compared with the *Planck* 2018 ΛCDM prediction.

**Fig. 37.** Low-multipole temperature power spectrum**Fig. 38.** Noise-weighted likelihood input maps.**Fig. 39.** Likelihood slices

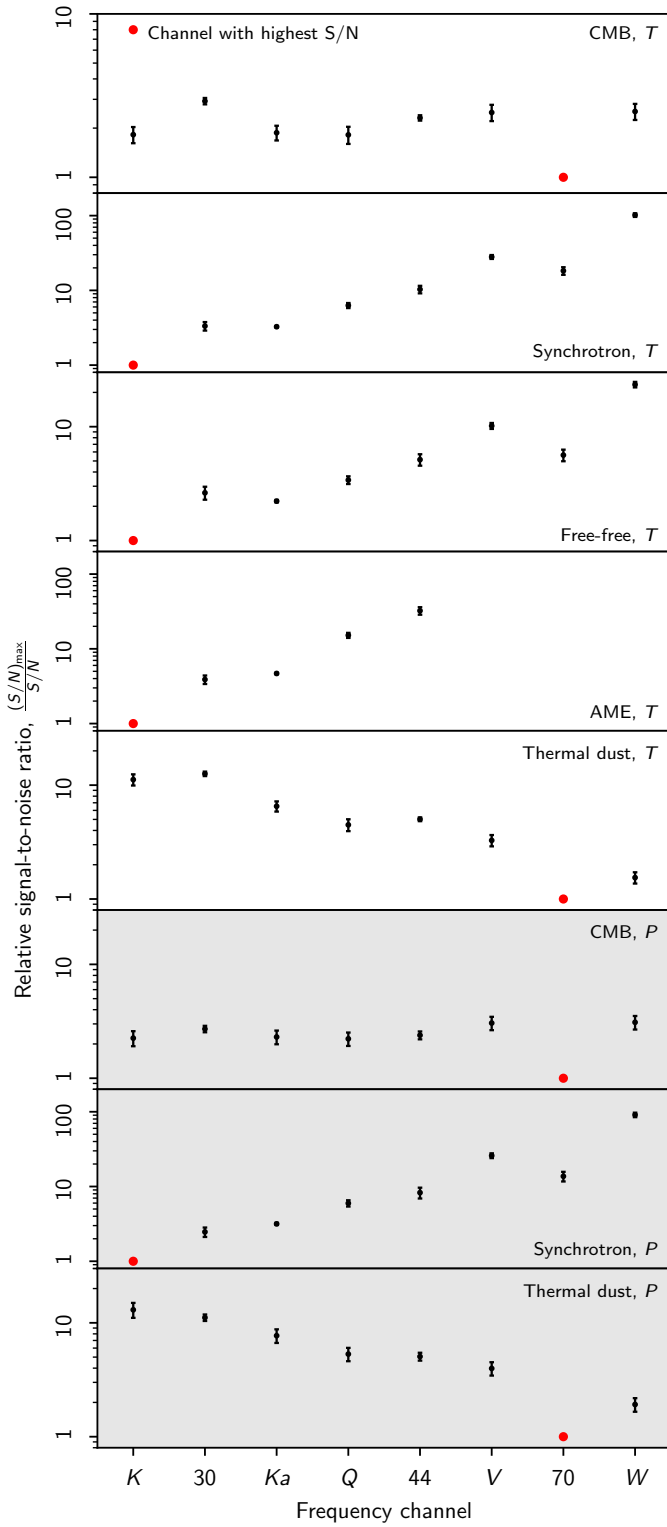


Fig. 40. Relative signal-to-noise ratios for WMAP and LFI channels and various components.

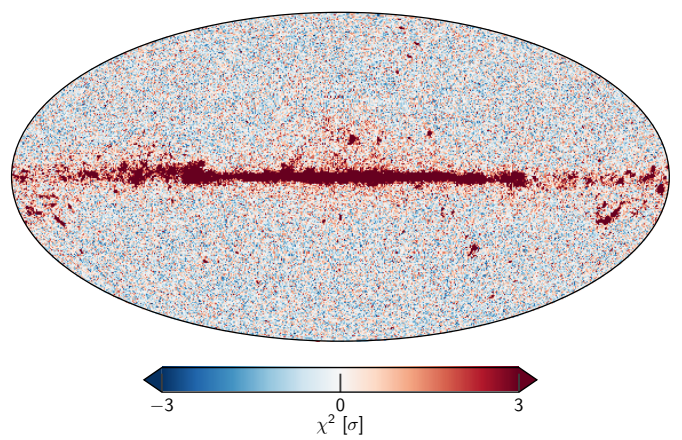


Fig. 41. Reduced- χ^2 , using $n_{\text{dof}} = 300$, which comes from fitting to the regions outside of the K -band processing mask.

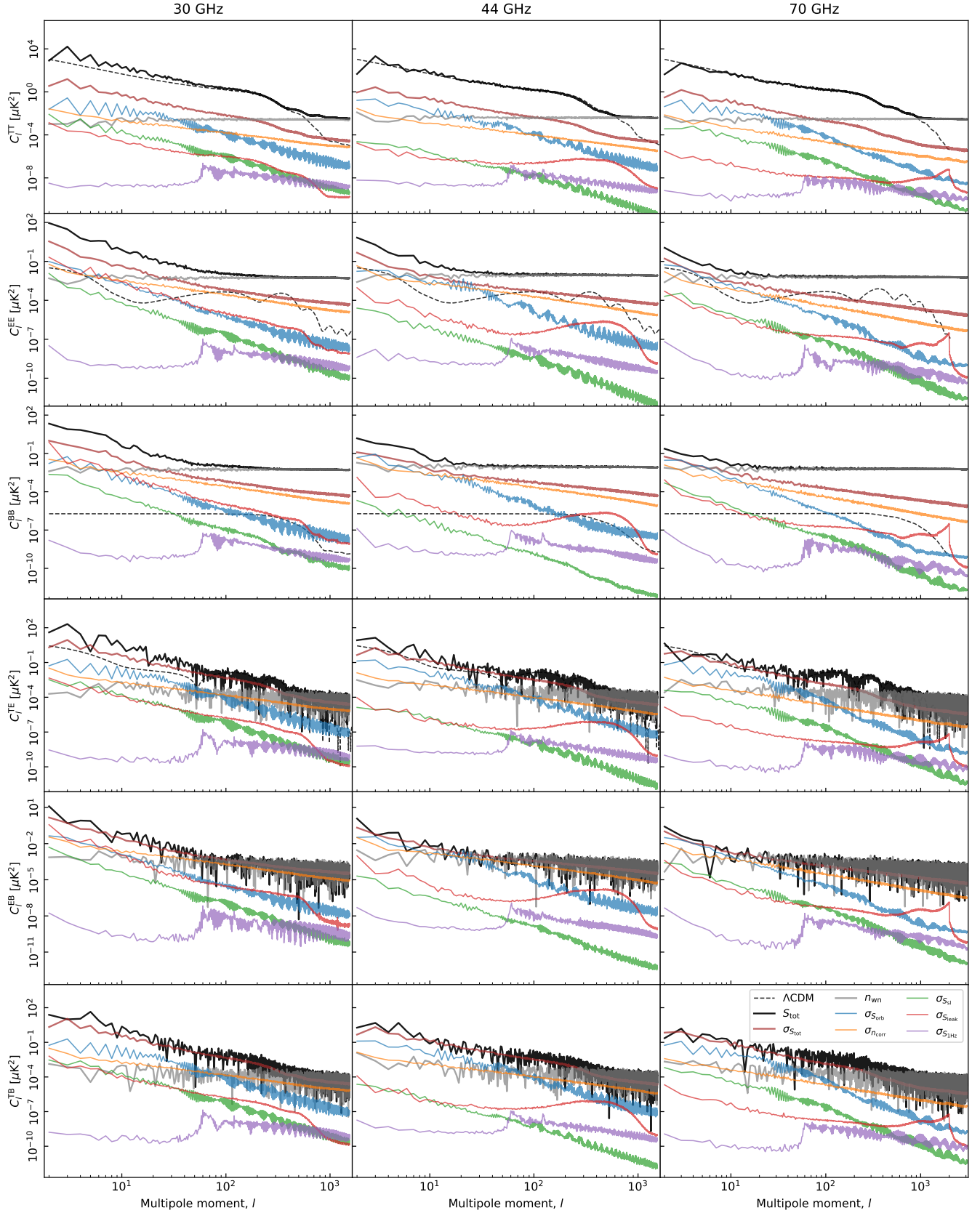


Fig. 42. Pseudo-spectrum standard deviation for each instrumental systematic correction shown in Figs. ??–?? (thin colored lines). For comparison, thick black lines show spectra for the full coadded frequency map; thick red lines show the standard deviation of the same (i.e., the full systematic uncertainty); gray lines show white noise; and dashed black lines show the best-fit *Planck* 2018 ΛCDM power spectrum convolved with the instrument beam. Columns show results for 30, 44 and 70 GHz, respectively, while rows show results for each of the six polarization states (TT, EE, BB, TE, TB, and EB). All spectra have been derived outside the CMB confidence mask presented by [Andersen et al. \(2022\)](#) using the HEALPix *anafast* utility, correcting only for sky fraction and not for mask mode coupling.

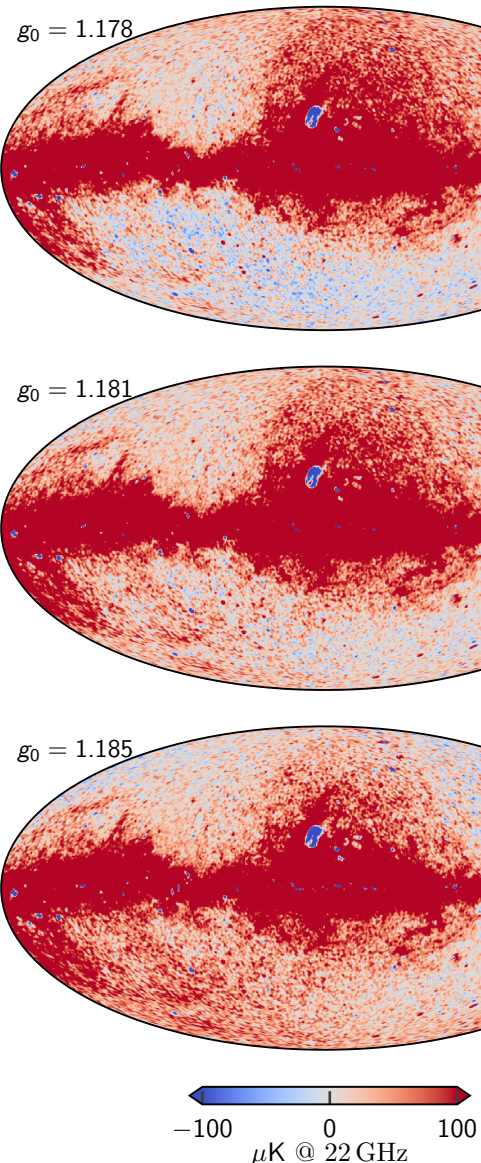


Fig. 43. Dependence on AME amplitude evaluated at 22 GHz as a function of absolute calibration. Each map comes from the fifth iteration of a dedicated `Commander` run that fixed g_0 while letting all other TOD parameters be fit. The values of $g_0 = 1.178$ and $g_0 = 1.185$ represent 3.5σ draws from the prior distribution with mean 1.1815 and standard deviation 0.001. The dipole visible in the top and bottom panels is aligned perfectly with the Solar dipole, and is directly due to variations in the K -band absolute calibration.



Fig. 44. Difference maps between the *Planck* 30 GHz and *WMAP* K-band maps. The columns are (1) *Planck* 2018 v. *WMAP*9, (2) *Planck* PR4 v. *WMAP*9, (3) BEYONDPLANCK v. *WMAP*9, and (4) COSMOGLOBE *Planck* 30 GHz and *WMAP* K-band both produced in this paper. All maps have been smoothed to a common resolution of 2° FWHM, and the K-band map has been scaled by 0.495 to account for different central frequencies, assuming a synchrotron spectral index $\beta_s = -3.1$.

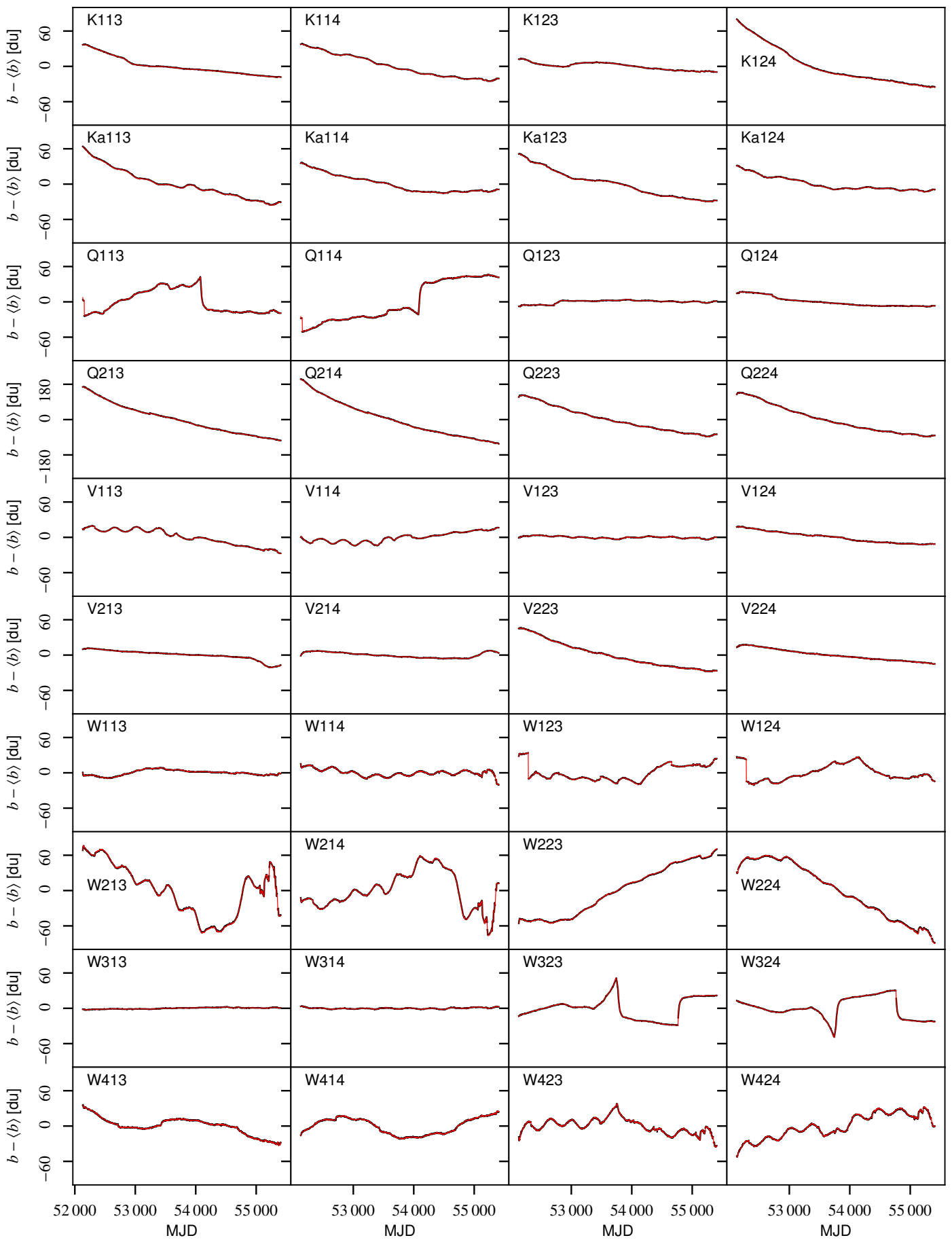
Appendix A: Survey of instrumental parameters

Appendix A.1: Gain, baselines, noise and χ^2

Appendix A.2: Transmission imbalance

Appendix B: WMAP frequency map survey

Appendix C: Comparison with BEYONDPLANCK LFI results

**Fig. A.1.** baseline.

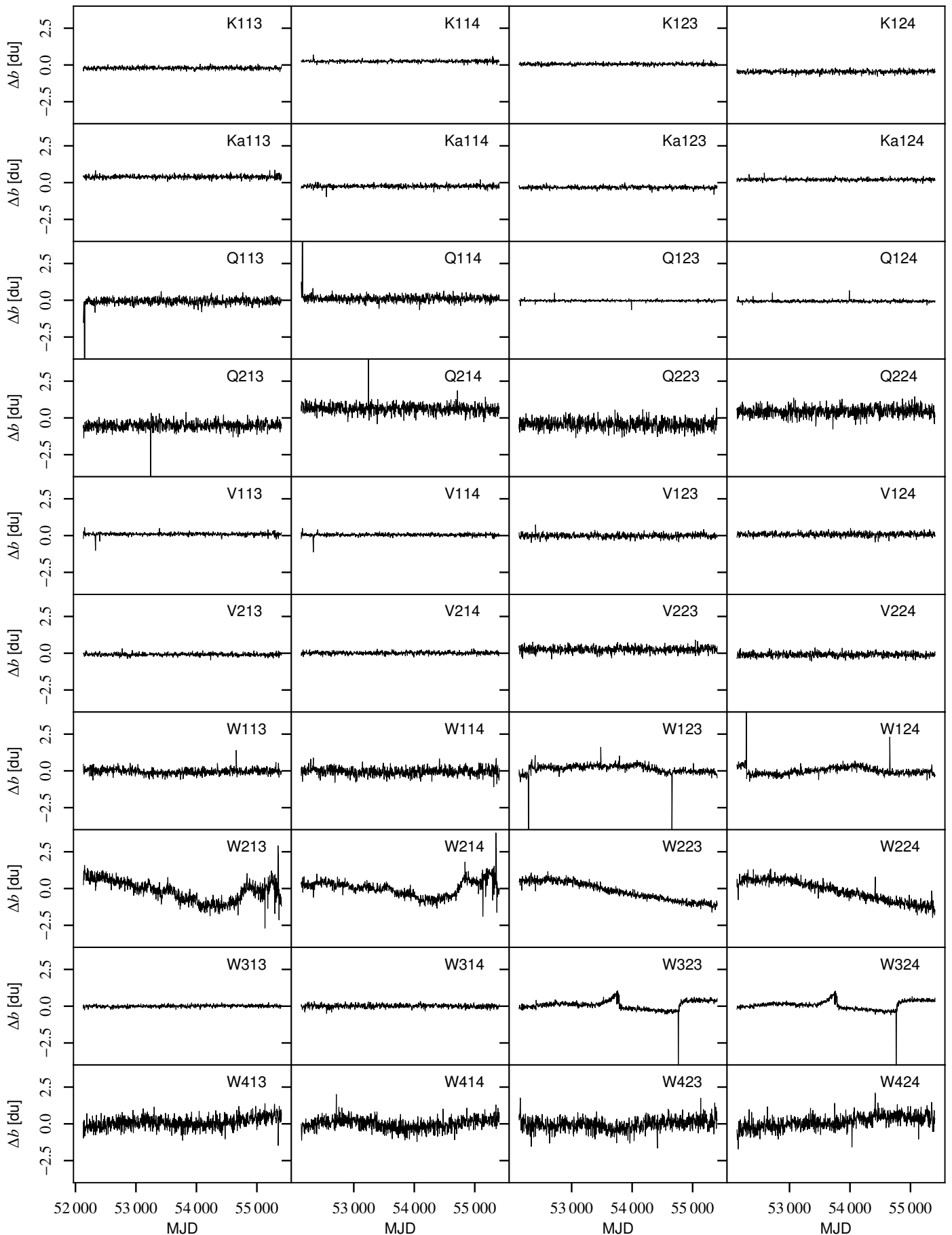
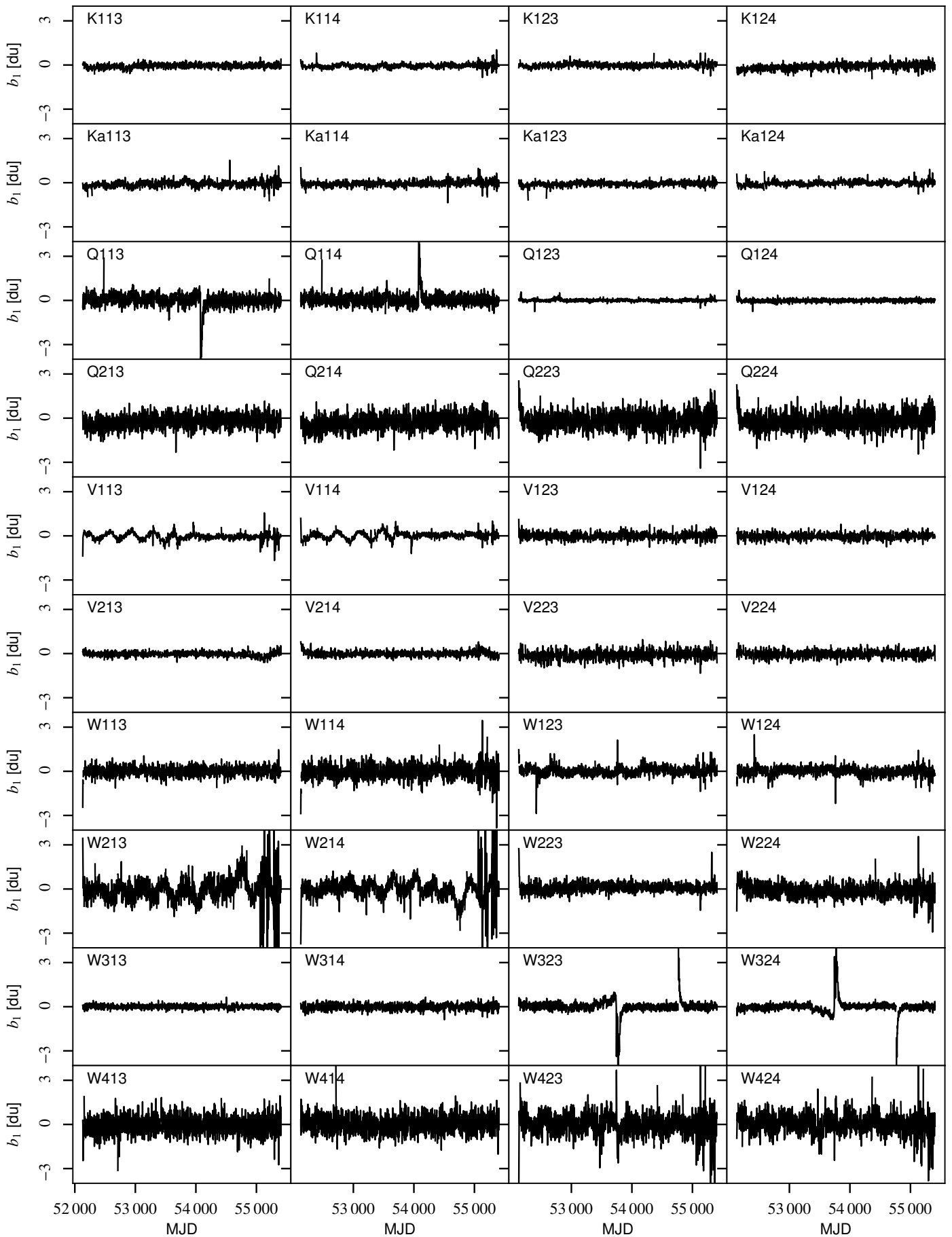
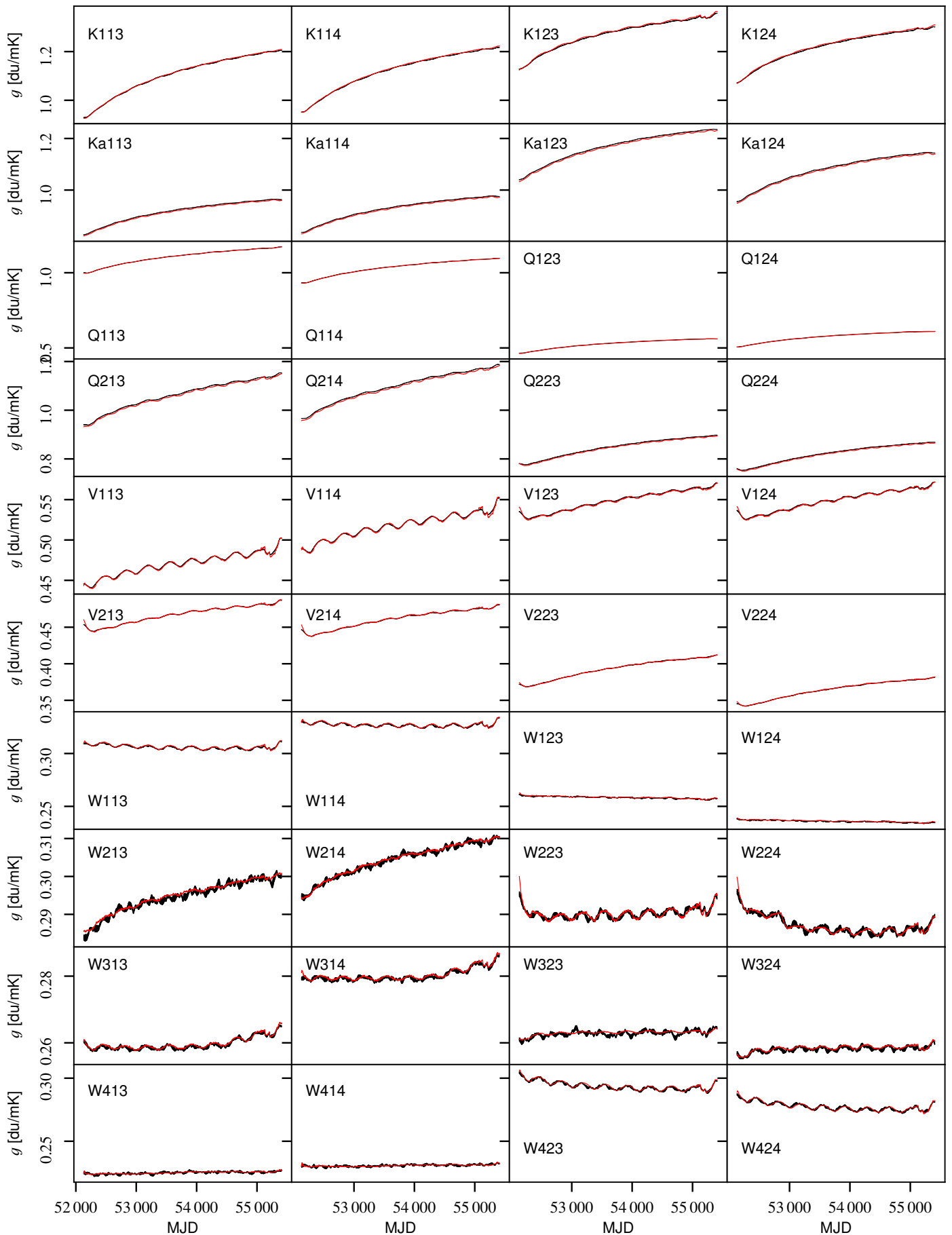
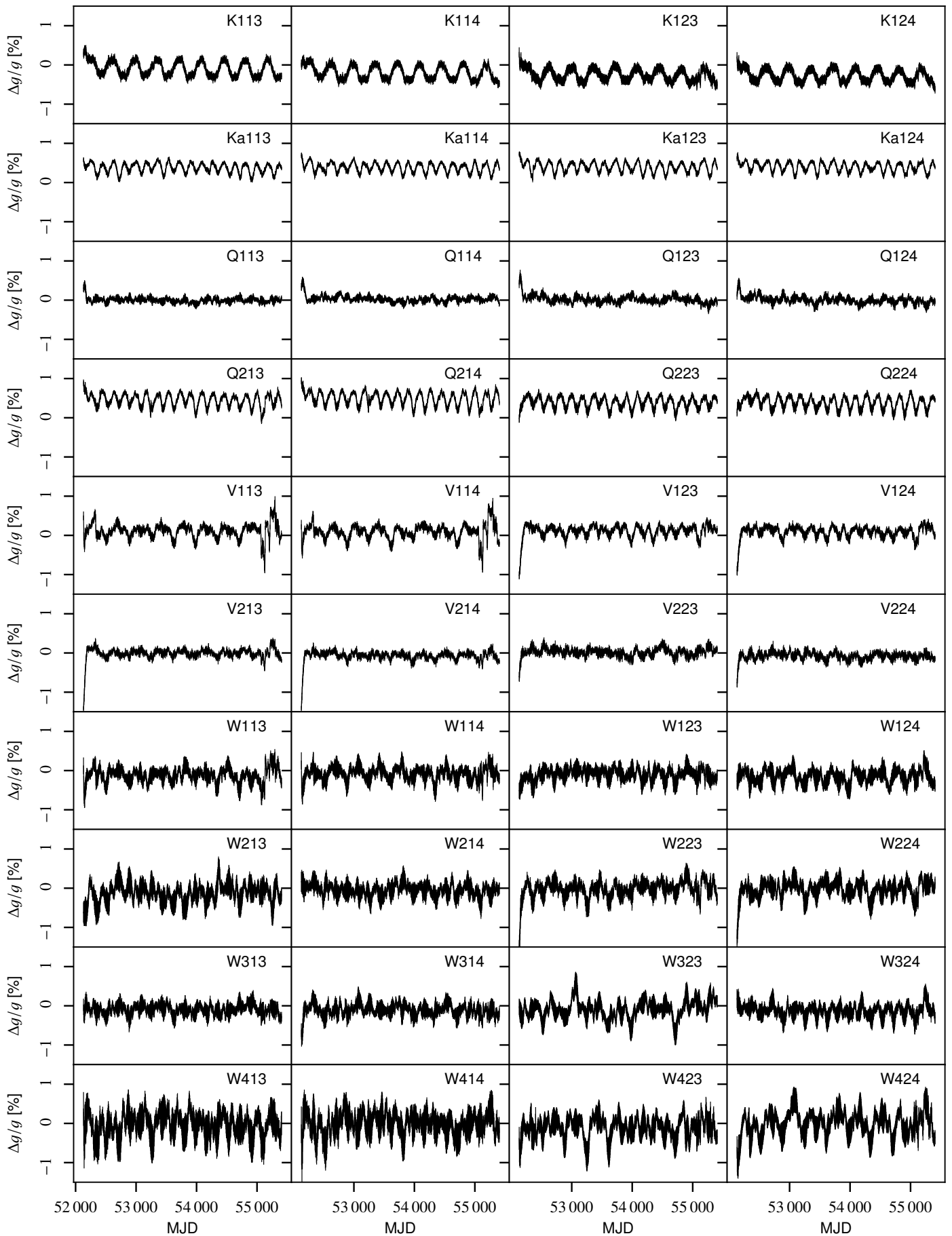
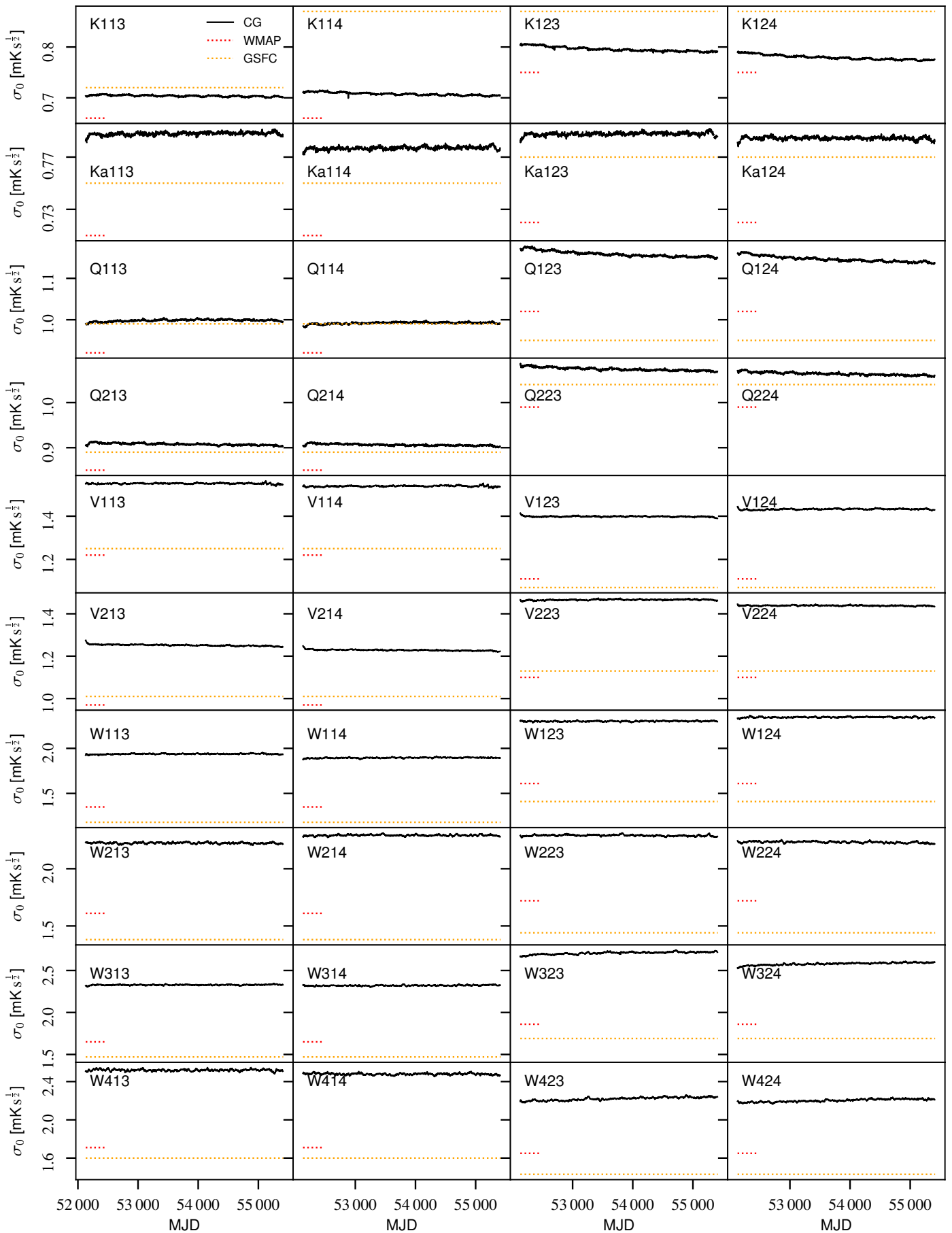


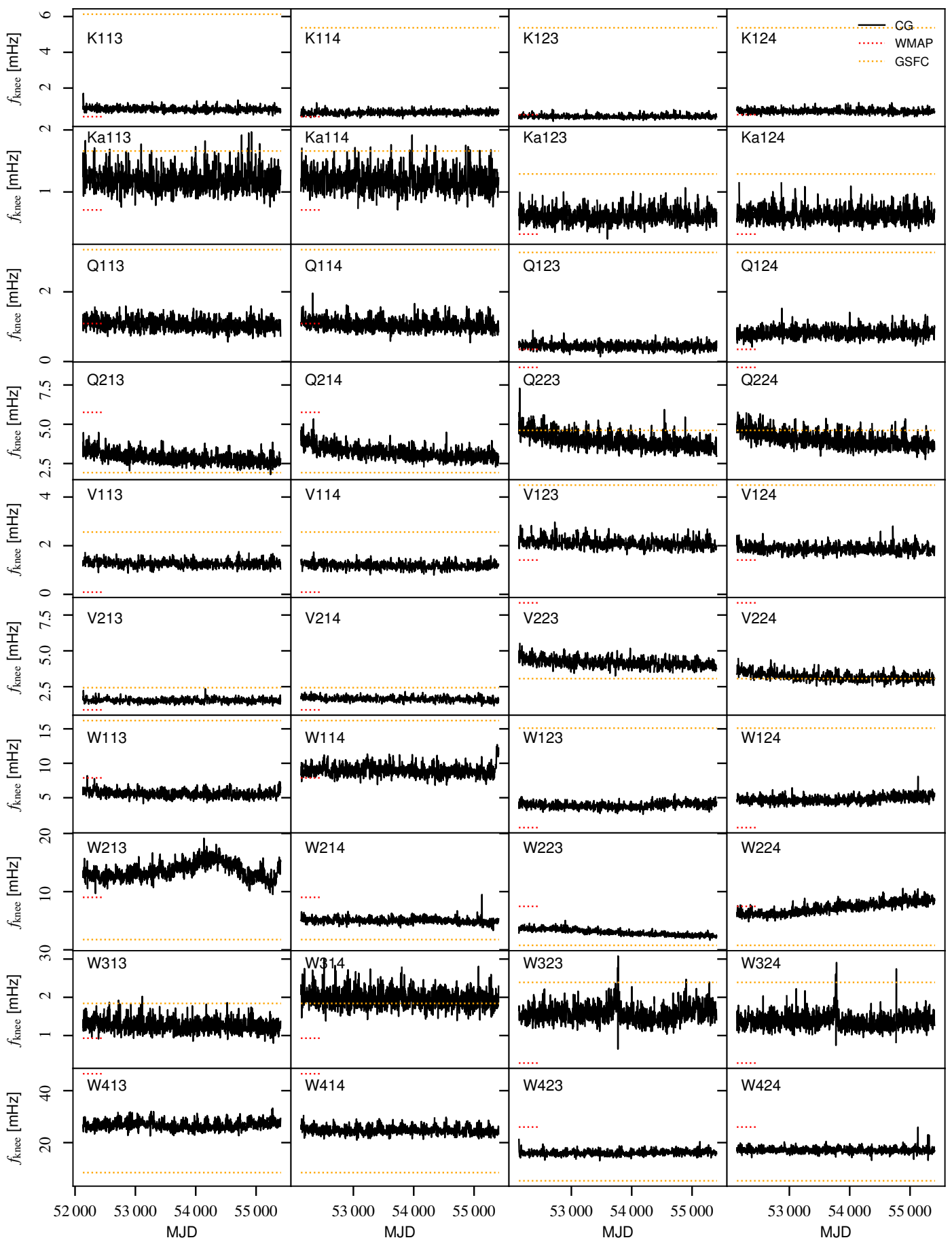
Fig. A.2. Difference in baseline solution, $b_0^{\text{CG}} - b_0^{\text{WMAP}}$.

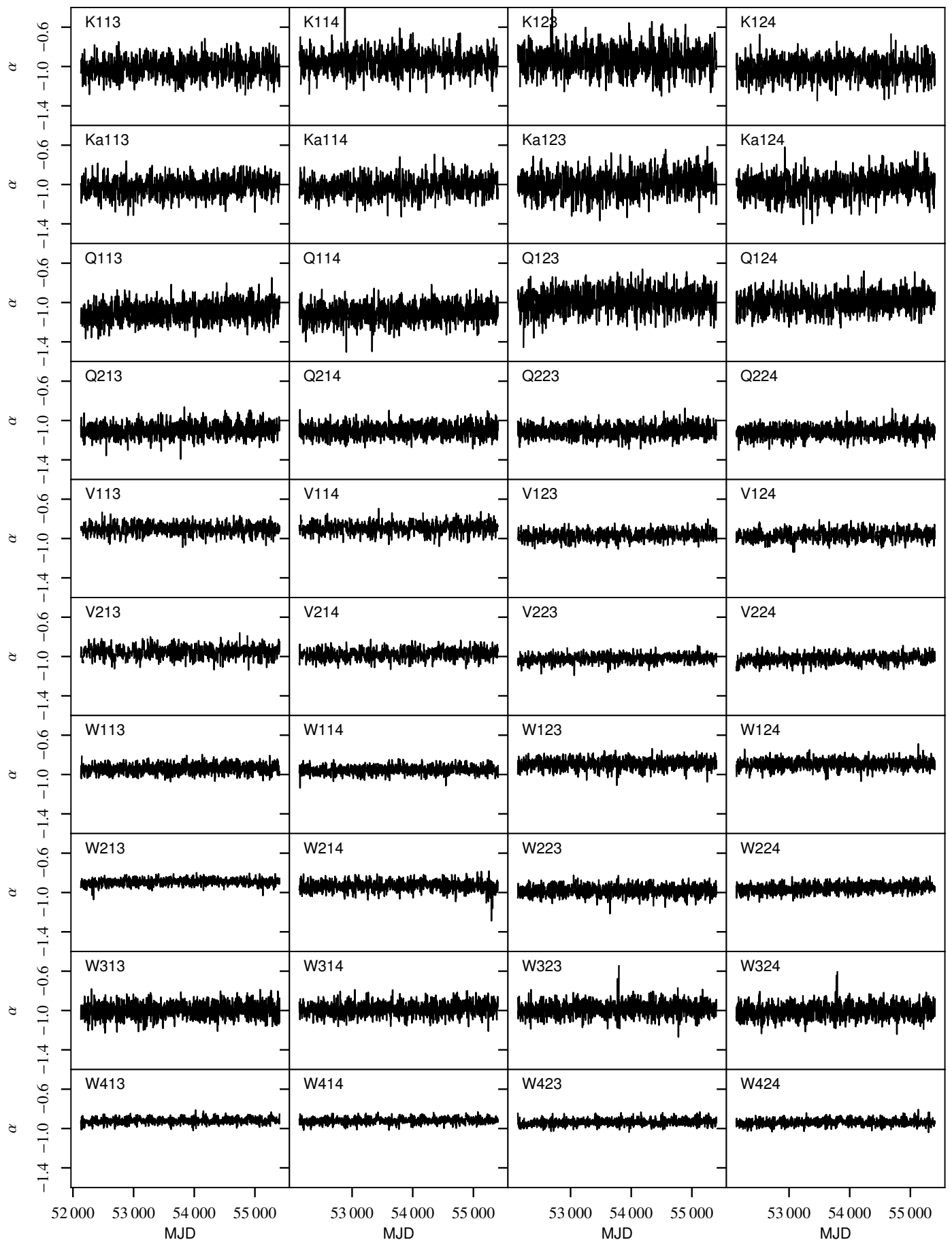
**Fig. A.3.** baseline slopes.

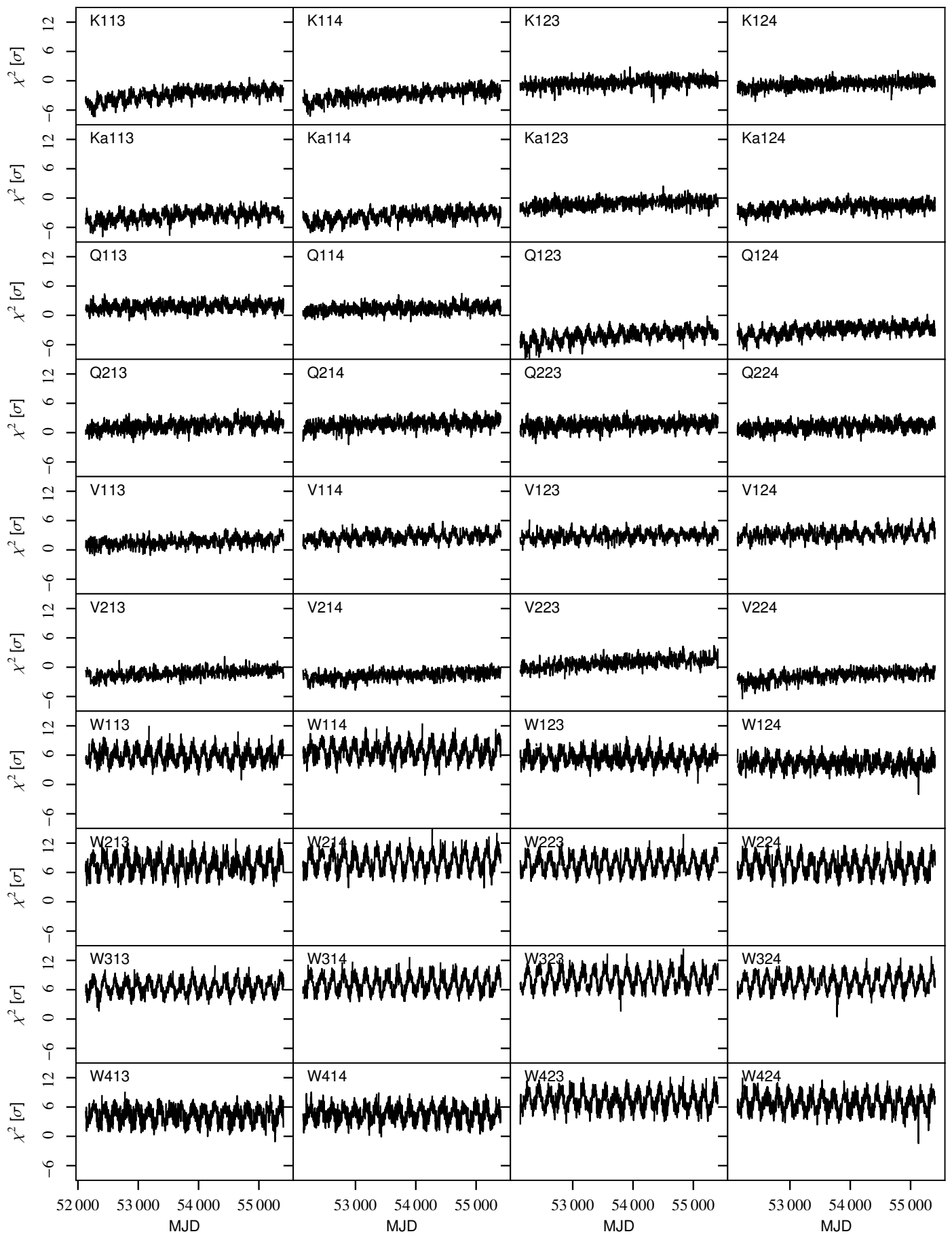
**Fig. A.4.** Gain.

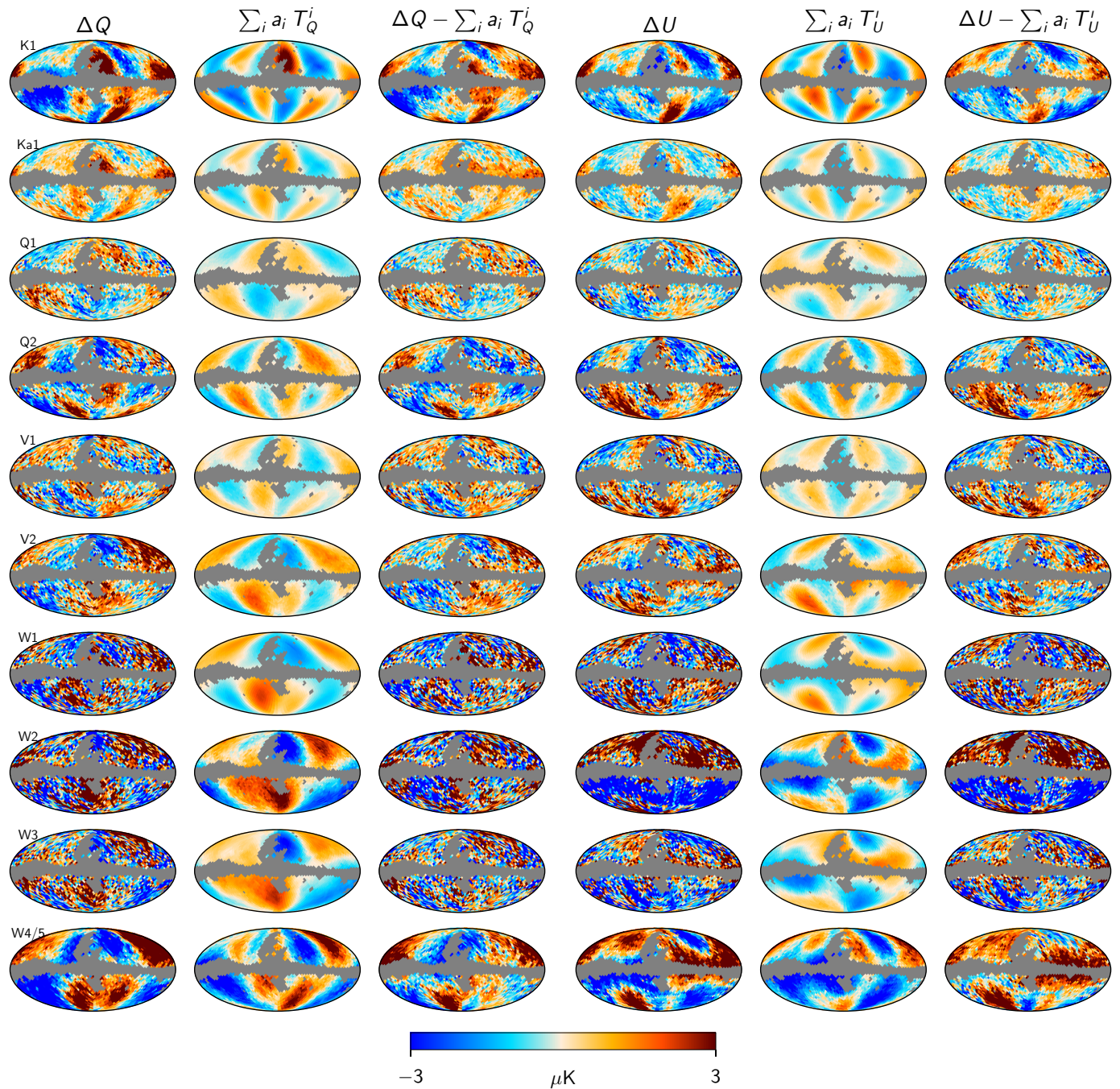
**Fig. A.5.** Relative difference in gain solutions, $(g^{\text{CG}} - g^{\text{WMAP}})/g^{\text{WMAP}}$.

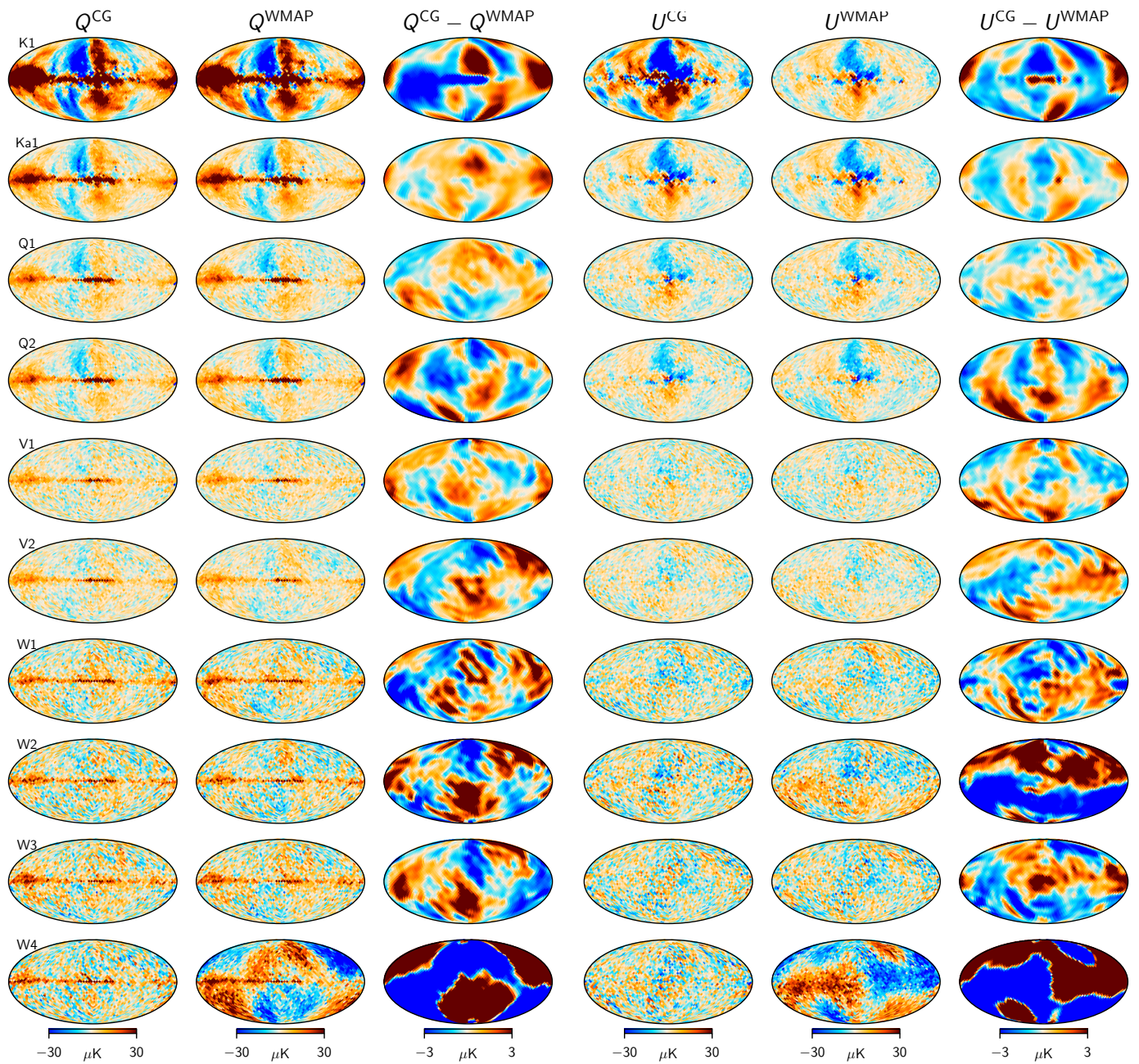
**Fig. A.6.** σ_0 .

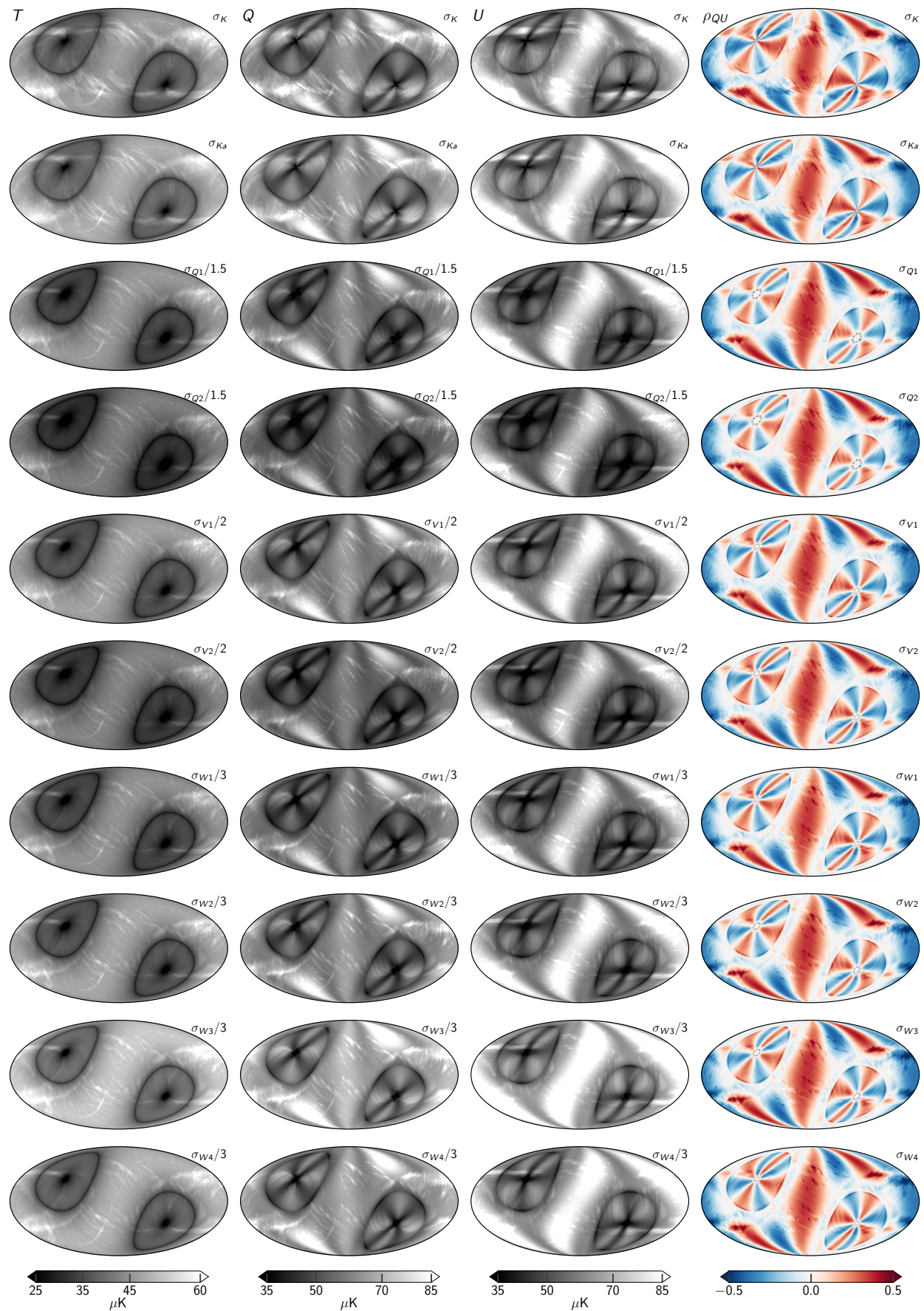
**Fig. A.7.** Fknee.

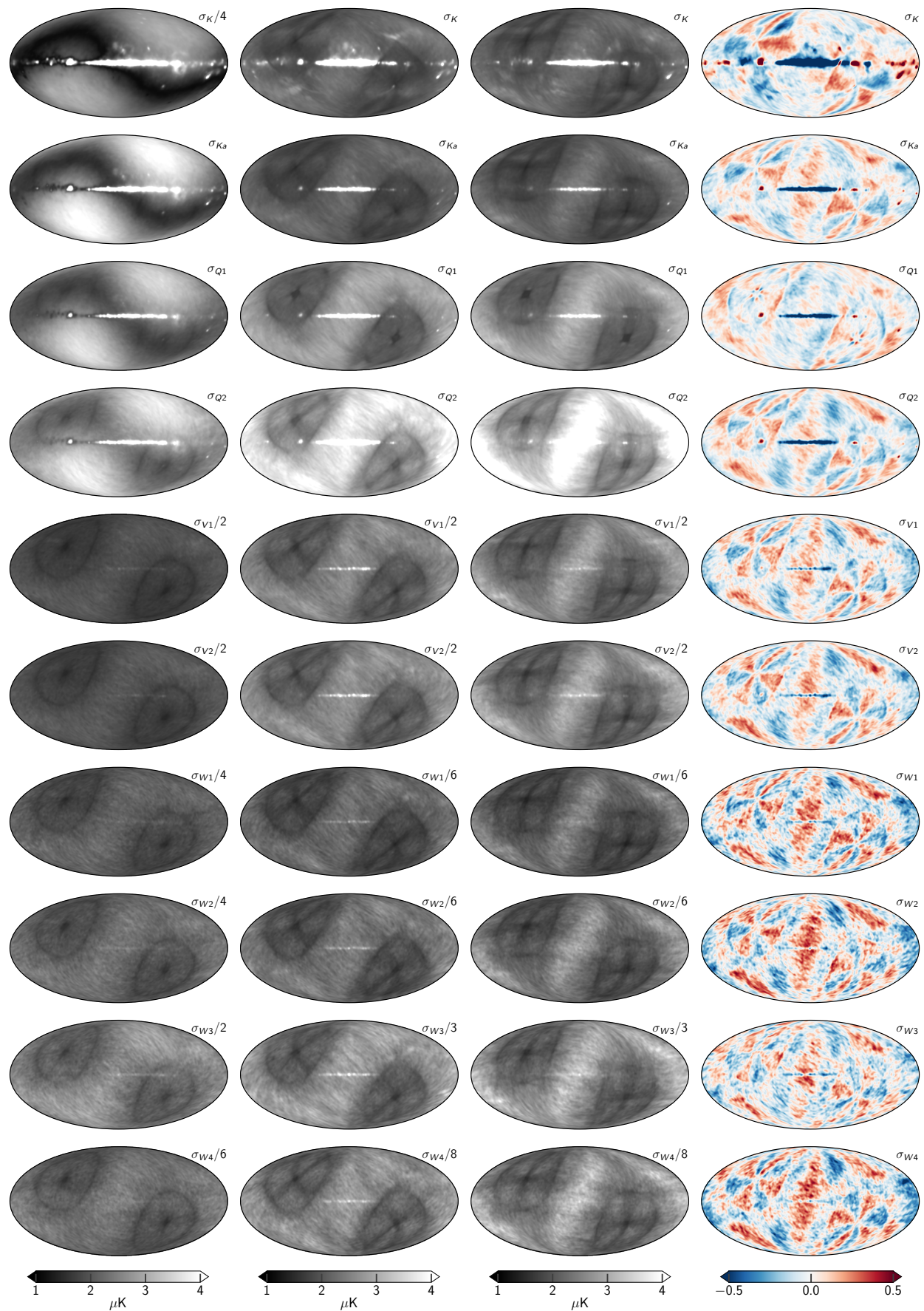
**Fig. A.8.** α .

**Fig. A.9.** chisq.

**Fig. A.10.** Transmission imbalance templates

**Fig. B.1.** Sky maps

**Fig. B.2.** RMS maps

**Fig. B.3.** STD std

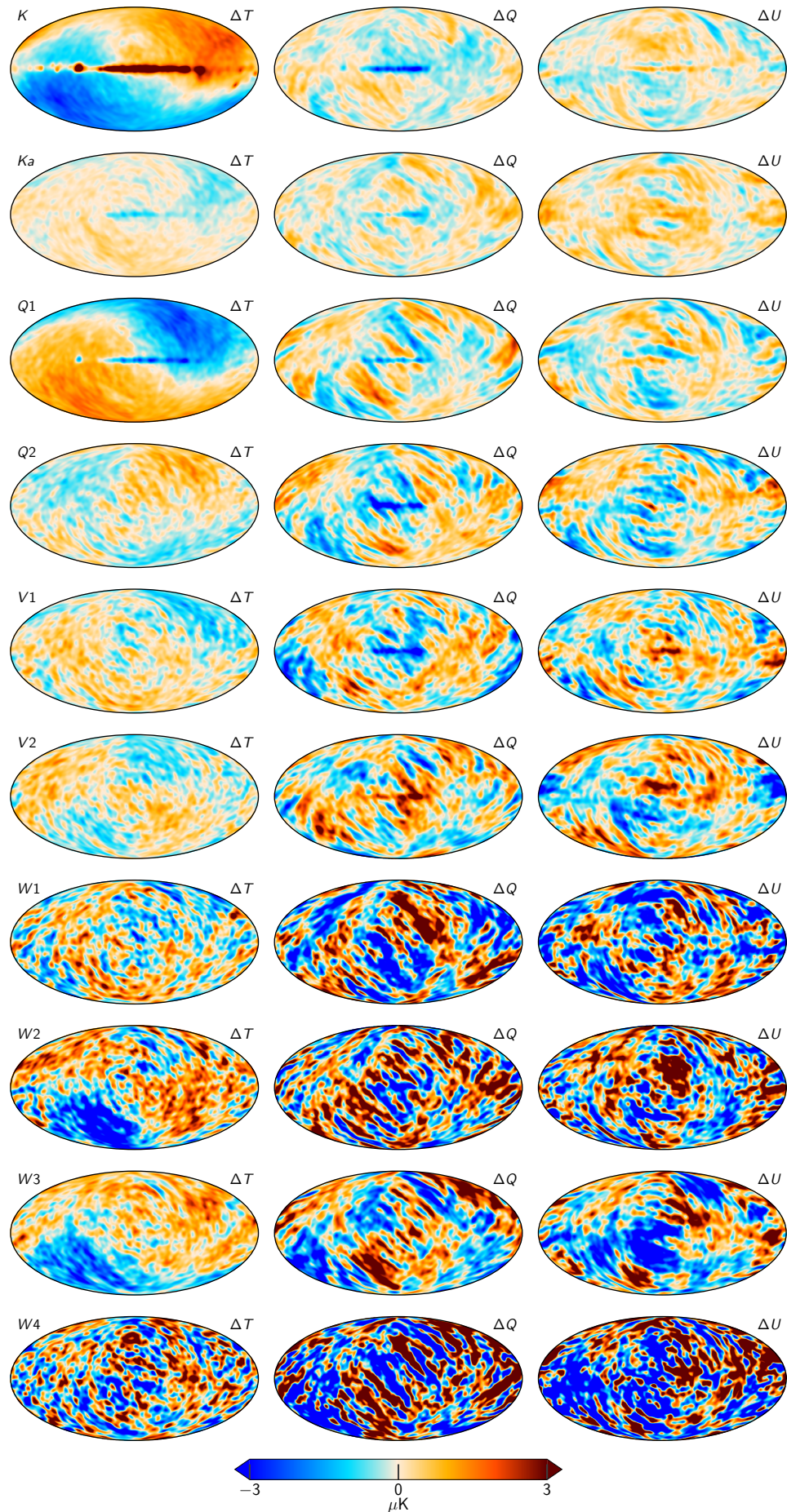
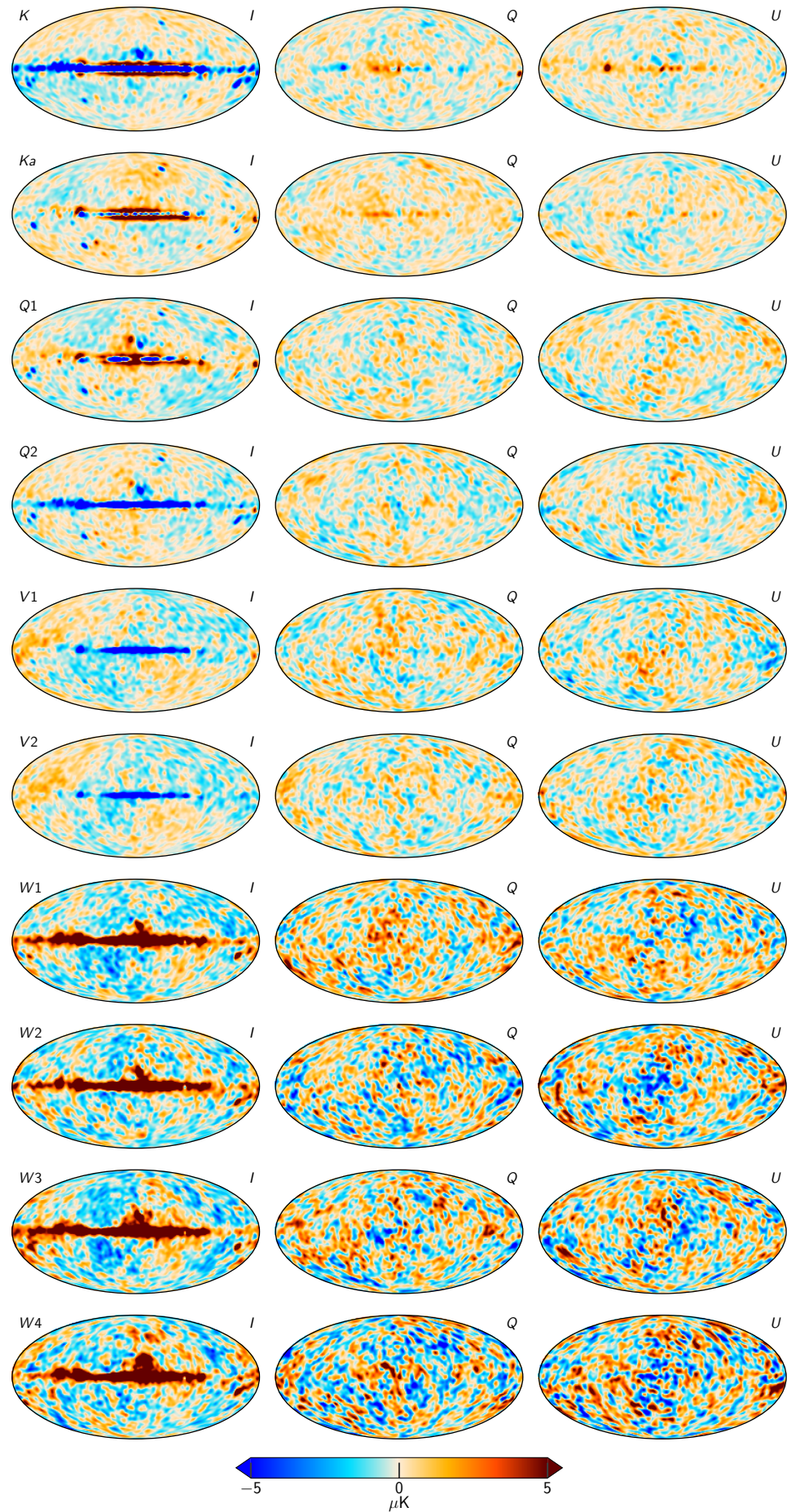


Fig. B.4. Differences between two samples
Article number, page 54 of 56

**Fig. B.5.** TOD Residuals for each of the WMAP channels, smoothed by 5° .

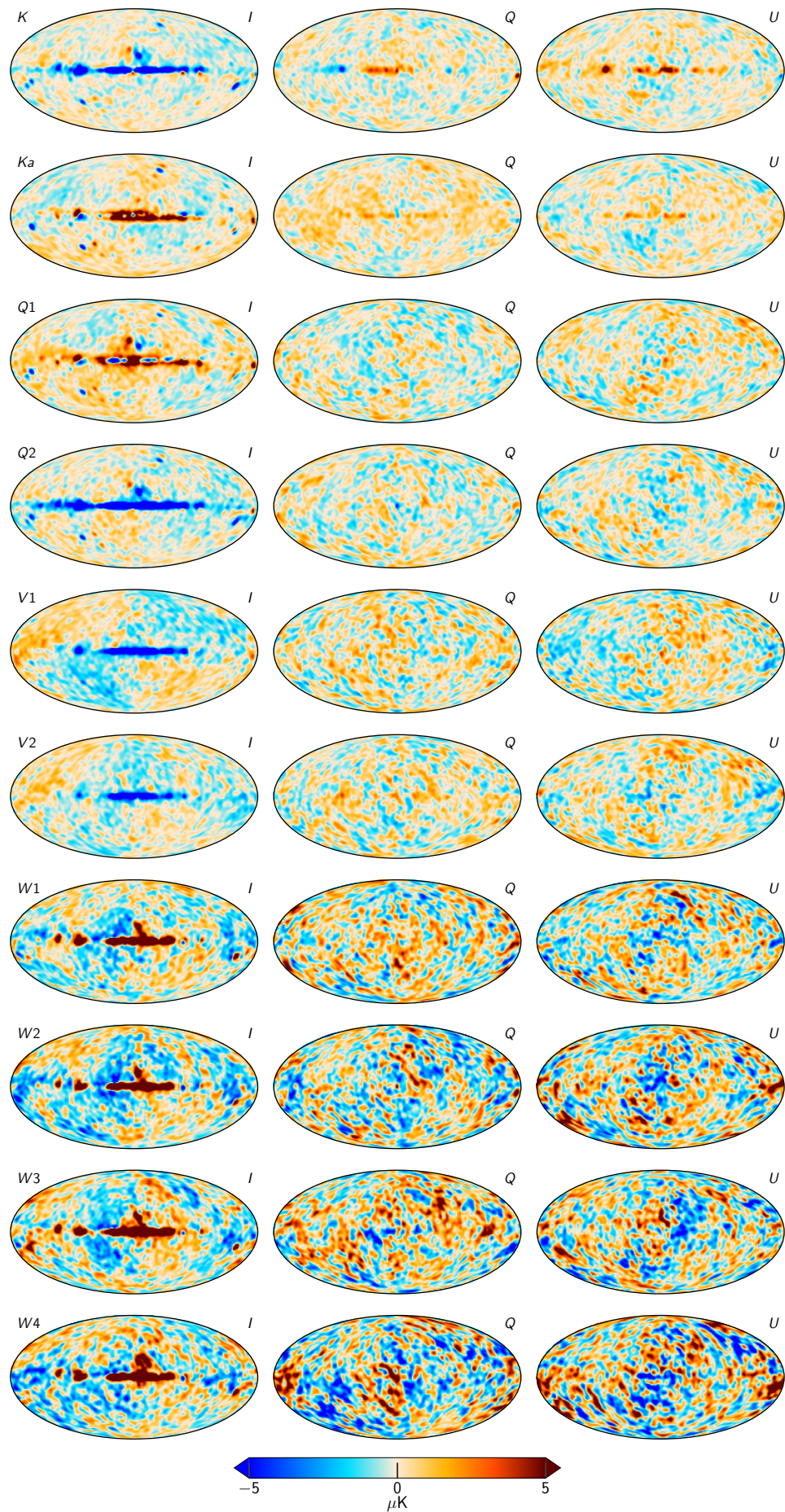


Fig. B.6. Component separation residuals for each of the WMAP channels, smoothed by 5° .
Article number, page 56 of 56